Dijet Azimuthal Decorrelations In Proton-Proton Collisions

At A Center Of Mass Energy Of 7 TeV

BY

COSMIN DRAGOIU
B.Sc., Technical University of Cluj-Napoca, 2002

THESIS

Submitted in partial fulfillment of the requirements
for the degree of Doctor of Philosophy in Physics
in the Graduate College of the
University of Illinois at Chicago, 2011

Chicago, Illinois

Defense Committee:

Nikos Varelas, Chair and Advisor
Mark Adams
David Hofman
Wai-Yee Keung
Vivian O'Dell, Fermilab

To my parents

ACKNOWLEDGMENTS

First, I would like to thank my thesis advisor Prof. Nikos Varelas for his guidance and support throughout the years. His broad experience and knowledge paved my way towards the final goal.

I am indebted to Dr. Leonard Apanasevich for his constant advise and help. I would like to thank him for all the constructive discussions we had. I would also like to express my gratitude to all members of the UIC group at CMS for their assistance.

Many thanks to the entire CMS Collaboration, especially to the hard working people from the JetMET and QCD groups. This work would not have been possible without their support.

I am grateful to Dr. Marek Zielinski for his help and advice over the years. I would also like to thank Dr. Klaus Rabbertz for providing the theory calculations used in this analysis.

On a more personal note, I would like to thank all my friends for helping me to remain sane throughout all these difficult years.

I would like to thank my parents and my sister for their support and patience while I was pursuing my studies so far away from home.

Finally, I would like to thank Ioana for her love and support. I could not have achieved all these without her.

<div style="text-align: center">

TABLE OF CONTENTS

</div>

<div style="text-align: center">

iv

</div>

LIST OF TABLES

LIST OF FIGURES

LIST OF ABBREVIATIONS

ALICE   **A** **L**arge **I**on **C**ollider **E**xperiment

APD   **A**valanche **P**hoto**D**iode

ATLAS   **A** **T**oroidal **L**HC **A**pparatu**S**

BPIX   **B**arrel **PIX**el

CERN   **C**entre **E**uropéen pour la **R**echerche **N**ucleaire

CMS   **C**ompact **M**uon **S**olenoid

CSC   **C**athode **S**trip **C**hamber

CSCTF   **C**athode **S**trip **C**hamber **T**rack **F**inder

CTEQ   The **C**oordinated **T**heoretical-**E**xperimental Project

                                  on **Q**CD

DAQ   **D**ata **A**cquisition **S**ystem

DIS   **D**eep **I**nelastic **S**cattering

DT   **D**rift **T**ube

DTTF   **D**rift **T**ube **T**rack **F**inder

EB   **E**lectromagnetic **B**arrel Calorimeter

ECAL   **E**lectromagnetic **CAL**orimeter

EE	**E**lectromagnetic **E**ndcap Calorimeter
EM	**E**lectro**M**agnetic
FPIX	**F**orward **PIX**el
FSR	**F**inal **S**tate **R**adiation
HB	**H**adronic **B**arrel Calorimeter
HCAL	**H**adronic **CAL**orimeter
HE	**H**adronic **E**ndcap Calorimeter
HF	**H**adronic **F**orward Calorimeter
HLT	**H**igh **L**evel **T**rigger
HO	**H**adronic **O**uter Calorimeter
HPD	**H**ybrid **P**hoto**D**iode
IP	**I**nteraction **P**oint
ISR	**I**nitial **S**tate **R**adiation
L1T	**L**evel-**1** **T**rigger
LEP	**L**arge **E**lectron-**P**ositron Collider
LHC	**L**arge **H**adron **C**ollider
LHCb	**L**arge **H**adron **C**ollider **b**eauty
LO	**L**eading **O**rder

MB	**M**uon **B**arrel
MC	**M**onte **C**arlo
ME	**M**uon **E**ndcap
MPF	**M**issing Transverse Energy **P**rojection **F**raction
MPI	**M**ultiple **P**arton **I**nteraction
NLO	**N**ext to **L**eading **O**rder
PDF	**P**arton **D**istribution **F**unction
PF	**P**article **F**low
pQCD	**p**erturbative **Q**uantum **C**hromo**D**ynamics
PS	**P**re**S**hower
QCD	**Q**uantum **C**hromo**D**ynamics
QED	**Q**uantum **E**lectro**D**ynamics
RECO	**RECO**nstructed
RMS	**R**oot **M**ean **S**quare
RPC	**R**esistive **P**late **C**hamber
SL	**S**uper **L**ayer
SM	**S**tandard **M**odel
TIB	**T**racker **I**nner **B**arrel

LIST OF ABBREVIATIONS (Continued)

TID   **T**racker **I**nner **D**isk

TOB   **T**racker **O**uter **B**arrel

TEC   **T**racker **E**nd**C**ap

UE   **U**nderlying **E**vent

VPT   **V**acuum **P**hoto**T**riode

ZDC   **Z**ero **D**egree **C**alorimeter

SUMMARY

Measurements of dijet azimuthal decorrelations for central rapidities in pp collisions at $\sqrt{s} = 7$ TeV using the CMS detector at the CERN LHC are presented. The analysis is based on an inclusive dijet event sample corresponding to an integrated luminosity of 2.9 pb^{-1}. The results are compared to predictions from perturbative QCD calculations and various MC event generators. The dijet azimuthal distributions are found to be sensitive to initial-state gluon radiation.

CHAPTER 1

INTRODUCTION

1.1 Standard Model

The Standard Model (SM) (1) of particle physics is a theoretical framework that describes the interactions of elementary particles with the electromagnetic, weak, and strong forces. It is a renormalizable quantum field theory (2), locally invariant under the $SU(3) \times SU(2) \times U(1)$ gauge transformations. The $SU(3)$ local symmetry is associated with the strong interaction, the $SU(2)$ with the weak interaction, and $U(1)$ with the electromagnetic interaction.

According to the SM, all known matter is made of leptons and quarks which are spin-1/2 particles. The leptons interact only through the electromagnetic and weak forces, while quarks interact through all three forces. The SM contains six leptons: the electron, electron neutrino, muon, muon neutrino, tau, and tau neutrino. They are grouped in three generations as listed in Table I. The leptons are characterized by mass, charge, electron, muon, and tau numbers. The electron and its associated neutrino have electron number one, the muon and the muon neutrino have muon number one, and the tau and its neutrino have tau number one. The charge, electron, muon, and tau numbers are conserved during all interactions. Each lepton has also an antiparticle which is identical

but with opposite quantum numbers. Only the muon, tau, and their antiparticles decay, all the other leptons are considered stable particles.

Generation	Flavor	Charge (e^-)	Mass (MeV)	Lifetime (s)
I	electron (e)	-1	0.511	∞
	e neutrino (ν_e)	0	$< 2.2 \times 10^{-6}$	∞
II	muon (μ)	-1	105.6	2.197×10^{-6}
	μ neutrino (ν_μ)	0	< 0.17	∞
III	tau (τ)	-1	1.776×10^3	2.91×10^{-13}
	τ neutrino (ν_τ)	0	< 15.5	∞

TABLE I

LEPTONS IN THE STANDARD MODEL.

Similarly, there are six quarks (Table II) which are also grouped in three generations. The lightest quarks are the up, down, and strange quarks, followed by more massive ones, the charm, bottom, and top quarks. The quarks have fractional charges and an additional quantum number called color. They can not be observed in nature as free particles, but only as part of composite objects. Fractional charges are assigned to quarks to reflect the measured charge of the composite objects. For example, the proton is made of two up quarks and one down quark. If we add the charges associated with these quarks we recover the well known charge of the proton ($(2/3 + 2/3 - 1/3)|e| = |e|$). Analogous

to leptons, each quark can have an additional flavor number which is conserved during strong and electromagnetic interactions, but not during the weak interactions. For every quark there exists also an antiquark with opposite quantum numbers.

Generation	Flavor	Charge (e$^-$)	Mass (MeV)
I	up (u)	+2/3	2.5 ± 0.8
	down (d)	-1/3	5.0 ± 0.9
II	charm (c)	+2/3	$1.27 \pm 0.09 \times 10^3$
	strange (s)	-1/3	101 ± 29
III	top (t)	+2/3	$172 \pm 2.2 \times 10^3$
	bottom (b)	-1/3	$4.19 \pm 0.18 \times 10^3$

TABLE II

QUARKS IN THE STANDARD MODEL.

Table III lists the SM interactions and their mediators. The strong interaction is mediated by eight gluons which are massless, electrically neutral, and carry both color and anti-color. The electromagnetic interaction is mediated by the photon which has zero mass and zero electric charge. The carriers of the weak interaction are the $W^{\pm}$ and Z^0 vector bosons, with $M_{W^{\pm}} \simeq 80.4$ GeV and $M_{Z^0} \simeq 91.2$ GeV. All these force carriers are spin-1 particles.

Force	Mediator	Charge (e$^-$)	Mass (MeV)	Lifetime (s)
Strong	8 gluons (g)	0	0	∞
Electromagnetic	photon (γ)	0	0	∞
Weak	$W^\pm$	± 1	$80.399 \pm 0.023 \times 10^3$	3.11×10^{-25}
	Z^0	0	$91.188 \pm 0.002 \times 10^3$	2.64×10^{-25}

TABLE III

FORCE MEDIATORS IN THE STANDARD MODEL.

The unification of the electromagnetic and the weak interactions by Glashow, Weinberg, and Salam has introduced, through spontaneous symmetry breaking, the Higgs boson (3). This is believed to be responsible for the generation of the mass of the $W^\pm$ and Z^0 vector bosons, and the mass of all elementary particles. The Higgs boson is the only particle in the SM not observed yet.

1.2 Quantum Chromodynamics

Around 1964, Gell-Man and Zweig proposed that nucleons and other strongly interacting particles are made of more basic entities, called quarks (4; 5). Around 1968, experiments at SLAC[1] on deep inelastic electron-nucleon scattering produced the first evidence that point like particles exist inside nucleons. So far, only two kinds of quark bound states are confirmed: the integral spin mesons which are considered to be quark-

---

[1]Stanford Linear Accelerator Laboratory

antiquark bound states, and the half-integral spin baryons which are considered to be bound states of three quarks.

The discovery of the Δ^{++} particle with an electric charge of +2 and spin-3/2 was interpreted as a bound state of three identical up quarks (uuu) with spin-1/2. To reconcile the quark model with the Pauli exclusion principle for fermions, an additional quantum number, the color[1], was introduced to each quark. In this model, quarks can have three distinctive colors: red, blue, and green.

The current model of the strong interactions relies on a non-Abelian gauge theory with a local $SU(3)$ color symmetry. It contains six quarks and eight gluons that represent the quanta of the $SU(3)$ gauge field. Since the gluons carry color charges, they can interact among themselves, making the Quantum Chromodynamics (QCD) a more complicated theory than Quantum Electrodynamics (QED).

---

[1]The concept of color was proposed independently in 1964 by Oscar W. Greenberg and Yoichiro Nambu

1.2.1   QCD Lagrangian

In the SM, the quark fields are described by Dirac spinors (ψ_i) with an additional degree of freedom, the color. Thus, the free Lagrangian density for a particular flavor is:

$$\mathcal{L} = i\bar{\psi}\gamma^\mu\partial_\mu\psi - m\bar{\psi}\psi \tag{1.1}$$

$$\psi \equiv \begin{pmatrix} \psi_r \\ \psi_b \\ \psi_g \end{pmatrix}, \quad \bar{\psi} \equiv \begin{pmatrix} \bar{\psi}_r & \bar{\psi}_b & \bar{\psi}_g \end{pmatrix} \tag{1.2}$$

This Lagrangian density exhibits a global symmetry under the $SU(3)$ group transformations:

$$\psi \to U\psi, \quad \bar{\psi} \to \bar{\psi}U^\dagger \tag{1.3}$$

$$U = \exp\left(-iq\mathbf{t}\cdot\boldsymbol{\phi}\right) \tag{1.4}$$

where q represents the charge of the particle involved, $\mathbf{t} = \boldsymbol{\lambda}/2$ with $\boldsymbol{\lambda}$ the Gell-Mann matrices (2), and $\boldsymbol{\phi}$ a set of eight real numbers. By promoting this global symmetry to a local $SU(3)$ symmetry with:

$$U = \exp\left(-iq\mathbf{t}\cdot\boldsymbol{\phi}(x)\right) \tag{1.5}$$

the covariant derivative needs to be replaced by:

$$\partial_\mu \to \mathcal{D}_\mu \equiv \partial_\mu + ig\mathbf{t} \cdot \mathbf{A}_\mu \tag{1.6}$$

to keep the free Lagrangian density invariant under this transformation. The $\mathbf{A}_\mu$ term represents eight gauge fields which are identified as the eight gluons of QCD and g the field strength constant. With these changes, the Lagrangian density becomes:

$$\mathcal{L} = i\bar{\psi}\gamma^\mu\partial_\mu\psi - m\bar{\psi}\psi - g\bar{\psi}\gamma^\mu\mathbf{t}\psi \cdot \mathbf{A}_\mu \tag{1.7}$$

Finally, the QCD Lagrangian density requires one more piece, the free Lagrangian density for gluons:

$$\mathcal{L}_{\text{gluon}} = -\frac{1}{4}\mathbf{F}^{\mu\nu} \cdot \mathbf{F}_{\mu\nu} \tag{1.8}$$

$$\mathbf{F}^{\mu\nu} = \partial^\mu\mathbf{A}^\nu - \partial^\nu\mathbf{A}^\mu - g\left(\mathbf{A}^\mu \times \mathbf{A}^\nu\right) \tag{1.9}$$

$$\left(\mathbf{A}^\mu \times \mathbf{A}^\nu\right)_a = \sum_{b,c} f_{abc}\mathbf{A}^\mu_b\mathbf{A}^\nu_c \tag{1.10}$$

where $\mathbf{F}^{\mu\nu}$ represents the gluon field strength tensor and f_{abc} the structure constants defined by the commutation relations of the Gell-Mann matrices:

$$[\boldsymbol{\lambda}_a, \boldsymbol{\lambda}_b] = \boldsymbol{\lambda}_a \cdot \boldsymbol{\lambda}_b - \boldsymbol{\lambda}_b \cdot \boldsymbol{\lambda}_a = if_{abc}\boldsymbol{\lambda}_c \tag{1.11}$$

The last term in the expression of $\mathbf{F}^{\mu\nu}$ is introduced by the requirement of the local $SU(3)$ symmetry. It generates the three-gluon and four-gluon self-interactions.

The complete Lagrangian density for QCD is given by:

$$\mathcal{L}_{\text{QCD}} = i\bar{\psi}\gamma^{\mu}\partial_{\mu}\psi - m\bar{\psi}\psi - \frac{1}{4}\mathbf{F}^{\mu\nu}\cdot\mathbf{F}_{\mu\nu} - g\bar{\psi}\gamma^{\mu}\mathbf{t}\psi\cdot\mathbf{A}_{\mu} \tag{1.12}$$

It describes three equal-mass Dirac fields (three colors) in interactions with eight massless vector fields (gluons). The last term in the expression describes the interaction between quarks and gluons.

1.2.2 Asymptotic Freedom and Confinement

In the case of QED, the field strength increases as the charges get closer together. This is due to the vacuum polarization which functions as a dielectric medium, partially screening the charges. The closer the two charges get, the less complete is the screening and the greater is the interaction.

An analogous effect occurs in QCD where virtual quark-antiquark pairs screen the color charge of the quarks involved. However, the additional gluon-gluon interactions generate a net opposite effect.

The running of the strong coupling constant (α_s) is given by the renormalization group equation:

$$\mu^2\frac{\partial\alpha_s}{\partial\mu^2} = \beta(\alpha_s) \tag{1.13}$$

where μ represents the cut-off scale and $\beta(\alpha_s)$ the parametrization function. If α_s is less than one, the β-function can be expended using a perturbative approach, such that:

$$\beta(\alpha_s) = -\frac{11n_c - 2n_f}{12\pi}\alpha_s^2 + \mathcal{O}(\alpha_s^3) \tag{1.14}$$

where n_c represents the number of color charges and n_f the number of quark flavors. For $n_f < 16$, the quantity $11n_c - 2n_f$ is positive, making the gluon polarization of the vacuum to dominate over the quark-antiquark contributions. Because of this, α_s decreases at short distances and quarks and gluons become asymptotically free. This makes possible the use of perturbation theory to make predictions.

The leading-log approximation of the QCD coupling constant is:

$$\alpha_s(\mu_R^2) = \frac{12\pi}{(11n_c - 2n_f)ln\frac{\mu_R^2}{\Lambda^2}} \tag{1.15}$$

where μ_R represents the renormalization scale and Λ the scale at which the theory becomes non-perturbative. In terms of the cut-off scale, Λ is defined as:

$$\Lambda^2 = \mu^2 \, exp\left[-\frac{12\pi}{(11n_c - 2n_f)\alpha_s(\mu^2)}\right] \tag{1.16}$$

marking the boundary between a world of quasi-free quarks and gluons and a world of mesons and baryons. Λ is determined experimentally and has a typical value around 250 MeV.

The variation of α_s with μ_R^2 ($\mu_R = Q$) was tested through different experiments (6) and the QCD predictions proved to be consistent with the experimental data. Figure 1 shows the measurements of α_s, for different energy scales, from Deep Inelastic Scattering (DIS), electron-positron annihilations, hadron collisions, and heavy quarkonia compared to QCD predictions.

1.3   Parton Distribution Functions

The structure of hadrons can be expressed in terms of parton distribution functions (PDFs). Each PDF represents the probability to find a parton of a given type carrying a momentum fraction x of the hadron's momentum. These functions can not be computed using perturbative Quantum Chromodynamics (pQCD) and have to be extracted from data.

Figure 2 shows the momentum densities for several partons as a function of x, at $Q^2 = 100$ GeV^2. These distributions are obtained from global fits on a large number of cross-section data points from many experiments performed by the CTEQ[1] collaboration (CTEQ6.6).

PDFs can be parametrized as a combination of polynomial functions:

$$xf(x) = p_0 x^{p_1} (1 - x)^{p_2} P(x) \tag{1.17}$$

---

[1]The Coordinated Theoretical-Experimental Project on QCD
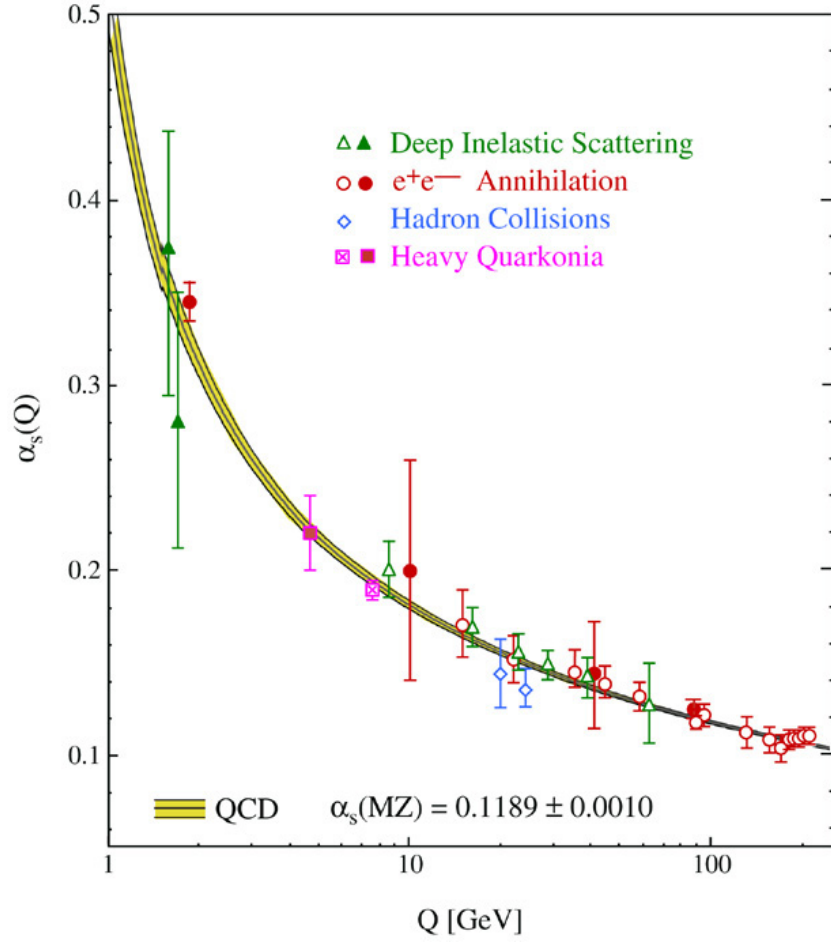
Figure 1. Measurements of α_s for different energy scales ($\mu_R = Q$), from various experiments, compared to QCD predictions.
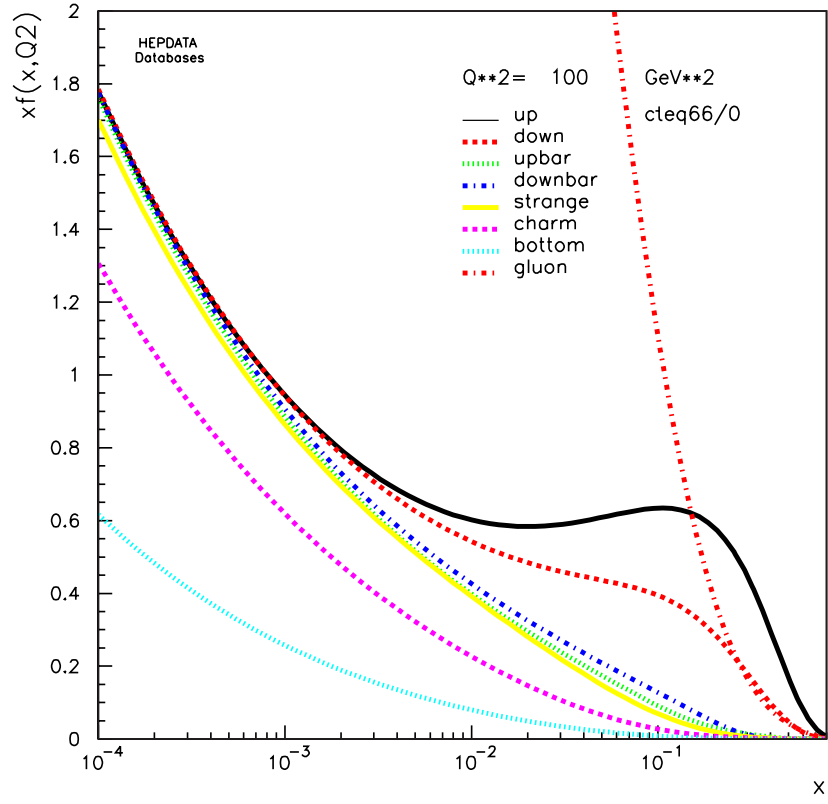
Figure 2. Momentum density functions for quarks, antiquarks, and gluons inside the proton at $Q^2 = 100$ GeV^2 as obtained by the CTEQ collaboration (CTEQ6.6).

where p_0, p_1, and p_2 represent parameters to be determined from data. The first part of the parametrization (x^{p_1}) describes the behavior of the function at small-x while $(1-x)^{p_2}$ describes the function at large-x. The behavior of $xf(x)$ in the region between these limits is described by the polynomial function $P(x)$.

Since the PDFs represent probabilities of finding various hadron constituents, they must obey certain sum rules to reflect the quantum numbers of these hadrons. For protons, for example, the PDFs must satisfy the following relations:

$$\int_0^1 [f_u(x) - f_{\bar{u}}(x)]dx = 2 \tag{1.18}$$

$$\int_0^1 [f_d(x) - f_{\bar{d}}(x)]dx = 1 \tag{1.19}$$

$$\sum_{q\in(c,s,t,b)} \int_0^1 [f_q(x) - f_{\bar{q}}(x)]dx = 0 \tag{1.20}$$

The momentum fraction carried by gluons (x_g) can be extracted from the following relation:

$$\sum_{q\in(u,d,c,s,t,b)} \int_0^1 xp[f_q(x) - f_{\bar{q}}(x)]dx = p(1 - x_g) \tag{1.21}$$

where p represents the hadron's momentum. From experimental data, around 50% of the hadron's momentum is carried by gluons.

1.3.1 PDF Evolution

The cross-section of a hard process can be expressed as a parton-parton cross-section convoluted with PDFs. The PDFs are measured at an initial μ_0^2 scale and then can be

"evolved" via pQCD to a scale μ_F. The PDF evolution is governed by the Dokshitzer-Gribov-Lipatov-Altarelli-Parisi (DGLAP) equations (2).

The evolution of the quark, antiquark, and gluon distribution functions with μ_F^2 is described by the following equations:

$$\frac{d}{d\log(\mu_F^2)}f_q(x,\mu_F^2) = \frac{\alpha_s(\mu_F^2)}{\pi}\int_x^1 \frac{dz}{z}\left[P_{q\to q}(z)f_q(\frac{x}{z},\mu_F^2) + P_{g\to q}(z)f_g(\frac{x}{z},\mu_F^2)\right] \quad (1.22)$$

$$\frac{d}{d\log(\mu_F^2)}f_{\bar{q}}(x,\mu_F^2) = \frac{\alpha_s(\mu_F^2)}{\pi}\int_x^1 \frac{dz}{z}\left[P_{q\to q}(z)f_{\bar{q}}(\frac{x}{z},\mu_F^2) + P_{g\to q}(z)f_g(\frac{x}{z},\mu_F^2)\right] \quad (1.23)$$

$$\frac{d}{d\log(\mu_F^2)}f_g(x,\mu_F^2) = \frac{\alpha_s(\mu_F^2)}{\pi}\int_x^1 \frac{dz}{z}\left[P_{q\to g}(z)\sum_{i=1}^{n_f}\left[f_{q_i}(\frac{x}{z},\mu_F^2) + f_{\bar{q}_i}(\frac{x}{z},\mu_F^2)\right]\right.$$
$$\left. +P_{g\to g}(z)f_g(\frac{x}{z},\mu_F^2)\right] \quad (1.24)$$

where $P_{q\to q}(z)$ represents the probability for a quark to emit another quark, $P_{g\to q}(z)$ the probability for a gluon to emit a quark, $P_{q\to g}(z)$ the probability of a quark to emit a gluon, and $P_{g\to g}(z)$ the probability of a gluon to emit another gluon. These splitting functions are given by:

$$P_{q\to q}(z) = \frac{4}{3}\left[\frac{1+z^2}{(1-z)_+} + \frac{3}{2}\delta(1-z)\right] \quad (1.25)$$

$$P_{g\to q}(z) = \frac{1}{2}\left[z^2 + (1-z)^2\right] \quad (1.26)$$

$$P_{q\to g}(z) = \frac{4}{3}\left[\frac{1+(1-z)^2}{z}\right] \quad (1.27)$$

$$P_{g\to g}(z) = 6\left[\frac{1-z}{z} + \frac{z}{(1-z)_+} + z(1-z) + \left(\frac{11}{12} - \frac{n_f}{18}\right)\delta(1-z)\right] \quad (1.28)$$

where:

$$\frac{1}{(1-z)_+} = \lim_{\epsilon \to 0} \left[\frac{1}{1-z}\theta(1-z-\epsilon) - \delta(1-z) \int_0^{1-\epsilon} \frac{1}{1-z'}dz' \right] \qquad (1.29)$$

1.4 Dijet Cross Section in pp Collisions

In hadron-hadron interactions, two jet events result when an incoming parton from one hadron scatters off an incoming parton from the other hadron to produce two high transverse momentum (p_T) partons, which are then observed as jets. Figure 3 illustrates how these interactions are interpreted within the parton model framework.
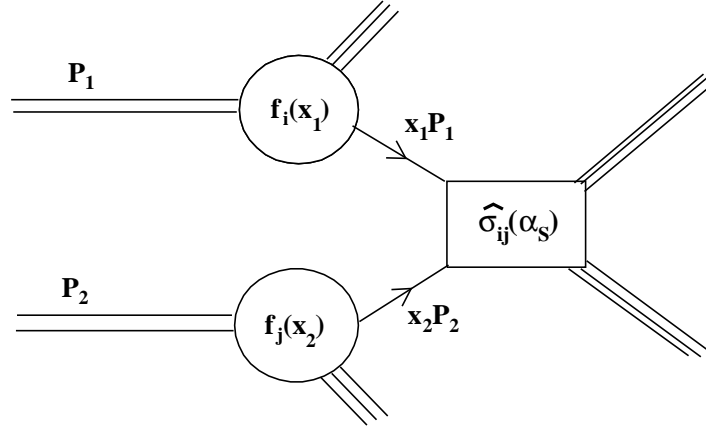
Figure 3. Parton model interpretation of a hard scattering process.

The cross-section for a hard scattering process initiated by two hadrons with momenta P_1 and P_2 is given by:

$$\sigma(P_1, P_2) = \sum_{i,j} \int dx_1 dx_2 f_i(x_1, \mu_F^2) f_j(x_2, \mu_F^2) \, \hat{\sigma}_{ij}\left(p_1, p_2, \alpha_s(\mu_R^2), \frac{Q^2}{\mu_F^2}, \frac{Q^2}{\mu_R^2}\right) \qquad (1.30)$$

where $p_1 = xP_1$ represents the momentum of parton i, $p_2 = xP_2$ the momentum of parton j, $f_i(x, \mu_F^2)$ the PDFs for parton type i, $\hat{\sigma}_{ij}$ the partonic cross-section, Q^2 the scale of the hard interaction, μ_F the factorization scale, and μ_R the renormalization scale. The most common choice of scales is: $\mu_R = \mu_F = Q$.

The partonic cross-section is obtained by summing over all possible reactions of quarks, antiquarks, and gluons. At LO ($\mathcal{O}(\alpha_s^2)$), the partonic cross-section is given by the following Feynman diagrams:
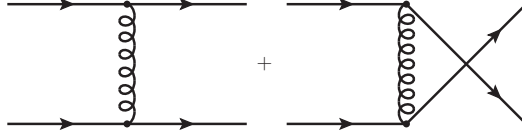
$$\frac{d}{d\hat{t}}\sigma(qq \to qq) = \frac{d}{d\hat{t}}\sigma(\bar{q}\bar{q} \to \bar{q}\bar{q}) = \frac{4\pi\alpha_s^2}{9\hat{s}^2}\left[\frac{\hat{s}^2 + \hat{u}^2}{\hat{t}^2} + \frac{\hat{s}^2 + \hat{t}^2}{\hat{u}^2} - \frac{2\hat{s}^2}{3\hat{t}\hat{u}}\right] \qquad (1.31)$$
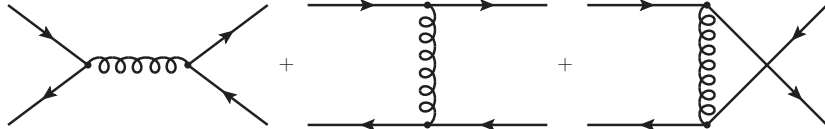
$$\frac{d}{d\hat{t}}\sigma(q\bar{q} \to q\bar{q}) = \frac{4\pi\alpha_s^2}{9\hat{s}^2}\left[\frac{\hat{s}^2 + \hat{u}^2}{\hat{t}^2} + \frac{\hat{t}^2 + \hat{u}^2}{\hat{s}^2} - \frac{2\hat{u}^2}{3\hat{s}\hat{t}}\right] \tag{1.32}$$
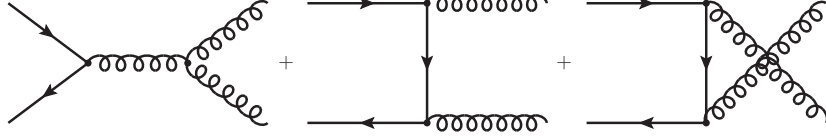
$$\frac{d}{d\hat{t}}\sigma(q\bar{q} \to gg) = \frac{32\pi\alpha_s^2}{27\hat{s}^2}\left[\frac{\hat{u}}{\hat{t}} + \frac{\hat{t}}{\hat{u}} - \frac{9(\hat{t}^2 + \hat{u}^2)}{4\hat{s}^2}\right] \tag{1.33}$$
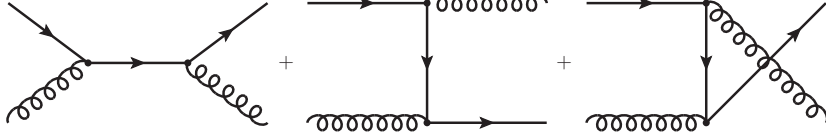
$$\frac{d}{d\hat{t}}\sigma(qg \to qg) = \frac{d}{d\hat{t}}\sigma(\bar{q}g \to \bar{q}g) = \frac{4\pi\alpha_s^2}{9\hat{s}^2}\left[-\frac{\hat{u}}{\hat{s}} - \frac{\hat{s}}{\hat{u}} + \frac{9(\hat{s}^2 + \hat{u}^2)}{4\hat{t}^2}\right] \tag{1.34}$$
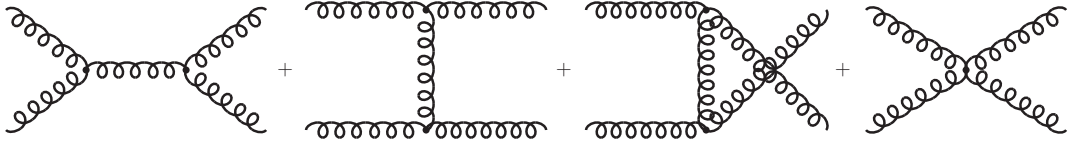
$$\frac{d}{d\hat{t}}\sigma(gg \to gg) = \frac{9\pi\alpha_s^2}{2\hat{s}^2}\left[3 - \frac{\hat{t}\hat{u}}{\hat{s}^2} - \frac{\hat{s}\hat{u}}{\hat{t}^2} - \frac{\hat{s}\hat{t}}{\hat{u}^2}\right] \tag{1.35}$$

where $\hat{s} = (p_1 + p_2)^2$, $\hat{t} = (p_1 - p_3)^2$, and $\hat{u} = (p_2 - p_3)^2$ represent the Mandelstam variables.

A more accurate description of the partonic cross-section can be obtained by including higher-order processes. Currently, next-to-leading order (NLO) predictions for $2 \rightarrow 2$ and $2 \rightarrow 3$ processes can be calculated with the NLOJET++ (7) and FastNLO (8) programs.

1.5   Dijet Azimuthal Decorrelations

At LO, dijets are produced with equal p_T with respect to the beam axis and back-to-back in the azimuthal angle.

$$p_{T,jet1} = p_{T,jet2} \tag{1.36}$$

$$\Delta\varphi_{dijet} \equiv |\varphi_{jet1} - \varphi_{jet2}| = \pi \tag{1.37}$$

Low p_T quark and gluon emissions spoil the p_T balance of the two leading jets and cause $\Delta\varphi_{dijet}$ to deviate from π. Larger deviations from π occur in the case of high-p_T multijet production. Three-jet topologies dominate the region of $2\pi/3 < \Delta\varphi_{dijet} < \pi$, whereas angles smaller than $2\pi/3$ are populated by four-jet events. Figure 4 illustrates how the parton radiation affects the $\Delta\varphi_{dijet}$ distributions.

The dijet azimuthal decorrelations can be used to study QCD radiation effects over a wide range of jet multiplicities without the need to reconstruct all the additional jets. Such studies are important because an accurate description of quark and gluon radiation is still lacking in pQCD. Experiments therefore rely on Monte Carlo (MC) event generators to take these higher-order processes into account for a wide variety of precision measurements and in searches for new physics.
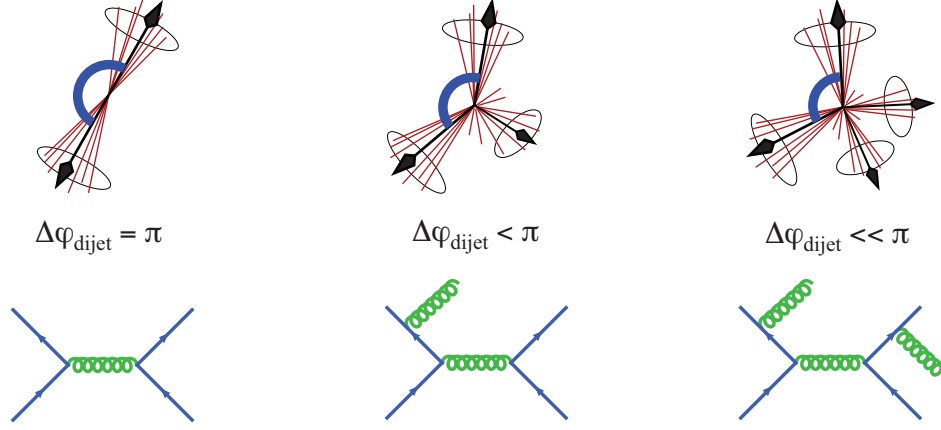
Figure 4. Examples of different levels of parton radiation and their effects on the dijet azimuthal decorrelation.

The observable chosen to study the radiation effects is the differential dijet cross section in $\Delta\varphi_{dijet}$, normalized by the dijet cross section integrated over the entire $\Delta\varphi_{dijet}$ phase space:

$$\frac{1}{\sigma_{dijet}} \cdot \frac{d\sigma_{dijet}}{d\Delta\varphi_{dijet}}. \tag{1.38}$$

By normalizing the $\Delta\varphi_{dijet}$ distributions in this manner, many experimental and theoretical uncertainties are significantly reduced.

Previous measurements of dijet azimuthal decorrelations in $p\bar{p}$ collisions at $\sqrt{s} = 1.96$ TeV have been reported by the DØ collaboration (9). These measurements were used to tune the PYTHIA MC event generator for initial state radiation. Similar measurements in pp collisions at $\sqrt{s} = 7$ TeV have also been reported by the ATLAS collab-

oration (10). In this document, the first measurements of dijet azimuthal decorrelations in pp collisions at $\sqrt{s} = 7$ TeV at the CERN LHC are presented (11).

CHAPTER 2

MONTE CARLO EVENT SIMULATION

2.1 Event Description

The purpose of a MC event generator is to simulate nature as accurately as possible. The event generation is performed in multiple steps including the hard interaction, parton showering, Underlying Event (UE), hadronization, and particle decays. To simulate the fluctuations present in real data, random number generators are used. The different methods employed to simulate specific processes and the different tuning parameters set apart one event generator from another. In this context, multiple MC event generators are often used to compare the data and to perform systematic studies.

Depending on the MC event generator, different choices are available to describe the collision of two particles. The most common interactions implemented are proton-proton, proton-antiproton, electron-positron, and electron-proton. A schematic illustration of a MC event simulation is presented in Figure 5.

A general MC event generator contains the following processes:

- **Hard Interaction**: represents the core of the event simulation. This is usually calculated at LO in pQCD. Some MC event generators can include in their matrix element calculations tree-level diagrams that correspond to higher parton multiplicities.
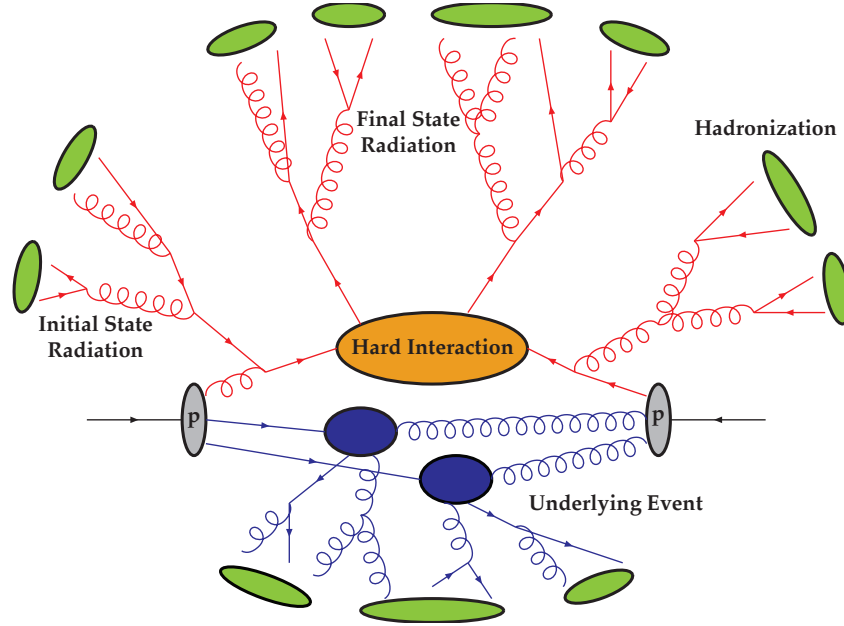
Figure 5. Schematic illustration of a MC event simulation.

- **Parton Distribution Functions**: needed for simulating proton or antiproton collisions.

- **Initial State Radiation (ISR)**: accounts for the quark and gluon radiation of the incoming partons that take part in the hard interaction. This is implemented in MC event generators as parton shower simulation. This is discussed in Section 2.2.

- **Final State Radiation (FSR)**: like the initial partons, the outgoing partons that emerge from the hard interaction can also radiate. A similar parton shower approach is used in this case (Section 2.2).

- **Color Coherence**: color coherence effects are taken into account for the initial and final state parton shower development. In PYTHIA and HERWIG++, these effects are taken into account via the angular ordering approximation.

- **Underlying Event**: represents the interactions among the remaining partons that are not involved in the hard interaction (beam remnants).

- **Multiple Parton Interaction (MPI)**: multiple interactions may also occur between more than two partons at the same time.

- **Hadronization**: describes how partons form colorless hadrons. This is usually simulated in MC event generators through the string or the cluster hadronization models (Section 2.3).

- **Particles Decay**: many particles that result during hadronization are unstable and decay further into stable particles. For a proper treatment, the decay properties of all these particles are included in MC event generators.

2.2   Parton Shower Models

2.2.1   Time-like Parton Branching

Every parton branching in the final state is of the form $a \rightarrow bc$ (i.e., $q \rightarrow qg$, $g \rightarrow q\bar{q}$, and $g \rightarrow gg$). Figure 6 shows the branching of an outgoing parton a into two partons b and c with their four-momenta satisfying $p_a^2 \gg p_b^2, p_c^2$ and $p_a^2 > 0$.

A time-like parton branching (12) is specific to final state parton showers. Within this framework, each parton is characterized by a virtuality (its four-momentum squared)
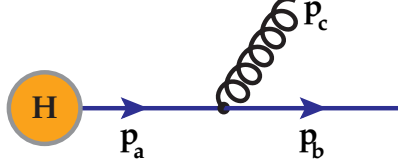
Figure 6. Branching of time-like partons specific to FSR.

which quantifies how far it is from its mass-shell. The shower initiators have the highest virtuality which is gradually decreased with each additional branching. The radiated partons can branch again depending on their virtuality. This process continues until all partons in the shower have virtualities below a cut-off value where the branching stops. For QCD showers, the usual cut-off is around 1 GeV. The ordering of the parton shower evolution can be based either on the m^2 or p_T^2 of the branching partons.

2.2.2 Space-like Parton Branching

The method used for the initial state parton shower development is similar to the one described in the previous section. However, instead of using the incoming partons as shower initiators and evolve them from a lower virtuality to a higher one, the process starts from the two partons that enter the hard interaction and evolves them backwards in time to the incoming partons. In this way the matching inefficiencies between the parton shower and the hard interaction are eliminated. This approach is called the space-like parton branching (12). Figure 7 shows the branching of an incoming parton before entering the hard interaction. The four-momenta satisfy $|p_b^2| \gg |p_a^2|, p_c^2$ with $p_b^2 < 0$.
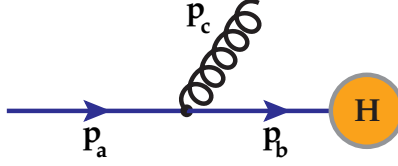
Figure 7. Branching of space-like partons specific to ISR.

Starting from the hard interaction, the virtuality of the partons decreases with each additional branching. The radiated partons (i.e., p_c) are evolved as time-like partons until they reach the cut-off virtuality. The branching process stops when the kinematics of the incoming partons are attained.

2.3   Hadronization Model

Once the parton shower has ended, the remaining partons enter a low-Q^2 regime where non-perturbative effects become important. The hadronization process simulates this regime where hadrons are produced. The most commonly used hadronization models are the string and cluster models.

2.3.1   String Hadronization Model

In a string hadronization model (12), the color flow between the partons that remain after the showering process is used to group them into string segments. Figure 8 illustrates how these string segments are constructed at the end of the parton shower. The string formation process starts from a final quark or antiquark and adds successively all color connected gluons until a final antiquark or quark is reached. At this stage a $q\bar{q}$ pair is

formed and the process starts again until all partons are grouped into $q\bar{q}$ pairs. Every time a gluon creates a $q\bar{q}$ pair during the parton shower an additional string segment is produced.
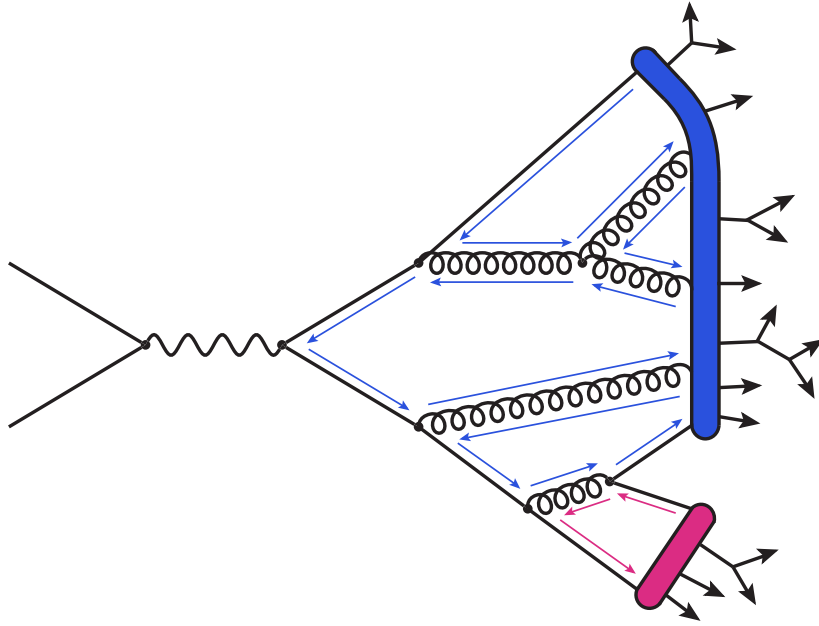
Figure 8. Example of a parton shower with string hadronization.

Once the string formation process is over, all $q\bar{q}$ pairs undergo the hadronization process. All $q\bar{q}$ pairs that have high virtualities generate further $q\bar{q}$ pairs until all formed mesons and baryons reach their mass-shell. In the string hadronization model only light

quarks can be produced. All heavy quarks (c, b, and t) can only be produced during the parton shower.

2.3.2 Cluster Hadronization Model

The cluster hadronization model (12) uses the same color flow approach to group partons together. The main difference is how the remaining gluons are treated at the end of the parton shower. Instead of keeping them as gluons, they are split into $q\bar{q}$ pairs.

Following the color flow between partons, the neighboring quarks and antiquarks are combined into separate clusters. Each cluster decays further into mesons and baryons depending on its virtuality. The usual cut-off value, around 1 GeV, generates clusters with masses as high as a few GeV. This is sufficient to produce most of the observed hadrons.

Figure 9 shows the cluster hadronization model for the same parton shower used to describe the string hadronization model.

2.4 Monte Carlo Event Generators

2.4.1 PYTHIA

One of the most widely used MC event generators in High Energy Physics is PYTHIA. It simulates high energy collisions between e^-, e^+, p, and $\bar{p}$. The hard interaction contains mostly $2 \rightarrow 2$ processes while higher multiplicities are achieved through parton showering.

Every process that contains colored objects in the initial or final state includes significant corrections from quark and gluon radiation. PYTHIA uses a space-like parton
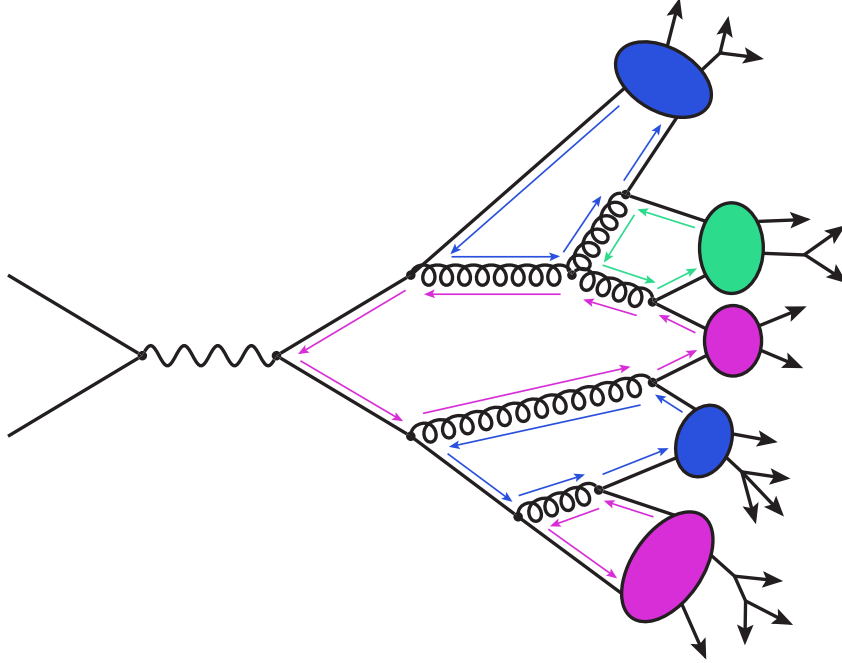
Figure 9. Example of a parton shower with cluster hadronization.

branching with backward evolution for ISR and a time-like parton branching with forward evolution for FSR. At the end of the parton showering, PYTHIA uses a string hadronization model to simulate the production of colorless hadrons.

The PYTHIA program contains many parameters that can be tuned for a better description of the data. Depending on the data used to adjust these parameters different PYTHIA tunes are available.

Currently, two versions of PYTHIA are available to simulate high energy collisions: PYTHIA6 (13) and PYTHIA8 (14). The PYTHIA6 program is written in Fortran 77 while PYTHIA8 is written in C++ and represents the successor of PYTHIA6.

In the new version, several improvements in the simulation of high energy collisions are implemented. The most notable are: the possibility to use one PDF set for the hard interaction and another set for parton showering and MPI, p_T-ordered ISR and FSR evolution, and a richer mix of UE processes.

2.4.2 HERWIG++

Another widely used MC event generator program is HERWIG++ (15). It can simulate collisions between e^-, e^+, p, and $\bar{p}$. The hard interaction processes are calculated as $2 \rightarrow 2$ at LO in perturbation theory.

The virtuality of the hard interaction and the color flow between partons set the starting conditions for the development of the initial and the final state parton showers. HERWIG++ uses a modified parton showering (16) that takes into account angular ordering effects for both ISR and FSR. Massive fundamental particles can also initiate parton showers both before and after their decay.

The UE in HERWIG++ is modeled as MPIs where one of them represents the hard interaction while the others are treated as soft scatterings. The combination of partons into colorless hadrons or hadron resonances is done using a cluster hadronization model.

2.4.3   MADGRAPH

Most of the current MC event generators compute the matrix elements for the hard interaction only at $2 \rightarrow 2$ LO in perturbation theory. A better description of the real processes in high energy collisions can be achieved by including higher order diagrams in the matrix element calculations. MADGRAPH (17) is an event generator that simulates up to seven particles at LO in the final state.

The current version of MADGRAPH implements both SM and Beyond Standard Model processes. It has the capability to run user defined models through the use of simple text files called run cards. The program can be run either locally or through a web interface making it user friendly. The code that calculates the Feynman diagram amplitudes is generated "on the fly" depending on the user's request.

The parton level MADGRAPH events do not include showering and hadronization effects. For a complete simulation, the events are passed through an additional MC event generator. The most common choice is PYTHIA. To facilitate this combination, the MADGRAPH events are stored in the common "Les Houches" event format (18). To avoid the double counting of parton emissions in the overlapping phase space regions, a matching algorithm is used to combine MADGRAPH partons with the ones from PYTHIA.

2.5 <u>Detector Simulation</u>

The simulation of particle detectors in high energy experiments is done within the GEANT 4 framework (19). The software provides a diverse set of tools that can be used from simple to full scale detector simulations. Information like the geometry of the detector, materials involved, the underlaying physics of particle interactions, and the response of the detector components are needed for a realistic simulation.

The GEANT 4 toolkit offers the possibility to create very complex models with a large number of components and materials, and to define active elements that record the information needed to simulate the detector response.

The software contains a set of physics models that handle the interactions of particles with matter for a wide energy range. The particles are characterized mainly by their mass, charge, and a list of processes to which they are sensitive. To simulate realistic electromagnetic (EM) and hadronic showers, material characteristics like the radiation and the interaction length are computed from the element makeup, and if necessary, from the isotope composition. The mean lifetime and branching ratios of all unstable particles are included in order to simulate their decay.

The GEANT 4 event contains information about the initial vertices and particles, the simulated hits and digitizations generated by the simulation, and information about the trajectories of the simulated particles.

CHAPTER 3

LHC AND THE CMS DETECTOR

3.1   Large Hadron Collider

3.1.1   General Description

The LHC (20) located at "Le Centre Européen pour la Recherche Nucleaire" (CERN), Geneva, on the border between Switzerland and France, is a powerful proton-proton accelerator designed to reach a center-of-mass energy of 14 TeV. The construction of the accelerator was approved by the CERN Council in 1996 and in September 2008 the first beams were circulated. The physics program at half of the nominal energy (7 TeV) started in 2010 and is expected to continue until the end of 2012 when a long upgrade period is scheduled to prepare the accelerator to run at the nominal energy of 14 TeV. In addition to the proton-proton physics program, heavy ion collisions between fully ionized lead atoms (Pb_{208}^{+82}) are also scheduled after periods of proton physics. The LHC collided heavy ions for the first time in November 2010.

The LHC machine (Figure 10) is situated in the old Large Electron-Positron Collider (LEP) tunnel, and lies beneath the surface at a depth that varies between 45 m and 170 m. The tunnel has a circumference of 26.7 km. The machine contains eight arcs and eight straight sections (Figure 11). Each straight section can accommodate a beam insertion point and an experiment.
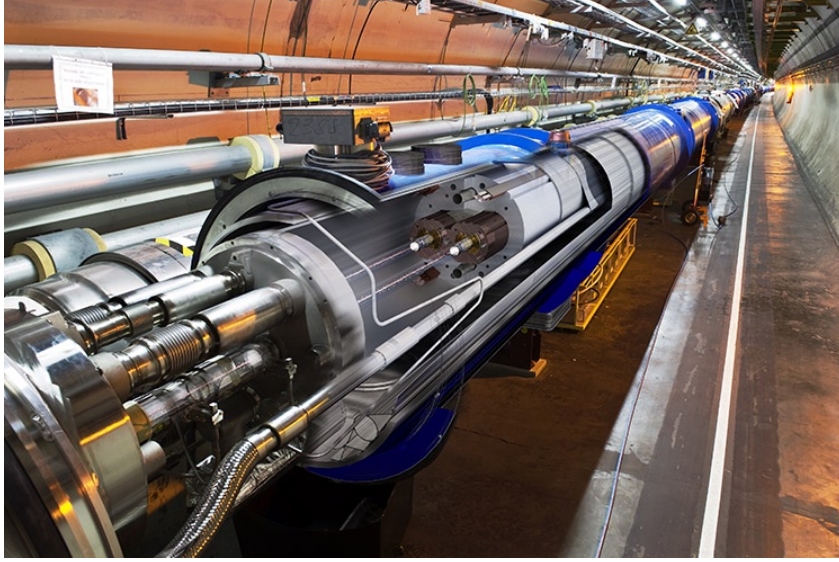
Figure 10. The LHC assembled in the LEP tunnel.

The Toroidal LHC Apparatus (ATLAS) experiment (21), located at P1, and the Compact Muon Solenoid (CMS) experiment (22), located diametrically opposite at P5, consist of general purpose detectors designed for proton-proton collisions. P2 hosts the injection system for Beam 1 and the Large Ion Collider Experiment (ALICE) (23), which is designed to study high energy nucleus-nucleus collisions. The Large Hadron Collider beauty (LHCb) experiment (24), which is optimized to study the physics of b-quarks, and the injection system for Beam 2, are located at P8. The straight sections located at P3 and P7 are equipped with collimation systems while P4 holds two radio frequency systems needed to capture, accelerate and store the two beams. The remaining straight section at P6 contains the beam dumping system.
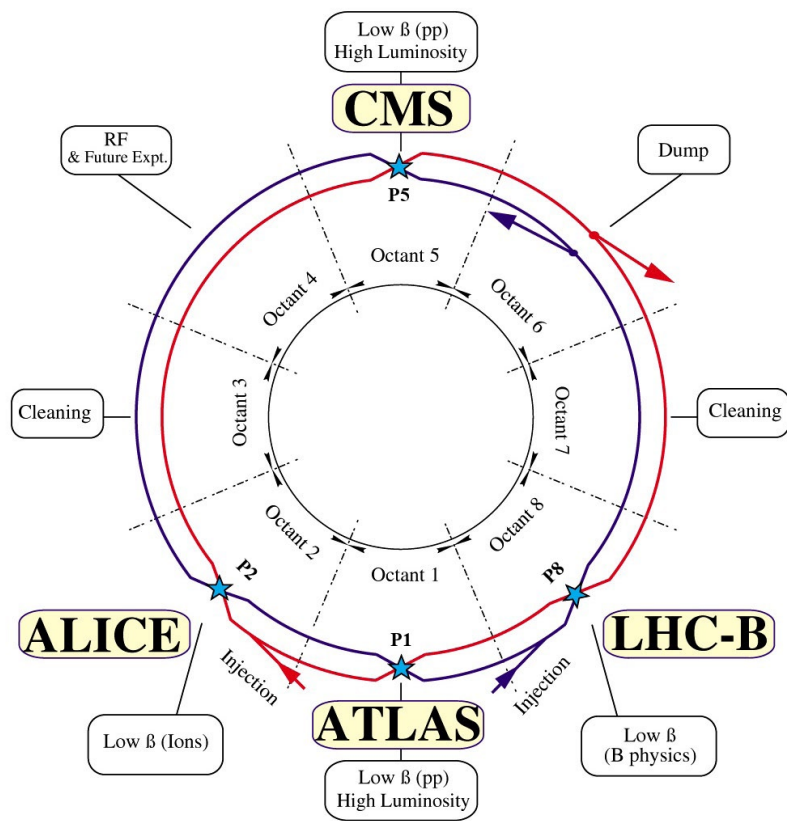
Figure 11. The LHC layout with Beam 1 clockwise and Beam 2 counterclockwise.

The protons enter the linac accelerator at 750 keV and get accelerated to 50 MeV. The next stage of the accelerator chain, the proton synchrotron booster, increases the energy of protons to 1.4 GeV. The proton synchrotron and the super proton synchrotron increase the energy of protons first to 25 GeV and then to 450 GeV. At this energy, the protons enter the main LHC ring where they can get accelerated to energies up to 7 TeV.

To achieve such beam energies, the LHC magnets are cooled below 2 K in order to operate at fields above 8 T. The insulation vacuum for cryo-magnets and helium distribution is around 10^{-6} mbar while for the beam pipes the equivalent hydrogen density has to be below 10^{-15} H_2 m^{-3} to ensure a nominal beam lifetime of 100 hours. To reduce the beam-gas interactions, the interaction point (IP) density has to be less than 10^{-13} H_2 m^{-3} (20).

3.1.2 Luminosity Calculation

The luminosity quantifies the number of particles that cross a given area in a given time interval. It is a crucial parameter needed in the commissioning process and to perform precise physics measurements. For a gaussian beam distribution, the instantaneous luminosity is given by:

$$\mathcal{L} = \frac{N_p^2 N_b f \gamma F}{4\pi \varepsilon_T \beta} \tag{3.1}$$

where N_p represents the number of particles per bunch, N_b the number of bunches per beam, f the revolution frequency, γ the relativistic gamma factor, F the geometric

luminosity reduction factor, ε_T the normalized transverse beam emittance, and β the betatron function at the collision point.

The profile of the beam in the transverse plane can be described by an ellipse of constant area ($\pi\varepsilon_T$) and variable shape. The two semi-axes change accordingly to β as $\sqrt{\varepsilon_T/\beta}$ and $\sqrt{\varepsilon_T\beta}$. The geometric luminosity reduction factor F in the case of a circular beam is calculated as:

$$F = \left(1 + \left(\frac{\theta\sigma_z}{2\sigma_T}\right)^2\right)^{-1/2} \tag{3.2}$$

where θ is the crossing angle at IP, σ_z the root-mean-square (RMS) bunch length, and σ_T the transverse RMS beam size at IP.

The instantaneous luminosity during a physics run decays over time because of the degradation of the beam emittance and intensity. The integrated luminosity over the run is given by:

$$L = \mathcal{L}_0\tau\left[1 - exp\left(-T/\tau\right)\right] \tag{3.3}$$

where $\mathcal{L}_0$ is the initial instantaneous luminosity, τ the luminosity lifetime, and T the duration of the run.

The nominal beam parameters for proton-proton and lead-lead collisions are listed in Table IV.

Beam Parameters	Protons	Lead Ions
Injection energy per nucleon [GeV]	450	177.4
Collision energy per nucleon [TeV]	7	2.76
Number of particles per bunch	1.1×10^{11}	7.0×10^{7}
Number of bunches	2808	592
Bunch separation [ns]	25	100
Betatron function at IP (β) [μm]	0.55	0.5
Transverse normalized emittance at IP (ε_T) [μm]	3.75	1.5
Instantaneous luminosity [cm^{-2}s^{-1}]	10^{34}	10^{27}

TABLE IV

LHC NOMINAL PARAMETERS FOR PROTON AND LEAD-ION COLLISIONS.

3.2   Compact Muon Solenoid Detector

3.2.1   General Description

The CMS is a general purpose detector, located in the LHC tunnel at P5, 100 m underground, close to the village of Cessy, France. Figure 12 shows the layout of the CMS detector. It is 21.6 m long with a diameter of 14.6 m and a total weight of 12500 tonnes. The CMS coordinate system has the x-axis pointing inwards towards the center of LHC, the y-axis in the vertical plane pointing upwards and the z-axis following the Beam 2 counterclockwise direction. The origin is located at the nominal collision point at the center of the detector.
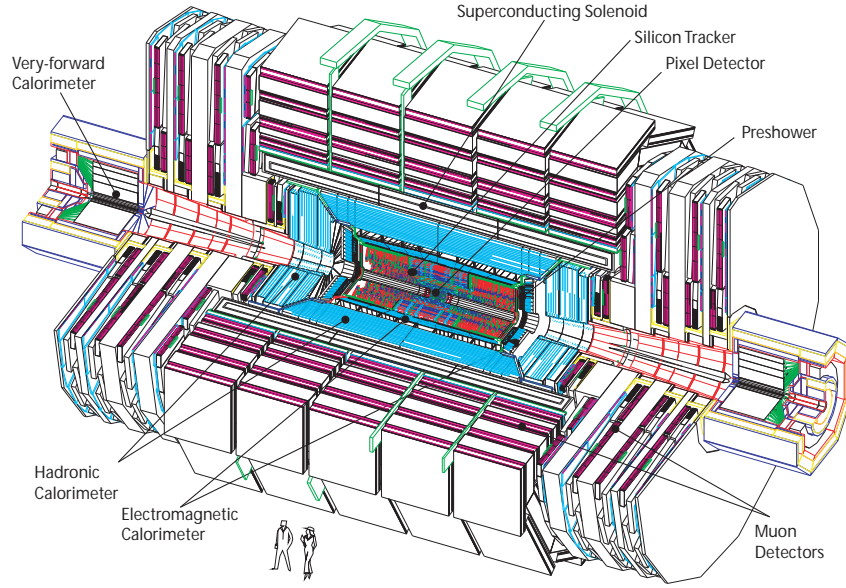
Figure 12. A 3D modeling of the CMS detector.

The pixel detector and the silicon tracker are the detectors closest to the beam pipe, and are used to determine the trajectories of charged particles. The coverage in pseudo-rapidity of the tracking detector is $|\eta| < 2.5$. The pseudo-rapidity is defined as:

$$\eta = -ln \left[tan \left(\frac{\theta}{2} \right) \right] \tag{3.4}$$

where θ represents the polar angle relative to the counterclockwise proton beam direction with respect to the center of the detector.

The tracking system is surrounded by the calorimeter system with the electromagnetic calorimeter (ECAL) located inside the hadronic calorimeter (HCAL). The ECAL system

uses lead tungstate ($PbWO_4$) crystals to measure the energy deposited by electrons and photons. It provides a coverage of $|\eta| < 3.0$. The HCAL system uses brass or steel absorber plates and plastic scintillators to measure the energy deposited by neutral and charged hadrons, with a coverage of $|\eta| < 5.2$. Both tracker and calorimeter systems are immersed in a uniform 3.8 T field generated by a superconductive solenoid. Outside the magnet is located the muon system which provides a coverage of $|\eta| < 2.4$. A side view of the CMS detector with the endcap removed is shown in Figure 13, and a detailed visualization of the CMS detector segmentation in η in Figure 14.

Figure 13. A side view of the central part of the CMS detector.
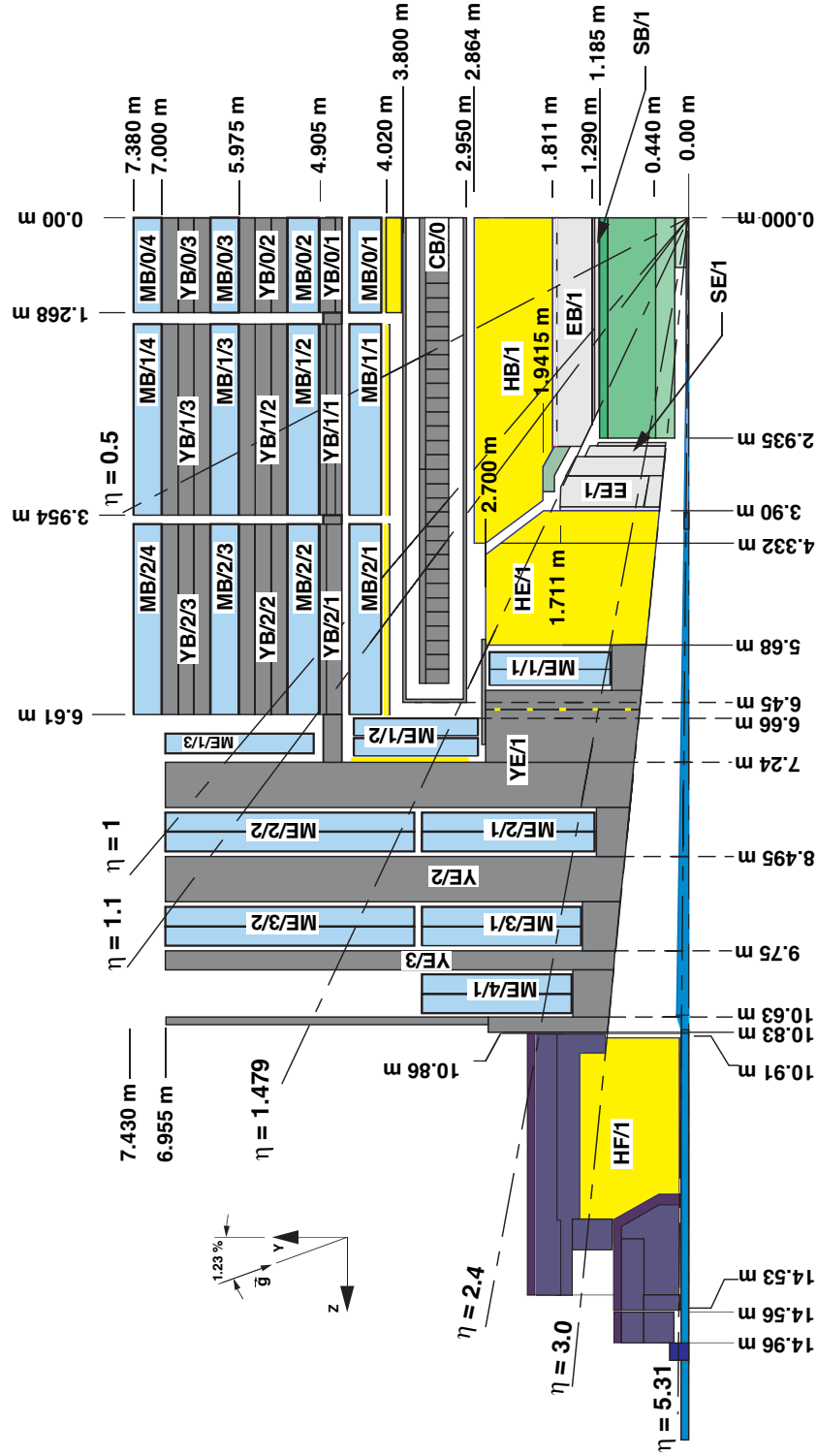
Figure 14. A cross-section view of the CMS detector along the z-axis.

3.2.2   Tracking System

The CMS tracker (25) consists of two major components: the pixel detector and the silicon strip tracker. It is made of 65 million semiconductor devices and can measure trajectories of charged particles. These semiconductor devices are basically ionization detectors that measure the energy deposited by charged particles when crossing their depleted area. The operating temperature of the tracker is around -10 °C.

The pixel detector (Figure 15) is the detector closest to the beam pipe. Its role is to provide a precise measurement on all three axes for the position of charged particles that traverse the detector. The excellent spatial resolution (15–20 μm) of the pixel detector allows the reconstruction of the primary collision vertex as well as any secondary vertices that result from the decays of b-quarks and other long lived particles.

The barrel pixel (BPIX) contains three layers of silicon sensors at radii of 4.4, 7.3, and 10.2 cm with a length of 53 cm and a coverage of $|\eta| < 2.5$. It contains approximately 48 million pixels of 100×150 μm^2 in size.

The forward pixel (FPIX) is made of four disks that extend from 6 to 15 cm in radius with a coverage from $1.5 < |\eta| < 2.5$. The FPIX disks are placed on both sides of the IP at distances of 34.5 and 46.5 cm. The forward pixels are tilted 20° out of the disk plane in order to have the signal in multiple pixels. The detector contains around 12 million pixels. Taken together, the BPIX and FPIX detectors provide minimum three hits per track in almost every η range.
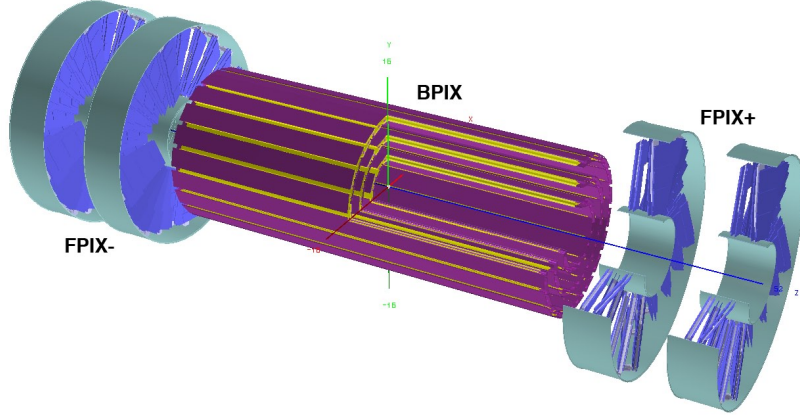
Figure 15. A perspective view of the CMS pixel detector.

The silicon strip tracker (Figure 16) is divided into four subsystems: the tracker inner barrel (TIB), the tracker inner disk (TID), the tracker outer barrel (TOB), and the tracker endcap (TEC). The TIB contains four cylindrical layers of silicon sensors at radii of 25.5, 33.9, 41.8 and 49.8 cm with a length of 1.4 m. The two innermost layers have double-sided modules while the remaining ones are single-sided only. Mounting two silicon strip modules back-to-back with an angle of 100 mrad between them provides additional spatial information to fully reconstruct the position of the tracks in all three coordinates.

The TID subsystem comprises three disks, each with an inner radius of 20 cm and an outer radius of 50 cm. Two TIDs span a distance along the beam axis between 0.8 and 0.9 m on both sides of the IP. Each disk is further divided in three concentric rings

with the two innermost rings having double-sided modules and the outermost ring with single-sided modules only. Together the TIB and TID provide a coverage of $|\eta| < 2.5$.

The TOB subsystem is split into six cylindrical layers of silicon sensors. The two innermost layers contain double sided modules while the rest are only single sided. The total length of the TOB detector is about 2.4 m with a radial span between 55.5 and 116 cm.

The last components of the tracking system are the two endcap detectors. They span a radial distance between 22 and 113.5 cm and a longitudinal coverage between 1.2 to 2.8 m on both sides of the IP. Each TEC contains nine disks on which the sensor modules are mounted. Disks one, two, and three consist of seven rings of modules. Disks four, five, and six have the innermost ring (ring one) removed in order to accommodate the installation of the pixel detector. For the same reason, disks seven and eight have rings one and two removed, while the outer disk has only four rings (four to seven). From the seven rings, only ring one, two and five have double-sided modules.

3.2.3 Electromagnetic Calorimeter

A reliable calorimetric measurement assumes a complete absorption of the energy of particles in a specific bulk of material. The main interaction of high energy electrons and positrons with matter is through bremsstrahlung while energetic photons produce $e^- e^+$ pairs (26).
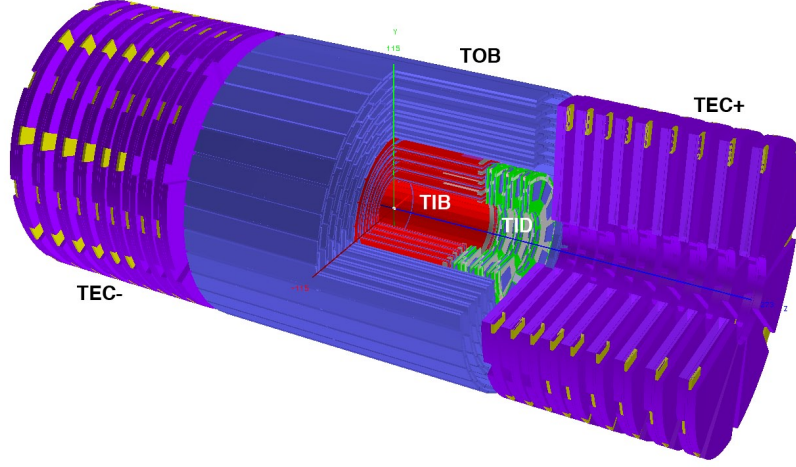
Figure 16. A perspective view of the CMS silicon strip tracker.

The radiation loss of a charged particle with energy E traveling through matter can be described by:

$$-\left(\frac{dE}{dx}\right) = \frac{E}{X_0} \qquad (3.5)$$

where X_0 is the radiation length of the material. For photons, the mean free path for pair production is $9 \cdot X_0/7$. After one radiation length the photon produces on average an $e^- e^+$ pair. The new particles emit after another X_0 one bremsstrahlung photon each, which again produces an $e^- e^+$ pair. This multiplicative process, called an EM shower, continues until the energy of all particles falls below a critical value E_c. After this point, the dominant interaction with the matter for electrons and positrons is through ionization and excitations while for photons is through Compton and photoelectric effects. The EM shower usually stops after another X_0.

The longitudinal development of an EM shower is thus characterized by X_0. After n multiplication steps, the EM shower contains 2^n particles with energy $E_0/2^n$. The average angular deflection per radiation length of the EM shower is quantified by a Molière radius:

$$R_M = \frac{X_0 \cdot E_s}{E_c} \tag{3.6}$$

where $E_s = m_e c^2 \sqrt{4\pi/\alpha} \simeq 21$ MeV is the scale energy.

The CMS ECAL detector (27) consists of three main components: the electromagnetic barrel calorimeter (EB), the electromagnetic endcap calorimeter (EE), and the preshower (PS) positioned in front of EE (Figure 17). Both EB and EE detectors are made of lead tungstate ($PbWO_4$) crystals, which are characterized by a short radiation length of 0.9 cm and a small Molière radius of 2.2 cm. The $PbWO_4$ crystals have a scintillation decay time very close to the nominal bunch separation of 25 ns, and emit a blue-green scintillation light with a maximum wavelength between 420 and 430 nm.

The EB contains 61200 crystals with a granularity in $\eta - \varphi$ of 170×360, providing a coverage of $|\eta| < 1.5$. To avoid the alignment of inter-crystal cracks with particle trajectories the crystals are tilted 3° from the nominal orientation. The $PbWO_4$ crystals have a trapezoidal form factor with a front face of 22×22 mm^2 and rear face of 26×26 mm^2. This translates into 0.017×0.017 in the $\eta - \varphi$ phase space. With a length of 23 cm, each crystal provides around 26 radiation lengths.
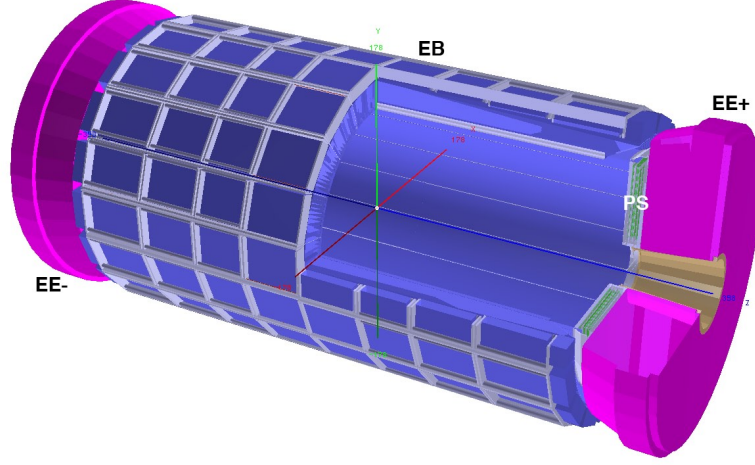
Figure 17. A perspective view of the CMS electromagnetic calorimeter.

The scintillation light in EB is collected and amplified by avalanche photodiodes (APDs) which are silicon photodiodes with a $p^+ - n - n^+$ structure. The penetrating photons create electron-hole pairs that are accelerated by the high potential difference in the pn junction. Multiple ionizations in the n-layer can provide very high signal amplifications.

The EE is made of 7324 PbWO$_4$ crystals arranged in a rectangular $x - y$ grid with a focus point of 1.3 m beyond the IP. Both EEs provide a coverage of $1.5 < |\eta| < 3.0$. The crystals in EE have a front face of about 29×29 mm^2 and a rear face of 30×30 mm^2. Around 25 radiation lengths are achieved in EE by using 22 cm long crystals. Due to its geometry, the EE granularity varies with η.

In EE the scintillation light is amplified by vacuum phototriodes (VPTs), which are photomultipliers equipped with a single gain stage. The number of photons emitted by crystals and the amplification of APDs or VPTs are temperature dependent. The nominal operating temperature for ECAL is 18 °C.

The main background for a Higgs search when $H \rightarrow \gamma\gamma$ is given by π^0 which decays immediately into two photons. In the central region the two photons are spaced enough such that the EB can resolve them. This is no longer true for the endcap region where the two photons are emitted almost in the same direction and EE can not resolve them. In this region an additional detector, the PS, is needed to improve the spatial resolution of EE.

With a thickness of 20 cm and a coverage of $1.6 < |\eta| < 2.6$, the PS is a two layer sampling calorimeter. Each layer has a lead absorber that initiates electromagnetic showers followed by silicon strip sensors that measure the energies of the showering particles and the transverse shower profile. The size of the silicon strip sensor is about 63×63 mm^2 with a nominal thickness of 320 μm. The first layer provides about $2X_0$ while the second one adds another X_0.

3.2.4   Hadronic Calorimeter

A hadronic calorimeter works similar to an EM calorimeter with the difference that the shower development is characterized by an interaction length. The absorption of hadrons in matter is described by:

$$N = N_0 \cdot e^{-x/\lambda} \tag{3.7}$$

where N_0 represents the initial number of hadrons and λ the average interaction length. The value of λ can be calculated as:

$$\lambda = \frac{A}{N_A \cdot \rho \cdot \sigma_{inel}} \tag{3.8}$$

where A represents the atomic weight, N_A the Avogadro's number, ρ the density of the material, and σ_{inel} the inelastic cross-section. The lateral width of a hadron shower is determined by the p_T transfer during nuclear interactions. The production of secondary particles consists mainly of charged and neutral pions, but includes also kaons, protons, and neutrons among other hadrons.

The CMS HCAL detector (28) has an average interaction length of 16.4 cm. Its main purpose is to measure jets and to aid in the reconstruction of neutrinos (as missing transverse energy). The HCAL is divided into a hadronic barrel calorimeter (HB) and two hadronic endcap calorimeters (HEs) (Figure 18).

The HB has a coverage of $|\eta| < 1.3$ and is made of 16 layers of brass absorber plates ($40 - 75$ mm in thickness) interleaved with tiles of plastic scintillation fibers. The segmentation in $\eta - \varphi$ space is 0.087×0.087. The first and last absorber layers are made of stainless-steel to provide additional structural strength. At $\eta \sim 0$ the absorbers provide around 6λ that increase to 11λ for $|\eta| \approx 1.3$. The presence of ECAL in front adds another λ. The scintillation light is collected and amplified by wavelength shifting fibers coupled to hybrid photodiodes (HPDs). The HPD consists of a photocathode held at -8 kV and positioned 3.3 mm in front of a silicon photodiode. The maximum achievable gain is around 2000.

In order to improve the containment of very energetic hadronic showers, and thus the measurement of the jet energy, an additional layer is added in the central region ($|\eta| < 1.3$) between the magnet and the muon system. At $\eta \approx 0$ the hadronic outer calorimeter (HO) consists of two layers of plastic scintillators at radii of 3.8 and 4.1 m. All other regions of HO have only one layer at a radius of 4.1 m. The presence of the magnet in front of HO provides an additional 1.5λ for the central region.

The HE is made of thicker brass absorber plates of about 79 mm interleaved with trays of plastic scintillation fibers. The coverage provided by both HEs is $1.3 < |\eta| < 3.0$ with a granularity of 0.087×0.087 for $|\eta| < 1.6$ and 0.17×0.17 for more forward regions. Like HB, the scintillation light is collected and amplified by wavelength shifting fibers
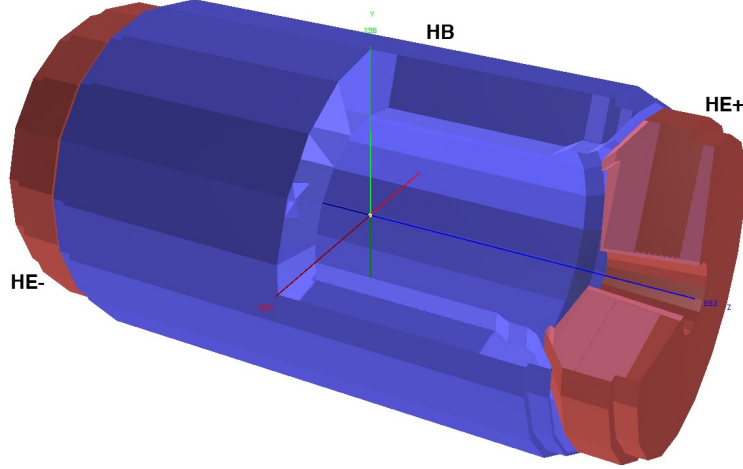
Figure 18. A perspective view of the CMS hadronic calorimeter.

coupled to HPDs. Both EE and HE provide enough material corresponding to about 10λ.

3.2.5   Forward Calorimeters

To extend the coverage of the calorimeter system up to $|\eta| = 5.0$, two hadronic forward calorimeters (HFs) are placed outside the muon endcaps, near the beam pipe, at a distance of 11.2 m from the IP. Because of high radiation doses each HF is made of steel absorbers as shower initiators and quartz fibers as active material. Each HF has a granularity in the $\eta - \varphi$ space of 0.175×0.175. With a radius of 1.3 m and a length of 1.65 m, the HF provides about 10λ.

When charged particles traverse the quartz fibers at a speed higher than the speed of light in the medium, they emit Cherenkov light. Half of the fibers extend over the full

length of the detector while the other half do not cover the first 22 cm measured from the interior face. Since the two sets of fibers are read out separately, EM showers can be distinguished from hadronic showers. This is possible because EM showers start to develop earlier and will deposit their energy mostly in the long fibers, while the hadronic showers will also deposit energy in the short fibers.

The CMS detector contains also two very forward calorimeter systems which are mainly used in the heavy ions and diffractive physics programs. The CASTOR system has two detectors placed on both sides of CMS, outside of HF at 14.4 m from the IP. Two zero-degree calorimeters (ZDCs) are positioned 140 m on both sides of the IP, between the two LHC beam pipes. The CASTOR detector provides a coverage of $5.2 < |\eta| < 6.6$ while the ZDCs extend it to $|\eta| > 8.3$. Both calorimeters have a design similar to HF with tungsten absorbers as shower initiators and quartz plates as active material.

3.2.6 Superconducting Magnet

The CMS superconducting magnet (29) has a compact design with an inner radius of 3 m and a length of 12.5 m. At a nominal current of 19.1 kA, an axial field of 4 T pointing along the positive z-axis is generated. This is achieved by using four layers of superconducting NbTi windings. The critical temperature of the superconductor in zero field is 9.2 K. To maintain its superconducting properties in a 4 T field the superconductor is cooled down to 4.5 K. Currently the magnet is operated at 3.8 T. The total weight of the solenoid is around 220 tonnes.
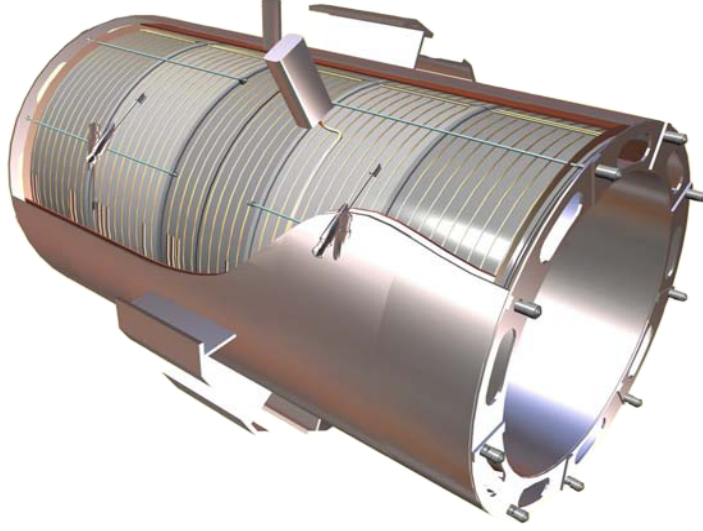
Figure 19. A 3D view of the CMS superconducting magnet.

The return flux of the magnet is mostly contained by an iron yoke intermixed with the muon system. The yoke has five wheels in the central region and two endcap disks with a total weight of 10 ktonnes. Both the wheels and the disks are split into three layers.

3.2.7   Muon System

Multiple SM and new physics signatures have muons in the final state. The CMS Muon Detector (30) was built to measure the position and momentum of muons. It represents a precise tracking system located outside of the superconducting solenoid.

The muon system (Figure 20) consists of a muon barrel (MB) with a coverage of $|\eta| < 1.2$ and two muon endcaps (MEs) that provide a coverage of $0.9 < |\eta| < 2.4$.
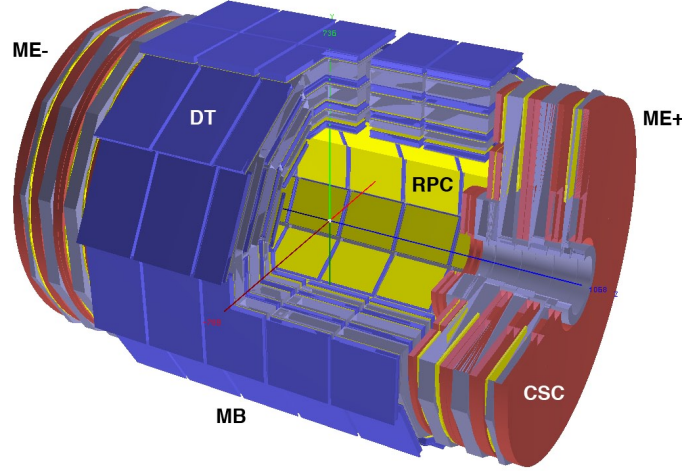
Figure 20. A perspective view of the CMS muon system.

Four muon stations made of drift tube (DT) chambers intermixed with the iron yoke are used to measure tracks in the MB section. Each of the three inner stations consists of 60 DT chambers while the outer station has 70. Each DT chamber is made of two or three super layers (SLs) depending on the location in the detector. Further, each SL has four layers of rectangular DTs. The position of DTs in each layer is shifted half a cell width with respect to the neighboring layers in order to eliminate the cracks between them.

The outer SLs in the chamber are oriented such that the anode wires are aligned to the beam pipe. This orientation allows the measurement of the radial and the azimuthal position of muon tracks. The three inner stations have DT chambers with an additional SL located between the two outer SLs. The orientation of the middle SL is tilted 90° to

allow the measurement of the z-position of muon tracks. Each SL provides an excellent time resolution of the order of a few nanoseconds.

The DT cell has a transverse dimension of 21 mm and an anode wire of 2.4 m in length. It is filled with a gas mixture of 15% Ar and 85% CO_2 providing a drift time of about 380 ns. When a muon traverses a DT it ionizes the gas mixture (26). The created electrons (ions) are accelerated by the existing electric field towards the anode (cathode). The accelerated electrons (ions) will ionize further the gas molecules and give rise to multiple EM showers. Each charged particle is then collected with a delay corresponding to its relative position to the collecting electrode. The distribution of the collected charged density is used to determine the track position inside the DT.

Due to a high muon rate and a large anisotropic magnetic field in ME, the DT chambers are replaced by trapezoidal cathode strip chambers (CSCs). The ME has four disk stations perpendicular to the beam line. The CSC is a multi-wire proportional chamber that contains six planes of gold plated tungsten wires (anodes) interleaved with seven plates of cathode strips. The gas mixture used is made of 40% Ar, 50% CO_2, and 10% CF_4 providing a gain of the order of 10^4.

The wires run along the φ direction with a spacing of 3.2 mm, while the strips are aligned along radial directions with a gap of 0.5 mm between them. The track position along the wire is calculated by interpolating the measured charge distribution on cathode strips. This setup allows for a precise measurement of the position of muon tracks in

all three coordinates. The innermost CSCs, located inside the solenoid, have the anode wires tilted 29°. This modification is needed to make the electron drift path parallel to the strips for a precise measurement of the $r - \varphi$ coordinates.

A redundant muon detection system is intermixed with the DT and CSC chambers to provide a fast detection time needed for the muon trigger system. The resistive plate chambers (RPCs) are gaseous parallel plate detectors with a coarse spatial resolution (around 1.5 cm) but a very good time resolution (around 1.5 ns).

The gas mixture used consists of 96.2% $C_2H_2F_4$, 3.5% C_4H_{10}, and 0.3% SF_6. Each RPC module has a plane of strips that divides the 2 mm gas chamber into two sections. The charge avalanche created by an ionizing particle passing through the detector is read separately from each section.

The MB has six layers of RPC chambers with strips aligned parallel to the beam line. The two inner muon stations have two layers of RPCs on both side of the DT chambers. This setup provides enough hits to trigger even on muon tracks that may stop inside the iron yoke. The outer muon stations, on the other hand, have only one layer of RPC chambers.

In ME, three RPC stations are used. Every station contains trapezoidal RPC chambers arranged in three concentric rings. The strips in the RPC modules, in ME, are aligned radially and segmented in three parts to provide a finer position measurement.

CHAPTER 4

CMS TRIGGER SYSTEM

4.1 Trigger Overview

For a nominal bunch separation of 25 ns and one proton-proton interaction per bunch crossing the event rate becomes as high as 40 MHz. Furthermore, for a nominal luminosity of $\mathcal{L} = 10^{34}$ cm^{-2}s^{-1}, up to 20 proton-proton collisions are expected to occur at each bunch crossing, making the event rate even higher. Limitations in the computing power, the data transfer bandwidth, and the storage capacity of the CMS computing infrastructure require an online event selection system (trigger) to reduce the expected high event rate down to about $\mathcal{O}(200)$ Hz for future analysis.

The input event rate is reduced online in two steps: first by the Level-1 Trigger (L1T) and then by the High-Level Trigger (HLT). The L1T is designed to reduce the rate from about 40 MHz to no more than 100 kHz using high-speed custom-designed programable electronics. The HLT consists of about $\mathcal{O}(700)$ commercial computers that run a similar event reconstruction to what is used for offline analyses. Its role is to reduce the event rate down to about $\mathcal{O}(200)$ Hz.

The L1T decision is based on data from the calorimeter and muon detectors. It uses coarse segmentations and simple algorithms while the HLT makes use of the full detector readout.

4.2   Level-1 Trigger System

The L1T system (31) consists of three layers as shown in Figure 21. The first layer contains the trigger electronics that read out the information from calorimeter towers and muon chambers. In the second layer this information is used to construct different regional trigger objects characterized by energy or momentum, position and quality flags. The last layer contains the Global Muon (Calorimeter) Trigger which sorts the regional muon (calorimeter) objects according to their physics properties and quality flags.
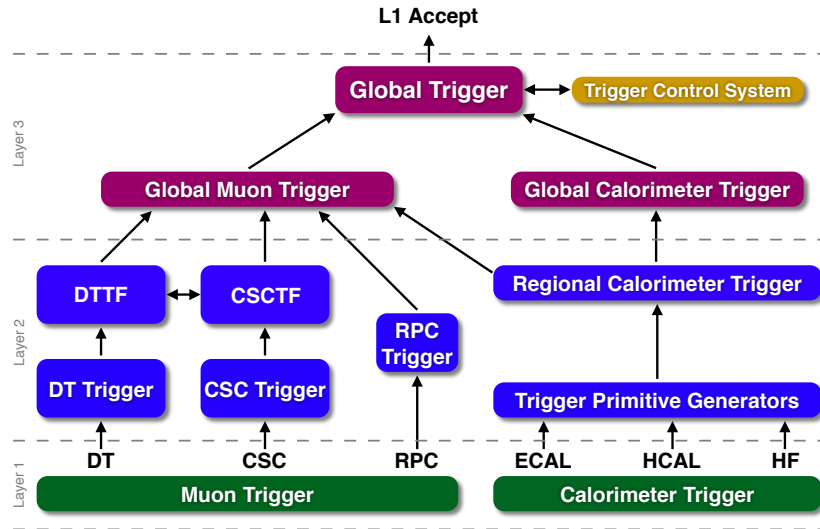
Figure 21. A schematic view of the Level-1 Trigger System.

The Global Trigger makes the decision to accept or to reject an event based on information received from the Global Muon and Calorimeter Trigger Systems. The L1T accept signal depends also on the Trigger Control System that provides information about the readiness of the sub-detectors and the Data Acquisition System (DAQ).

4.2.1   Muon Trigger System

The Level-1 Muon Trigger System uses information from all three types of muon detectors. The DT stations provide track segments and hit patterns in the $\eta - \varphi$ plane for the central region. Each track segment is characterized by position, direction, and a quality flag which reflects the number of drift cell hits. The drift tube track finder (DTTF) reconstructs muon tracks using track segments received from the DT stations and assigns to each one a p_T, η, φ, charge, and a quality flag.

The CSC detectors deliver 3D track segments for the endcap regions. Each track segment, defined by a position and a direction, is supplied to the cathode strip chamber track finder (CSCTF). Muon tracks are formed by matching the track segments. For the barrel-endcap overlap region, the DTTF and the CSCTF exchange information about reconstructed muon tracks. The CSCTF assigns to each muon track similar parameters as the DTTF. The quality flag for CSC tracks represents an expected coarse p_T resolution.

The RPC Trigger System is based on the spatial and time coincidence of hits in several RPC layers. Each muon track has a p_T, η, φ, charge, and a quality flag assigned according to the matched pattern. The quality flag reflects the number of hit layers.

4.2.2   Calorimeter Trigger System

The Level-1 Calorimeter Trigger System generates a trigger primitive for each trigger tower in both ECAL and HCAL. In the barrel region, a trigger tower corresponds to 5×5 ECAL crystals and one HCAL tower. In the $\eta - \varphi$ space this corresponds to 0.087×0.087. At more forward rapidities, the tower segmentation increases to $0.1 - 0.35$.

The ECAL trigger primitive construction starts with a strip of five crystals in φ. The summed analog-to-digital converter counts in the strip are converted to energy by taking into account the electronic gains and calibration coefficients of each crystal. The energy pulse is obtained by averaging five time-samples, each being 25 ns long. The total energy of the trigger primitive is calculated by summing the energies from five adjacent strips in η. A veto flag is set for each trigger tower if the highest two adjacent strips in the tower contain less than 90% of the total energy. This can be used to reject electron and photon candidates that result from physical jets.

The HCAL trigger primitives are calculated for the same trigger towers as for ECAL. In the central region this corresponds to a trigger primitive for each HCAL tower. For now, the HO information is not included in the Level-1 trigger decision. The HCAL energy pulse is calculated as the sum of two adjacent 25 ns time-samples.

The HF provides coarser trigger primitives calculated from $3\eta \times 2\varphi$ towers since they are used only for jet and energy sum triggers. The HF trigger primitives are forwarded directly to the Global Calorimeter Trigger.

The regional calorimeter trigger adds the energy of the ECAL and HCAL trigger primitives over 4×4 non-overlapping towers and forward these sums to the global calorimeter trigger. Electron and photon candidates are identified for $|\eta| < 2.5$. The resulting candidates are classified as isolated or non-isolated, based on the activity in the surrounding towers, and passed to the global trigger.

4.2.3   Global Trigger System

The Level-1 Global Muon Trigger System receives up to four candidates from each of the DTTF and CSCTF, and up to eight candidates (four in the barrel and four in the endcap) from the RPC trigger. Look-up tables are used to combine the candidates and to assign quality flags. The four highest p_T muon candidates, from all regions, are forwarded to the Global Trigger.

The Level-1 Global Calorimeter Trigger System sorts the electron and photon candidates based on the transverse energy (E_T) and forwards to the Global Trigger the highest four isolated and non-isolated candidates. The jet candidates are identified using a sliding window algorithm (32). Look-up tables are used to apply a p_T and η-dependent jet energy scale correction. The Global Calorimeter Trigger System provides to the Global Trigger the total and missing E_T, the jet multiplicity, and the total and missing H_T (scalar sum of E_T of jet candidates).

The main task of the Level-1 Global Trigger is to reject or to accept events from readout for further processing by the HLT. The Global Trigger can accommodate up to

128 algorithms. Some of them are simple algorithms based on p_T, E_T, or multiplicity thresholds, while others use more complex topologies. In addition, up to 64 algorithms can be simple on/off signals, which are called technical triggers. These triggers correspond to predefined hardware signals. The Global Trigger contains also random triggers that generate signals based on random number generators.

4.3   High Level Trigger

The HLT (33) consists of an event filter farm that runs a similar event reconstruction to what is used for offline analyses to select events for permanent storage. The software consists of different trigger paths, each designed to select a specific event type. A trigger path contains reconstruction modules and selection filters which are executed in a specified order. The first filter in an HLT path is usually a L1T decision.

The execution of a trigger path stops if one of the filters inside that path is not satisfied. If the same reconstruction module appears in more than one trigger path, that module is executed only once and the information is passed to all trigger paths. In this way, the execution time and resource usage are kept to a minimum. Based on the reconstructed objects used to trigger on, various HLT paths are available:

- jet triggers;

- missing E_T triggers;

- total and missing H_T triggers;

- muon triggers;

- electron and photon triggers;

- tau triggers;

- b-jet triggers;

- mixed triggers used to select multi-object topologies;

- technical triggers used for the alignment, calibration, and commissioning of the CMS detector.

The events that are selected by the HLT are saved in separate datasets. The grouping is done according to their offline usage. Because an event can be selected by multiple triggers, it can be saved in more than one dataset.

4.3.1 Data Acquisition System

A schematic view of the DAQ and its data flow is presented in Figure 22. Once a L1T accept signal is sent to HLT, the data from the front-end buffers are read and passed to the DAQ. The overall latency to deliver the L1T signal is set by the depth of the front-end pipelines and corresponds to 128 bunch crossings (3.2 μs).

The DAQ is comprised of eight identical slices that can run independently of each other. The first stage of the system is the event builder made of a front-end builder and a readout builder. The front-end builder is responsible with the transport of the event fragments from the cavern to the surface, where the filter farm is located. The fragments are then assembled in super-fragments and stored in the readout units. All super-fragments of an event are delivered to the same DAQ slice.
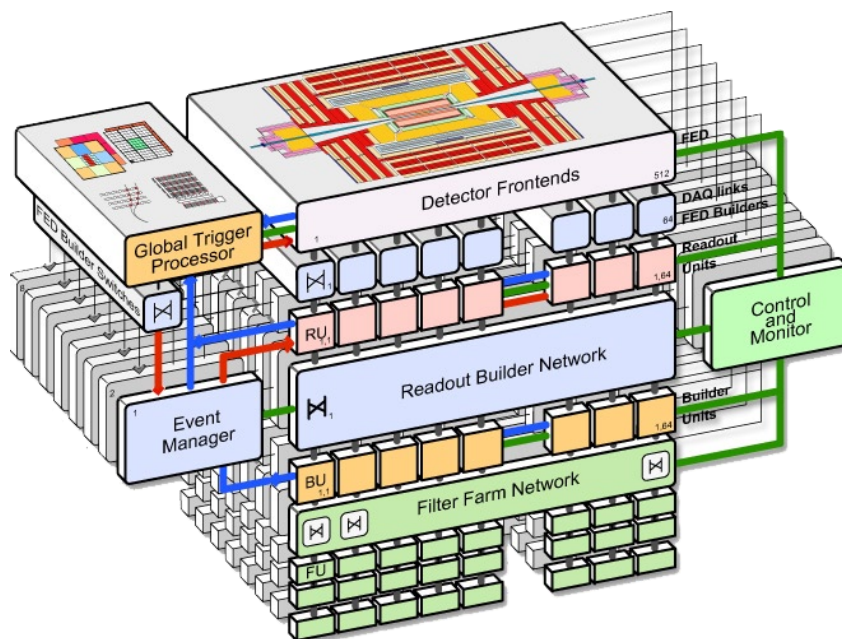
Figure 22. A schematic view of the Data Acquisition System.

A readout builder consists of multiple readout units, builder units, and a single event manager connected to a common switching network. Its purpose is to put together all super-fragments into one complete event. The event manager handles the data flow between different components and allocates events to builder units on request.

Complete events are transferred to different filter units for data consistency checks, reconstruction, and filtering. The primary goal is to reduce the event rate to manageable values for transfer and storage. The accepted events are forwarded to a storage manager; every DAQ slice being serviced by two storage managers. From there, the events are transferred to the CERN computing center for storage and further offline processing.

4.3.2   Jet Triggers

During the 2010 data taking period, the jets were reconstructed at HLT using an iterative cone algorithm (34) with a radius $R = 0.5$. The algorithm uses as inputs calorimeter towers with a minimum p_T of 0.5 GeV and a jet seed requirement of $p_T > 1$ GeV. The HLT jets were not corrected for the detector response; only the HF jets were scaled by a flat factor of 0.7.

Three categories of jet triggers are available for event selection: single jet triggers, dijet triggers, and multijet triggers. The single jet triggers have been used primarily in QCD jet analyses. Depending on the instantaneous luminosity, several single jet triggers are available. They are characterized by p_T threshold requirements at both L1T and HLT. The lowest threshold paths are usually Level-1 pass-through paths that have no additional requirement at the HLT. The higher threshold paths require an additional filter at the HLT.

A list of available single jet triggers for two instantaneous luminosities are presented in Table V ($L = 4 \cdot 10^{29}$ cm^{-2}s^{-1}) and Table VI ($L = 9 \cdot 10^{30}$ cm^{-2}s^{-1}). The tables list for each trigger the corresponding L1T condition, the prescales at both L1T and HLT, and the event rate. The Level-1 p_T threshold is chosen such that the L1T efficiency at the HLT threshold is at least 95%. As the instantaneous luminosity increases, the low threshold paths are prescaled (L1T and/or HLT) to keep the event rate within the allocated bandwidth.

The dijet triggers are designed to select unbiased events for the determination of the jet energy scale corrections. They require two HLT jets with an average E_T greater than a given threshold. The multijet triggers are used to select events where the total energy is shared among several jets. They are based on jet multiplicities above a given p_T threshold, scalar sums of calorimeter tower E_T, and scalar sums of jet p_T.

Path Name	Level-1 Seed	Level-1 Prescale	HLT Prescale	Rate (Hz)
HLT_L1Jet6U	L1_SingleJet6	1	200	5.26±0.04
HLT_L1Jet10U	L1_SingleJet10	1	40	4.74±0.04
HLT_Jet15U	L1_SingleJet6	1	10	6.37±0.04
HLT_Jet30U	L1_SingleJet20	1	1	5.73±0.04
HLT_Jet50U	L1_SingleJet30	1	1	0.98±0.02

TABLE V

SINGLE JET TRIGGERS FOR AN INSTANTANEOUS LUMINOSITY OF $4 \cdot 10^{29}$ cm^{-2}s^{-1}.

Path Name	Level-1 Seed	Level-1 Prescale	HLT Prescale	Rate (Hz)
HLT_L1Jet6U	L1_SingleJet6	2	10000	1.47±0.03
HLT_L1Jet10U	L1_SingleJet10	1	4000	1.32±0.03
HLT_Jet15U	L1_SingleJet6	2	400	2.04±0.04
HLT_Jet30U	L1_SingleJet20	1	40	3.50±0.05
HLT_Jet50U	L1_SingleJet30	1	1	23.37±0.12
HLT_Jet70U	L1_SingleJet40	1	1	6.80±0.07
HLT_Jet100U	L1_SingleJet60	1	1	1.71±0.03

TABLE VI

SINGLE JET TRIGGERS FOR AN INSTANTANEOUS LUMINOSITY OF $9 \cdot 10^{30}$ cm^{-2}s^{-1}.

CHAPTER 5

EVENT RECONSTRUCTION

5.1   CMS Computing Environment

The CMS computing infrastructure consists of multiple computing centers located throughout the world and connected by high-speed network links. Its role is to support the storage, transfer, and manipulation of the recorded data for the lifetime of the experiment.

A hierarchical structure of computing centers is used, with a single Tier-0 center located at CERN, a few Tier-1 centers at various national computing facilities, and several Tier-2 centers at different institutions.

The Tier-0 center accepts data from the DAQ and copies them to permanent mass storage. It also performs the first reconstruction of the raw data and copies the raw and reconstructed data to Tier-1 centers. With large computing facilities, the Tier-1 centers provide mass storage systems with robotic tape archives and high-speed network links. Their role is to store the raw data, perform additional data reconstruction when needed, and serve the Tier-2 centers with reconstructed and simulated data. The Tier-2 centers support physics analysis activities by providing user access to the various data samples. They are also used in the production and storage of MC data samples.

The CMS computing centers are integrated into a single coherent system through the use of Grid middleware (35). The Grid provides a standardized interface to the CMS storage and computing facilities and allows for remote job submission and data access.

The CMS data model uses an event container that holds all the relevant information about the recorded data. This includes the raw digitized data, reconstructed products, high-level analysis objects, and event provenance information. The data are stored as ROOT (36) files and can be visualized using the Fireworks (37) event display, which provides a simple interface with several graphical and textual views.

The CMS software model is based on a single executable and several event data modules that are configured at run time through a job specific configuration file. The event data modules are split into four categories: event data producers that add new objects to the event, event data filters that select events based on specific conditions, event data analyzers that produce summary information from events, and event data input/output modules for disk storage and DAQ.

CMS uses several event storage formats with different levels of detail. The RAW format is used to store the full recorded information from the detector along with the trigger information from the event. This format is permanently archived and occupies about 1.5 MB per event. The reconstructed (RECO) format is intended to store recon-structed information obtained by applying multiple pattern recognition and compression algorithms to the RAW data. The disk space occupied is about 0.5 MB per event. A

more compact event format is the Analysis Object Data which is produced by filtering the RECO data. It contains selected parameters of the high-level physics objects and usually occupies about 100 kB per event.

5.2   Track and Primary Vertex Reconstruction

An important step in the reconstruction of a proton-proton collision represents the reconstruction of charged particle tracks based on hits from the silicon detectors. When combined with information from the other sub-detectors, electrons, muons, taus, and charged hadrons can be reconstructed. In addition, primary and secondary interaction vertices can be determined.

The track reconstruction (38) at CMS is performed using a combinatorial track finder algorithm (39) that relies on a good estimate of the proton-proton interaction region (beamspot). Triplets of pixel hits, or pairs of pixel hits together with the beamspot position are used as seeds from which initial trajectories and their uncertainties are calculated. The initial trajectories are propagated outwards in a search for compatible hits. With each additional matching hit, the track parameters and uncertainties are updated. The search for compatible hits stops once the tracker boundary is reached, or no more matching hits are found. In the last step, the matched hits are fitted and the best estimate of the track parameters is obtained.

The CMS track finder algorithm consists of six iterations, which are optimized to find different categories of charged tracks. After each iteration, fake tracks are removed

based on the number of hits, the normalized χ^2, and the track compatibility. Hits that are assigned to real tracks are removed from the list after each iteration. In the first two iterations, pixel triplets and pairs are used as seeds, while the next iteration uses only pixel triplets to reconstruct low p_T tracks. To find displaced tracks, combinations of pixel and strip hits are used in the fourth iteration. The last two iterations use strip pairs to reconstruct tracks that lack pixel hits.

The primary vertex is determined using selected reconstructed tracks based on their transverse impact parameter significance (the closest distance between the track direction and the beam line), the number of pixel and strip hits, and the normalized track χ^2. Vertex candidates are constructed by grouping tracks that are separated along the z-axis by less than 1 cm. All candidates that have at least two tracks are fitted using an adaptive vertex fitter (40) and their positions and numbers of degrees of freedom are calculated. The number of degrees of freedom is defined as:

$$n_{dof} = 2\sum_{i=1}^{n} w_i - 3 \tag{5.1}$$

where w_i represents the compatibility of the ith track with the reconstructed vertex.

The vertex reconstruction efficiency (41) can be estimated by using a tag-and-probe method. The tracks used to reconstruct the vertex are split into two sets, with 2/3 of them assigned to a tag set and the rest to a probe set. This asymmetric splitting

increases the number of vertices with low track multiplicities. To reduce the fake rate of the reconstructed tracks, a minimum p_T cut of 0.5 GeV is applied to all tracks.

The tag and probe track sets are fitted independently with an adaptive vertex fitter. The vertex reconstruction efficiency is calculated as the probability for a probe vertex to match the original vertex given that the tag vertex was successfully reconstructed and matched. Figure 23 shows the primary vertex reconstruction efficiency as a function of the number of tracks, for both data and simulated events from PYTHIA8.
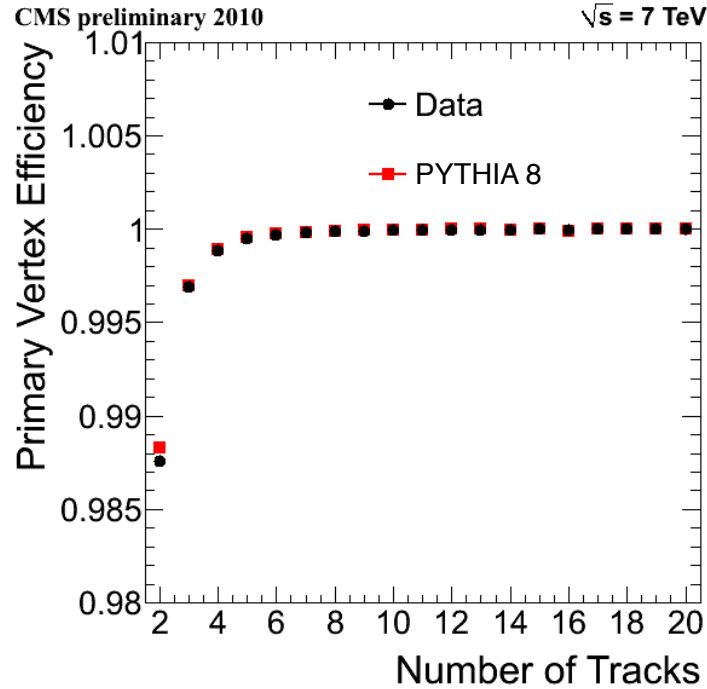
Figure 23. Primary vertex reconstruction efficiency as a function of the number of tracks used.

5.3   Photon and Electron Reconstruction

Photons and electrons can be reconstructed by measuring the energy deposits in the ECAL crystals. Usually, an EM shower spreads over a few ECAL crystals such that most of its energy is contained in a 3×3 array of crystals.

To extract the photon and the electron parameters, the ECAL energy deposits are grouped into superclusters by the CMS hybrid algorithm (42). The algorithm uses the $\eta - \varphi$ geometry of the ECAL crystals to extract information about the lateral shape in η of the EM shower and to find separated energy deposits in φ. For EB, the hybrid algorithm uses a 3×3 array of crystals, while for EE and PS a 5×5 array is used. The energy of the superclusters is corrected for energy losses due to showering in the tracker material and shower leakage in ECAL. The corrections are typically around 1%.

The tracker material, with about one radiation length, can initiate photon conversions and electron and positron bremsstrahlung. Photon conversions are characterized by a pair of opposite tracks with a small opening angle and a zero invariant mass.

Photons are reconstructed by summing the energy of the corrected superclusters. The lateral spread of the energy deposition is characterized by the energy contained in a 3×3 array of crystals, centered on the crystal with the highest deposited energy, divided by the total energy of the supercluster. Values close to unity are specific for isolated photons, while smaller values describe converted photons. If the percentage of this ratio is more

than 94% in the barrel and more than 95% in the endcap, the energy of an extended 5×5 array of crystals is used; otherwise, the supercluster energy is used (43).

Electrons are reconstructed using information from both ECAL and the tracking system. Depending on the method used, the electron reconstruction (44) can be ECAL-driven or tracker-driven. For low p_T electrons, the reconstruction starts with a tracking seed and tries to match it with an energy deposition in ECAL. For more energetic electrons, ECAL superclusters represent the seeds and the algorithm tries to match them with track candidates.

The comparison between a track candidate and an ECAL supercluster is based on a loose geometrical and energy-momentum matching. The difference between the energy measured by the ECAL supercluster and the momentum measured at the track origin depends on the energy loss in the tracker material. By combining both information, the measurement of the electron energy is improved.

5.4   Muon Reconstruction

Muon reconstruction (45) at CMS can be performed using either the muon detector, the silicon tracking system, or both. Based on this, several muon reconstruction methods are available.

If only the muon detector information is used, muons are reconstructed as standalone muon-track candidates. The muon reconstruction starts with the reconstruction of track segments from the muon chambers. The track segments found in the innermost muon

chambers are used as seeds to reconstruct muon trajectories. If no matching segments are found, the search continues with the next station until the boundary of the detector is reached. Once a muon-track is constructed, an extrapolation to the IP is performed and the track parameters are fitted again including information about the primary vertex.

The global muon reconstruction extends the trajectories of the muon-track candidates to include hits from the silicon tracker. Starting from a standalone muon-track candidate, the muon trajectory is extrapolated inwards by including the effects of multiple scattering and energy loss in the material. Based on the extrapolated trajectory, a region of interest is defined inside the silicon tracker and a regional track reconstruction is performed. If a matching track is found in the silicon tracker, the muon and tracker candidates are combined and fitted. This procedure improves the momentum reconstruction of very high p_T muons.

Similar to the global muon reconstruction, tracker muons are reconstructed using both the silicon tracker and the muon detector. In this algorithm, all tracks from the silicon tracker with $p_T > 0.5$ GeV are considered as possible muon candidates and are extrapolated outwards until they reach the muon detector. If at least one track segment in the muon detector matches the extrapolated track, the corresponding track is considered a tracker muon candidate. This approach works better for low p_T muons since it requires only a single track segment in the muon detector.

At the end, all muon candidates are combined into one single collection. The tracker muon and the global muon candidates that share the same tracks from the silicon tracker are merged. Similarly, standalone muon-track candidates which are not part of the global muon candidates are merged with tracker muon candidates if they have a common track segment in the muon detector.

5.5   Jet Reconstruction

The hadrons that emerge from the hard scatter appear in the detector as localized sprays of particles which are identified as jets. By studying these jets, various kinematic properties of the emerging partons can be extracted.

At CMS, several jet reconstruction algorithms are available. The most common ones are: the anti-k_t algorithm, which is described in Section 5.5.1, the seedless infrared-safe cone algorithm (46), and the iterative cone algorithm (34), which was used by the HLT during the 2010 data taking period.

Depending on the inputs used by the jet reconstruction algorithms, several types of jets are available at CMS: calorimeter jets, jet-plus-track, track jets, particle flow (PF) jets, and generated (particle) jets.

Calorimeter jets are reconstructed using only the information from the ECAL and HCAL detectors. Section 5.5.2 describes in more detail this jet type.

In the jet-plus-tracks algorithm (47), calorimeter jets are matched with charged parti-cle tracks based on the distance between the jet axis and the track in the $\eta-\varphi$ plane. The

momenta of matched charged particle tracks are then used to improve the measurement of the jet energy and position.

Another category of jets are the track jets (48), which are reconstructed based solely on the information from the tracking system. These jets are useful in the validation of calorimeter jets, since no calorimeter information is used.

The PF algorithm, which is discussed in Section 5.5.3, combines the information recorded by all CMS sub-detectors in an effort to identify and reconstruct all particles in the event. At the end, a list of all reconstructed particles is made available to the jet reconstruction algorithm.

A MC-only type of jets are the generated (particle) jets. They are reconstructed using all stable particles from MC simulated events as inputs to various jet reconstruction algorithms.

5.5.1   Recombination Jet Clustering Algorithms

The recombination clustering algorithms (49) are the primary algorithms used at CMS to reconstruct jets. The clustering procedure is based on the distances d_{ij} between two objects i and j, and d_{ii} between the object i and the beam line.

$$d_{ij} = min\left(k_{t,i}^{2p}, k_{t,j}^{2p}\right)\frac{\Delta r_{ij}^2}{R^2} \tag{5.2}$$

$$\Delta r_{ij}^2 = (y_i - y_j)^2 + (\varphi_i - \varphi_j)^2 \tag{5.3}$$

$$d_{ii} = k_{t,i}^{2p} \tag{5.4}$$

where $k_{t,i}$ represents the transverse momentum of object i, y_i its rapidity, φ_i its azimuthal angle, and R the radius of the jet in the $y - \varphi$ space. At CMS, two R-values are used to reconstruct jets: $R = 0.5$ and $R = 0.7$. The rapidity is defined as:

$$y = \frac{1}{2}ln\left(\frac{E + p_z}{E - p_z}\right) \tag{5.5}$$

where E represents the total energy and p_z the projection of the momentum along the beam axis.

Depending on the value of parameter p, three jet clustering algorithms are defined:

- $p = 1 \rightarrow k_t$ algorithm;

- $p = 0 \rightarrow$ Cambridge/Aachen algorithm;

- $p = -1 \rightarrow$ Anti-k_t algorithm.

For all algorithms, the distances d_{ij} and d_{ii} are computed for all possible object pairs, and the smallest values are identified. If $d_{ij} < d_{ii}$, the objects i and j are merged together, otherwise object i is considered to be a jet and removed from the list. The same procedure is applied again until all objects are removed from the list.

In the case of the anti-k_t algorithm, low-k_t objects will cluster first around high-k_t ones, before clustering among themselves. If two high-k_t objects, a and b, are separated by a distance $\Delta r_{ab} > 2R$, all objects within a distance R around each high-k_t object will be merged together, resulting in perfectly conical jets in the $y - \varphi$ space. If the two high-k_t

objects are close to each other such that $R < \Delta r_{ab} < 2R$, then the shape of the resulting jets will depend on their transverse momenta. For $k_{t,a} \gg k_{t,b}$, jet a will be conical in the $y - \varphi$ space while jet b will be missing the objects in the overlapping region. When both high-k_t objects have similar transverse momenta, neither one will be reconstructed as conical jet since the overlapping region between the two high-k_t objects will be divided almost equally between the two jets. The two objects will be reconstructed as a single jet if they are closer to each other than a distance R.

5.5.2 Calo Jets

The reconstruction of calorimeter jets is based on energy deposits from the ECAL crystals and HCAL cells. These are combined into calorimeter towers, which group together one or more HCAL cells and the corresponding ECAL crystals. In the center region, a calorimeter tower is made of one HCAL cell and 5×5 ECAL crystals. For more forward regions, the association between HCAL cells and ECAL crystals is more complex.

Prior to the construction of calorimeter towers, each HCAL cell and ECAL crystal is passed through a selection criterion which is listed in Table VII. This is necessary to suppress contributions from calorimeter readout electronic noise. An additional cut on the calorimeter tower energy ($E_T > 0.3$ GeV) is also applied to reduce pile-up effects.

Calorimeter Subsystem	Threshold (GeV)
HB	0.7
HE	0.8
HO	1.1 - 3.5
HF (long fibers)	0.5
HF (short fibers)	0.85
EB	0.07
EE	0.3
$\sum_{crystals}^{tower}$ (EB)	0.2
$\sum_{crystals}^{tower}$ (EE)	0.45

TABLE VII

CALORIMETER TOWER ENERGY THRESHOLDS USED IN THE RECONSTRUCTION
OF CALORIMETER JETS.

Calorimeter jets are then reconstructed by applying one of the available clustering algorithm on the filtered list of calorimeter towers. Fake jets from electronic noise are eliminated through a set of selection cuts (50):

- the jet EM fraction, $f_{EM} > 0.01$ for $|\eta| < 2.4$;

- the fraction of energy contributed by the hottest HPD, $f_{HPD} < 0.98$;

- the number of reconstructed tracker hits carrying 90% of the jet energy, $n_{90hits} > 1$.

These selection cuts rely on the fact that a jet that originates from the collision should deposit some of its energy in the ECAL crystals, and should spread its energy over more

than one HCAL cell. It also assumes that a real jet should be detected by more than one subsystem.

5.5.3 Particle Flow Jets

The PF reconstruction algorithm (51) tries to reconstruct all particles that emerge from the collision, based on information from all CMS sub-detectors. These particles are then used to reconstruct jets.

Each particle will produce different PF elements, like a charged track, a calorimeter cluster, a muon track or a mixture of these, when interacting with the CMS detector. A calorimeter cluster is constructed starting from a seed, which corresponds to a calorimeter cell with a local maximum energy above 80 MeV for EB, 300 MeV for EE, and 800 MeV for HCAL. All neighboring cells, above the previous thresholds, that share at least one side with the seed, or the previously merged cells, are combined together.

The PF elements are grouped together using a link algorithm (51). A charged track is linked to a calorimeter cluster if it is found to be within the cluster boundary. If multiple tracks are linked to the same calorimeter cluster, the sum of their momenta is used when comparing with the cluster energy. When more than one calorimeter clusters are linked to the same charged track, the link with the closest cluster is kept. An ECAL cluster is linked to an HCAL cluster if the ECAL cluster lies within the boundary of the HCAL cluster. A charged track is linked with a muon track if a global fit of the two tracks returns an acceptable χ^2 (22).

Once the PF elements are linked, particles are reconstructed by the PF algorithm. A global muon becomes a PF muon if its momentum is compatible with the value measured solely by the tracker. Charged tracks that are linked to calorimeter clusters are used to reconstruct PF electrons. All remaining tracks that are linked to calorimeter clusters and not used to reconstruct PF electrons are defined to be PF charged hadrons.

The reconstruction of neutral particles requires a comparison between charged track momenta and calorimeter cluster energies. Since the calorimeter manifests a nonlinear response, cluster energies are first corrected (52). Figure 24 shows the raw and calibrated calorimeter response for the barrel and endcap regions.

The calorimeter clusters that are more energetic than the linked charged tracks give rise to PF photons and PF neutral hadrons. A PF photon is produced if the excess energy is less than the total ECAL energy of the cluster. Otherwise, the ECAL fraction of the excess is attributed to a PF photon and the remaining part to a PF neutral hadron. The remaining ECAL and HCAL clusters, which are not linked to charged tracks, give rise to PF photons and PF neutral hadrons respectively.

After all PF elements are processed, a list of PF particles is passed to the jet clustering algorithm and PF jets are reconstructed. Figure 25 shows the average contribution of each particle type in the reconstruction of PF jet energy as a function of η for jets with $p_T > 25$ GeV.
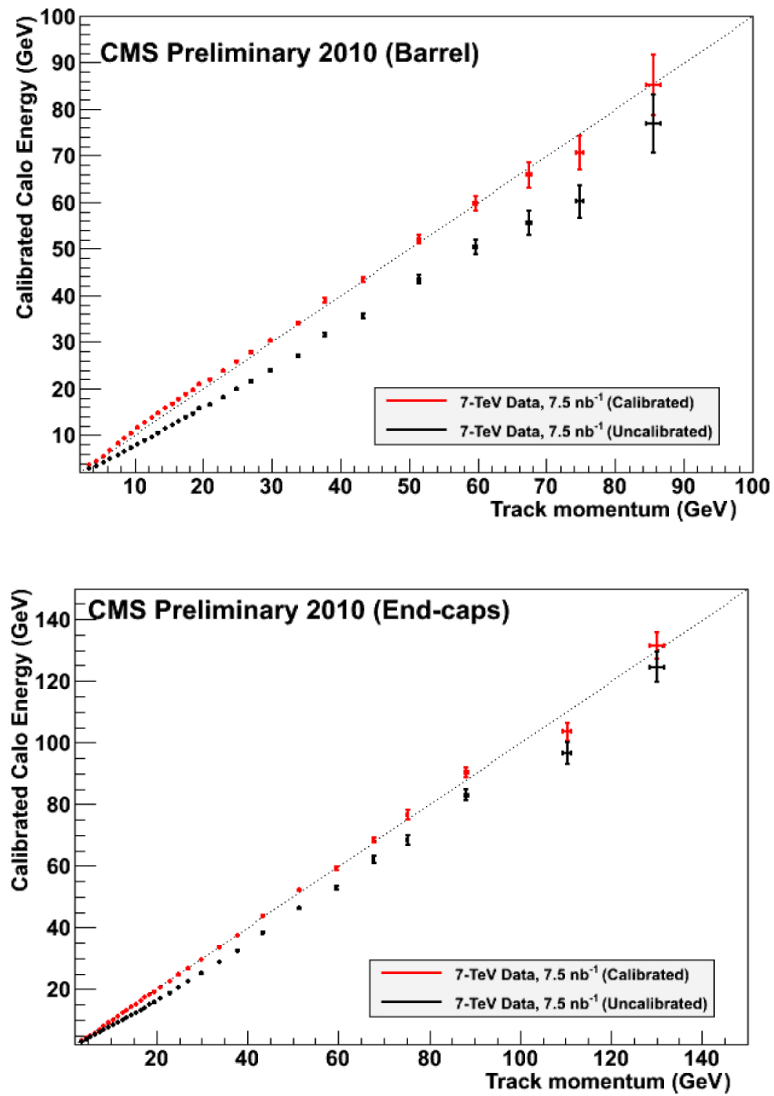
Figure 24. Raw and calibrated calorimeter response for the barrel region (top) and endcap region (bottom).
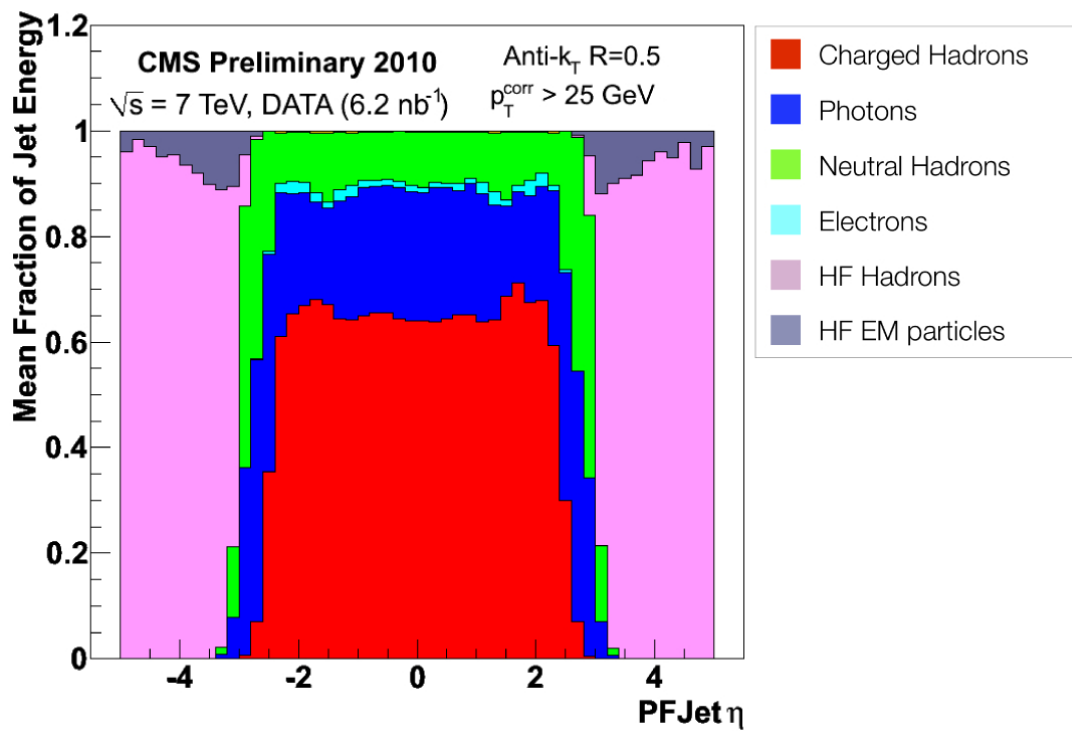
Figure 25. The average contribution of each particle type in the reconstruction of PF jet energy as a function of η for jets with $p_T > 25$ GeV.

Spurious jets from isolated noisy calorimeter cells and non-collision backgrounds are eliminated by a set of quality cuts. For $\eta < 2.5$, the PF jet identification is based on:

- the number of constituents, $N_{cand} > 1$;

- the number of charged hadrons, $N_{ch} > 0$;

- the fraction of energy contributed by neutral hadrons, $f_{nh} < 0.9$;

- the fraction of energy contributed by charged hadrons, $f_{ch} > 0.0$;

- the fraction of energy contributed by neutral EM particles, $f_{\gamma} < 0.9$;

- the fraction of energy contributed by charged EM particles, $f_e < 1.0$.

CHAPTER 6

JET PERFORMANCE

6.1 Jet Reconstruction Efficiency

The jet reconstruction efficiency is an important measure of the performance of the CMS detectors in identifying jets. A first approximation of the jet reconstruction efficiency can be extracted from MC by making use of generated jets.

To determine this efficiency, a spatial matching is performed between all generated and reconstructed jets. A jet matching efficiency is defined as the ratio of the number of generated jets matched to reconstructed jets within a given $\Delta R = \sqrt{\Delta\eta^2 + \Delta\varphi^2}$ and the total number of generated jets. Comparisons between matching efficiencies for calorimeter and PF jets in the barrel region for $\Delta R = 0.2$ and $\Delta R = 0.5$, as a function of the generated jet p_T, are shown in Figure 26.

For $\Delta R = 0.2$, the matching efficiency for calorimeter and PF jets reaches 100% at approximately 80 GeV and 50 GeV, respectively. If the matching requirement is relaxed to $\Delta R = 0.5$, the matching for calorimeter jets is fully efficient at approximately 40 GeV, and for PF jets at approximately 20 GeV.

Appendix A contains a description of a tag-and-probe method used to extract the calorimeter jet reconstruction efficiency from data. When the effect of the ΔR matching is removed, the reconstruction of PF jets is found to be fully efficient for $p_T > 20$ GeV.
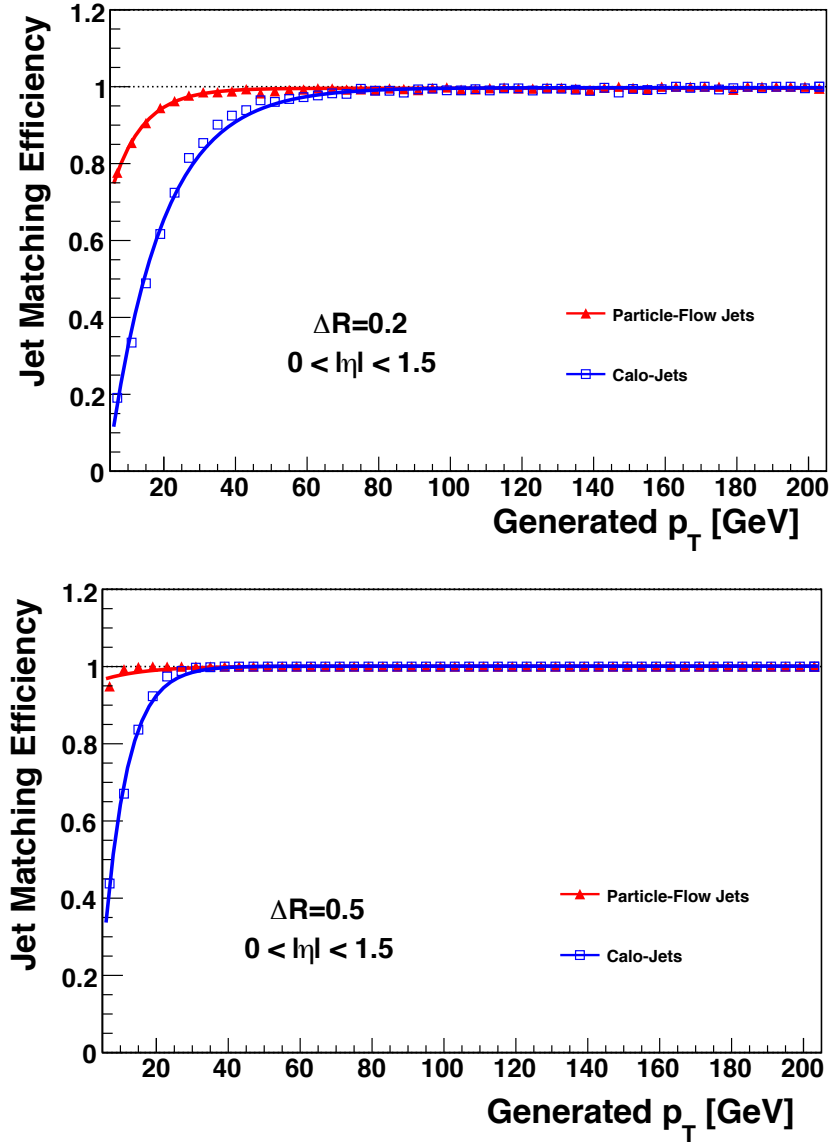
Figure 26. Jet matching efficiency for calorimeter and PF jets in the barrel region for $\Delta R = 0.2$ (top) and $\Delta R = 0.5$ (bottom), as a function of generated jet p_T.

6.2   Jet Energy Scale

The energy of a reconstructed jet is typically lower than the true jet energy due to losses in dead material and the non-uniform and non-linear response of the CMS detector. In addition, electronic noise and pile-up can also alter the jet energy.

Reconstructed jets are calibrated for these effects, on average, using a factorized approach, which is illustrated in Figure 27. First, an offset correction removes from the jet energy the contributions from electronic noise and pile-up. Then, MC-based corrections flatten the jet response in η and correct the p_T of the reconstructed jets to the corresponding generated jets. Finally, residual corrections that account for differences in the jet response between data and MC are applied. These corrections are described in more detail in the following sections.

6.2.1   Offset Correction

The offset correction (53) is the first step in the energy calibration of a reconstructed jet. It can be determined employing a method based on the jet area (54).

The effects of electronic noise and pile-up are simulated by adding a large number of low-p_T particles in the event, before reconstructing the jets. For each event, these contributions are quantified by determining the average p_T density per unit area.

The jets are reconstructed using a k_t jet clustering algorithm (Section 5.5.1) with a distance $R = 0.6$ and the average p_T density is estimated. The k_t algorithm is a proper choice since it naturally clusters a large number of low-p_T jets.
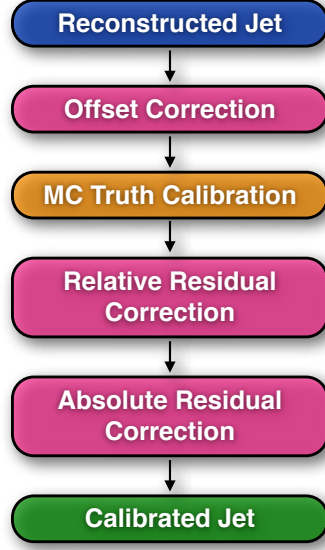
Figure 27. Jet energy scale calibration procedure.

For each event, the p_T density is calculated as the mean of the $p_{T,j}/A_j$ distribution, where A_j represents the area of jet j. Figure 28 shows the PF p_T density as a function of the leading jet p_T for several pile-up conditions. The average correction factor for each jet is determined as:

$$\mathcal{C}_{area} = 1 - \frac{A_j \cdot (\rho - \langle \rho_{UE} \rangle)}{p_{T,raw}} \tag{6.1}$$

where ρ represents the measured p_T density, $p_{T,raw}$ the uncorrected jet p_T, and $\langle \rho_{UE} \rangle$ the p_T density component of the UE which is measured in events with only one reconstructed primary vertex.
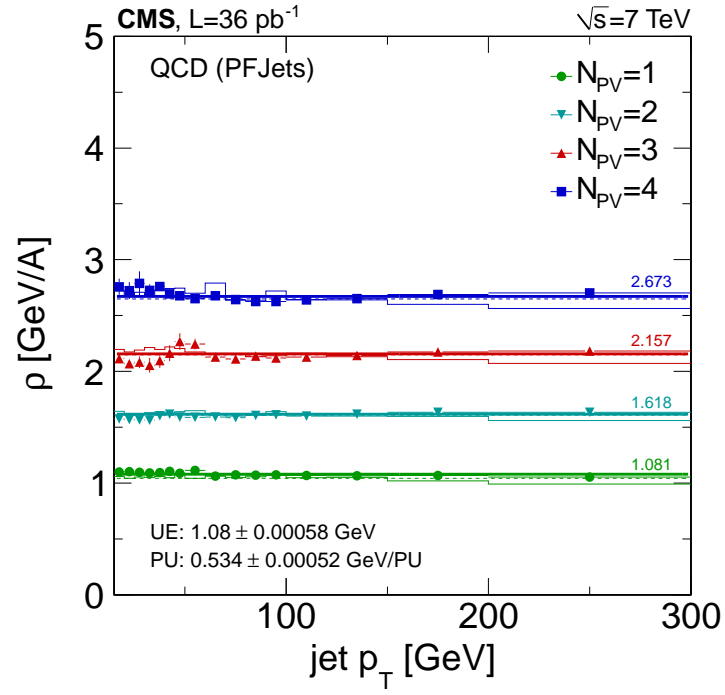
Figure 28. PF p_T density as a function of the leading jet p_T for several pile-up conditions. N_{PV} represents the number of reconstructed primary vertices per event.

6.2.2   MC Truth Calibration

The MC truth jet energy corrections are derived from QCD events generated with PYTHIA6. Generated jets are first matched to reconstructed jets within a $\Delta R = 0.25$ and the $p_{T,reco}/p_{T,gen}$ quantity is calculated for each pair of matched jets. The mean value of this distribution quantifies the true jet response. The inverse of the jet response represents the jet calibration factors, which are shown in Figure 29 for several jet types, as a function of the jet η, and in Figure 30 as a function of the jet p_T.
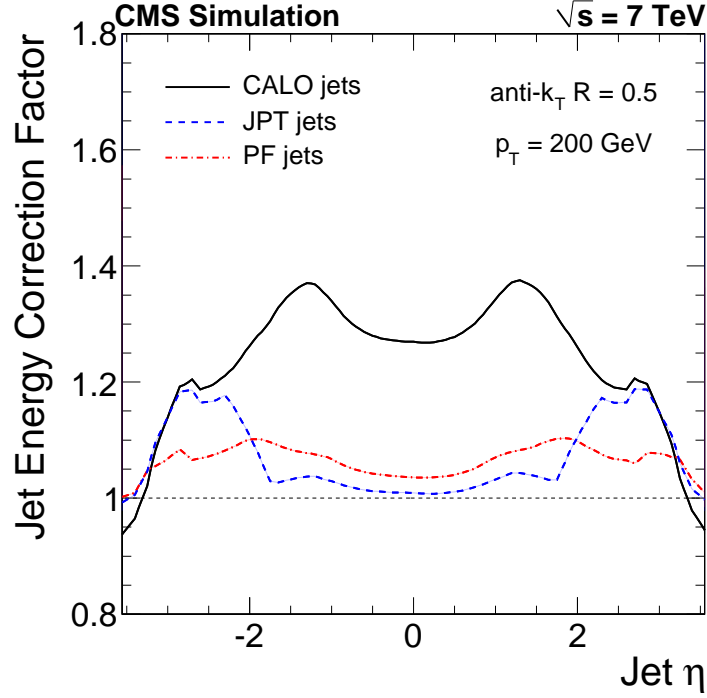
Figure 29. MC jet energy correction factors for several jet types as a function of η, for jets with $p_T = 200$ GeV.
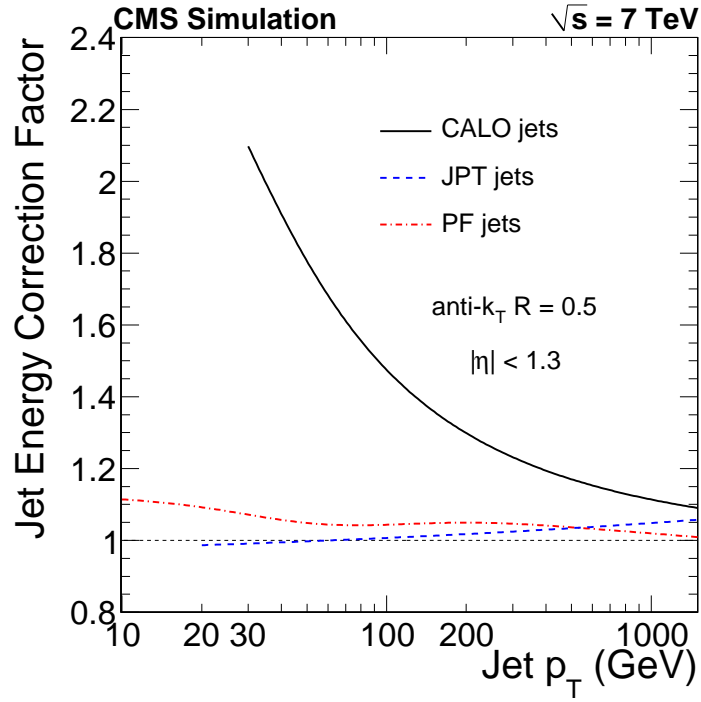
Figure 30. MC jet energy correction factors for several jet types as a function of jet p_T, for jets with $|\eta| < 1.3$.

The calibration factors for calorimeter jets are larger than for the other jet types because the calorimeter jets use only information from the CMS calorimeters, which exhibit a poor energy response. The features in Figure 29, around $|\eta| = 1.3$, are introduced by losses due to the interaction of particles with the tracker material and the barrel-endcap boundary of the calorimeter detector. The boundary between the endcaps and the forward calorimeters is also visible around $|\eta| = 3.0$. In the endcap and forward regions,

the calorimeter response gets better since jets of the same p_T are more energetic as η increases.

6.2.3   Relative Residual Correction

An η-dependent relative residual jet energy correction is applied after the coarse η and p_T dependence is removed by the MC truth calibration. This is achieved by determining the discrepancies between data and MC based on a dijet p_T balance technique (55). The method relies on the p_T balance of the two leading jets, in dijet events, with one jet in the central region of the detector ($|\eta| < 1.3$) and the other at arbitrary η. To reduce the effects of quark and gluon radiation, the third jet p_T is extrapolated to zero. The jet balance is calculated in bins of η_{probe} and $p_{T,dijet}$ as:

$$B = \frac{p_{T,probe} - p_{T,barrel}}{p_{T,dijet}} \tag{6.2}$$

and the relative jet response as:

$$R = \frac{2 + \langle B \rangle}{2 - \langle B \rangle} \tag{6.3}$$

where $\langle B \rangle$ represents the average value of the jet balance.

Figure 31 shows the discrepancies in the relative jet response between data and MC, and the size of the correction factors, for calorimeter and PF jets. The deviation of the corrected data from unity is due to the jet energy resolution which varies with η.
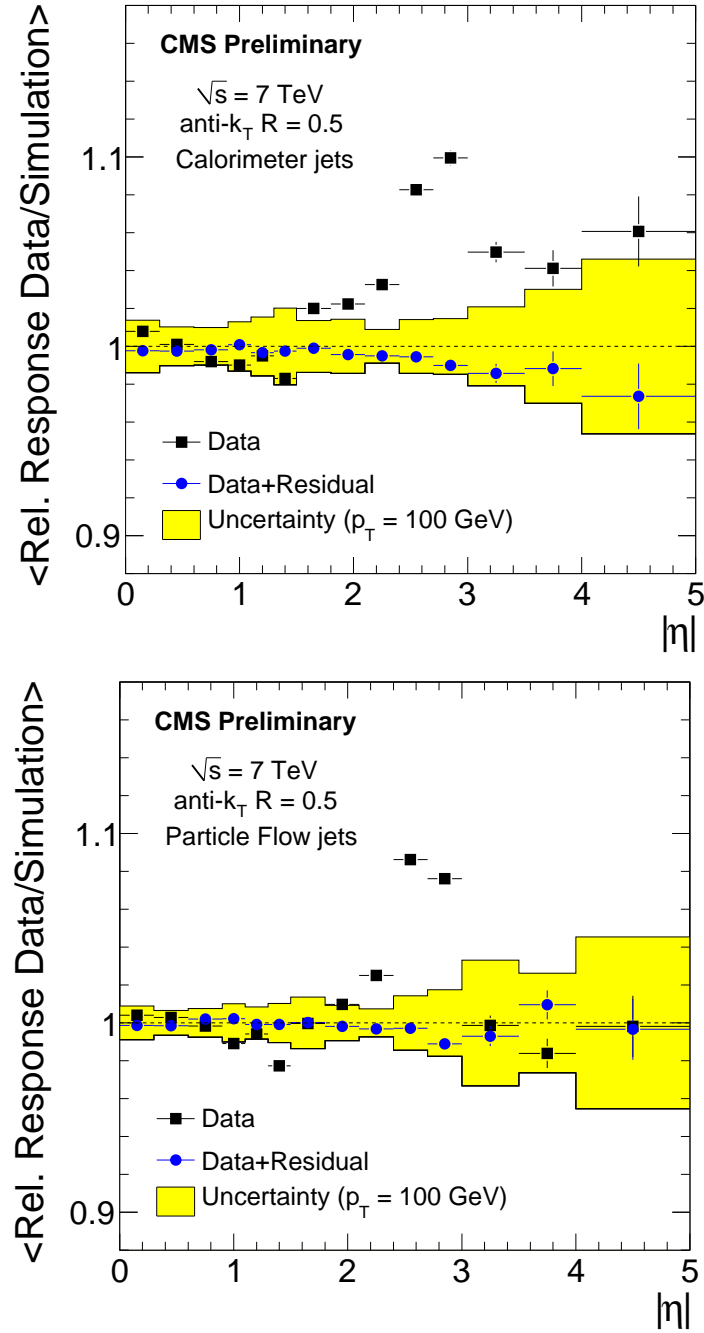
Figure 31. Relative jet response ratio between data and MC for calorimeter jets (top) and PF jets (bottom), for jets with $p_T = 100$ GeV.

To reduce statistical errors, the relative jet response is calculated in $|\eta|$ bins. The dominant systematic uncertainty is introduced by the uncertainty in the determination of the jet energy resolution. The extrapolation to zero of the third jet p_T introduces a small systematic uncertainty which is also included.

6.2.4   Absolute Residual Correction

The p_T-dependent absolute residual correction is needed to remove the differences in the jet response between data and MC. It is determined by measuring the jet response in the central region ($|\eta| < 1.3$) in $\gamma + jet$ events from data and MC using the missing transverse energy projection fraction (MPF) and p_T balance methods (55).

The MPF method relies on the fact that real $\gamma + jet$ events have no intrinsic missing transverse energy ($\not{E}_T$):

$$\vec{p}_{T,\gamma} + \vec{p}_{T,jet} = 0. \tag{6.4}$$

For reconstructed objects, the detector response spoils this balance such that:

$$R_\gamma \cdot \vec{p}_{T,\gamma} + R_{jet} \cdot \vec{p}_{T,jet} = - \vec{\not{E}}_T \tag{6.5}$$

where R_γ represents the photon response and R_{jet} the jet response of the detector. To reduce the effects of quark and gluon radiation, the second jet p_T is extrapolated to zero.

The p_T balance method relies on the fact that the p_T ratio of the photon and the leading jet should be approximately one in $\gamma + jet$ events. Figure 32 shows the PF jet

response ratio between data and MC for both MPF and p_T balance methods. The size of the absolute residual jet energy correction is obtained by fitting together both sets of points.
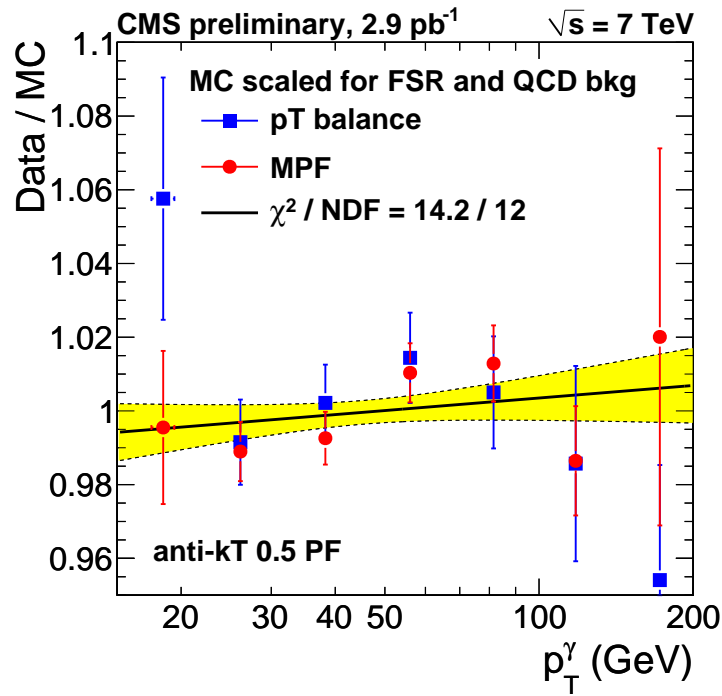
Figure 32. PF jet response ratio between data and MC for the MPF and p_T balance methods, and the size of the absolute residual jet energy correction.

Several contributions add to the total systematic uncertainty of the absolute residual correction. The MPF and p_T balance methods introduce uncertainties, mainly in the low-p_T region, due to differences between quark and gluon jets, parton radiation, and

photon identification. The uncertainty in the determination of the photon energy also impacts both methods. Another uncertainty that contributes mainly in the high-p_T region comes from the extrapolation of the jet response at high-p_T values in data. The offset uncertainty is relatively small and contributes only to the low-p_T region, while residual corrections are taken as an additional uncertainty. Figure 33 shows the total systematic uncertainty of the absolute residual correction for PF jets.
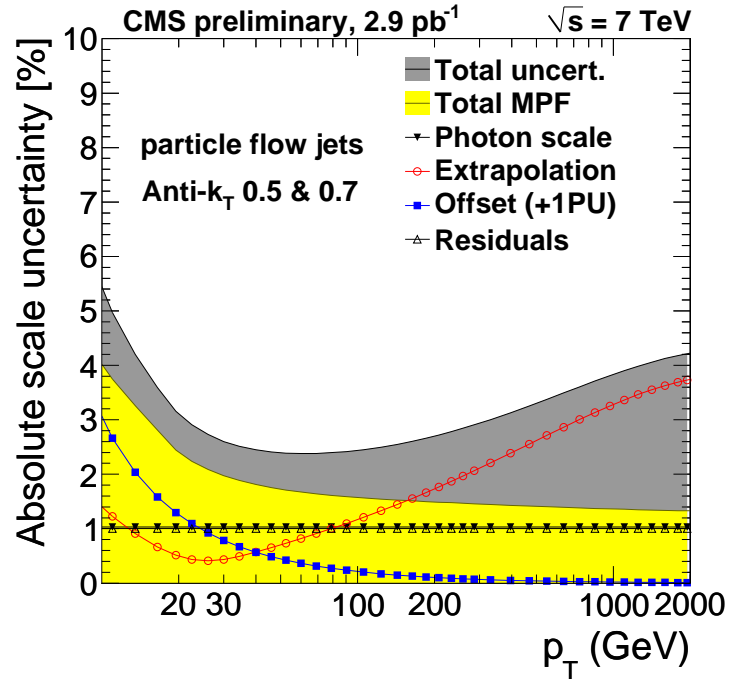
Figure 33. Total systematic uncertainty of the absolute residual correction for PF jets.

6.2.5   Total Jet Energy Correction

The total correction factor $\mathcal{C}$ is composed of the offset correction $\mathcal{C}_{offset}$, the MC truth calibration $\mathcal{C}_{MC}$, and the relative and absolute residual corrections $\mathcal{C}_{rel}$ and $\mathcal{C}_{abs}$:

$$\mathcal{C} = \mathcal{C}_{offset}\left(p_{T,raw}\right) \cdot \mathcal{C}_{MC}\left(p_T',\eta\right) \cdot \mathcal{C}_{rel}\left(\eta\right) \cdot \mathcal{C}_{abs}\left(p_T''\right) \tag{6.6}$$

where p_T' represents the jet p_T after the offset correction and p_T'' the jet p_T after all previous corrections.

The small relative and absolute residual corrections indicate that the MC truth calibration describes very well the jet energy scale in data. Figure 34 shows the total jet energy correction factors and their uncertainties for several jet types as a function of jet η and p_T.

6.3   Jet Energy Resolution

The jet energy resolution is extracted from data based on the dijet asymmetry method and compared to the MC truth jet energy resolution, which is derived from QCD dijet events generated with PYTHIA6. The width of the $p_{T,reco}/p_{T,gen}$ distribution, in bins of $|\eta|$ and $p_{T,gen}$, represents the MC jet p_T resolution. This is determined from generated jets matched to reconstructed jets within a $\Delta R = 0.25$.

Figure 34. Total jet energy correction factors and their uncertainties for several jet types as a function of the jet η (top) and jet p_T (bottom).
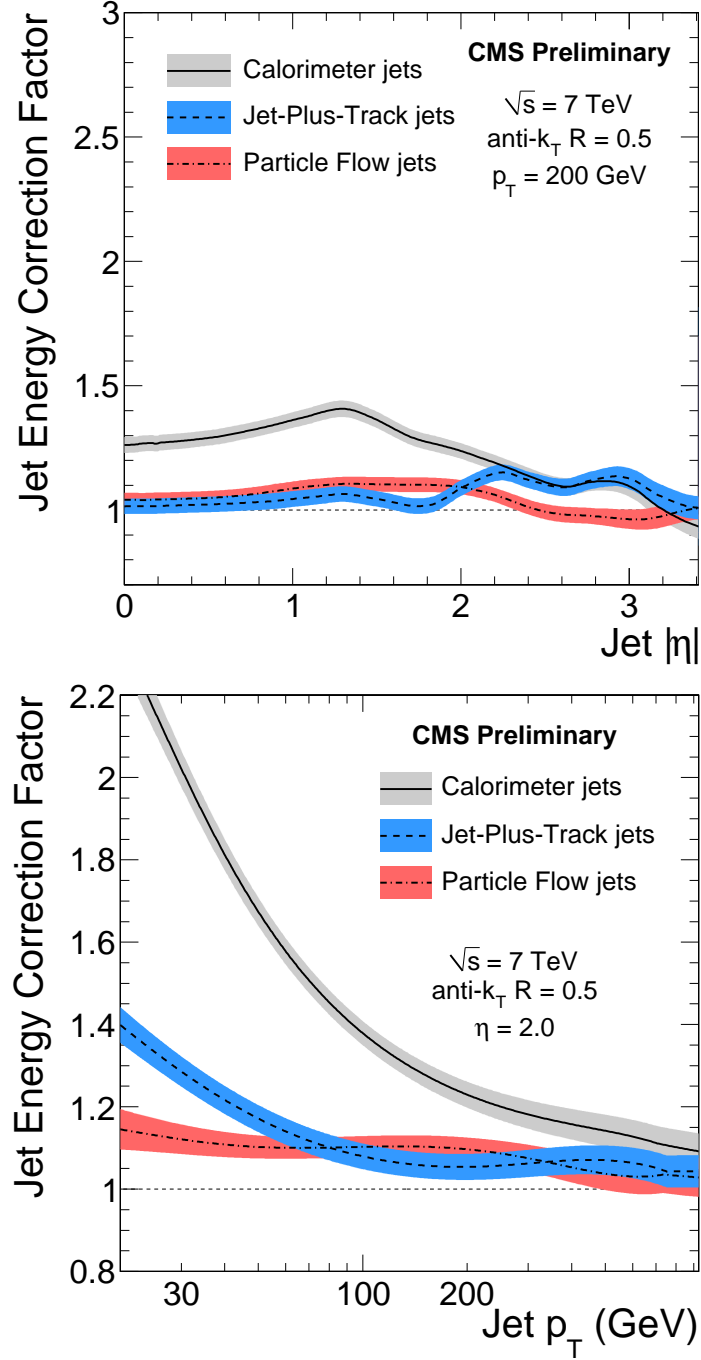
The dijet asymmetry method (56) is used to extract the jet p_T resolution from data. The method relies on the jet p_T asymmetry, which is defined as:

$$\mathcal{A} = \frac{p_{T,jet1} - p_{T,jet2}}{p_{T,jet1} + p_{T,jet2}} \tag{6.7}$$

where $p_{T,jet1}$ and $p_{T,jet2}$ represents the p_T of the two leading jets in the event, which are randomized. The variance of the jet p_T asymmetry is:

$$\sigma^2\left(\mathcal{A}\right) = \left|\frac{\partial \mathcal{A}}{\partial p_{T,jet1}}\right|^2 \cdot \sigma^2\left(p_{T,jet1}\right) + \left|\frac{\partial \mathcal{A}}{\partial p_{T,jet2}}\right|^2 \cdot \sigma^2\left(p_{T,jet2}\right). \tag{6.8}$$

In the limit of $\langle p_{T,jet1}\rangle = \langle p_{T,jet2}\rangle \equiv p_T$ and $\sigma\left(p_{T,jet1}\right) = \sigma\left(p_{T,jet2}\right) \equiv \sigma\left(p_T\right)$, the fractional jet p_T resolution is calculated as:

$$\frac{\sigma\left(p_T\right)}{p_T} = \sigma\left(\mathcal{A}\right)\sqrt{2}. \tag{6.9}$$

The true jet p_T resolution can be extracted only from events with exactly two jets. This can be achieved by applying a p_T cut on the third jet in the event. The jet p_T resolution is then measured for several p_T thresholds on the third jet. To reduce the quark and gluon radiation effects on the jet p_T resolution, the third jet p_T is extrapolated to zero (Figure 35).

The p_T imbalance that comes from physics effects (i.e., parton showering, hadronization) needs to be evaluated. The effect of such contributions is determined by applying
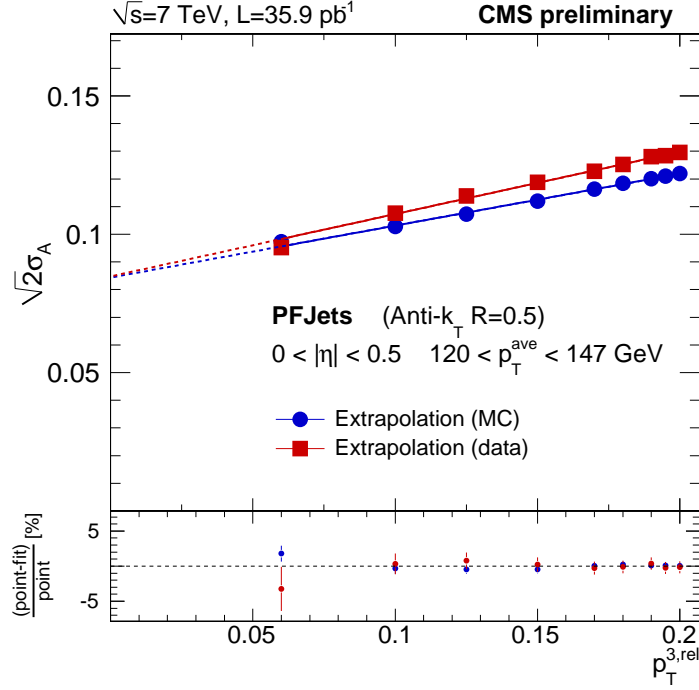
Figure 35. Extrapolations of $\sigma\left(\mathcal{A}\right)\sqrt{2}$ as a function of $p_{T,jet3}/p_{T,ave}$ to zero for PF jets. $p_{T,ave} = (p_{T,jet1} + p_{T,jet2})/2$.

the same technique on generated jets. The particle level resolutions are then subtracted

in quadrature from the reconstructed jet resolutions:

$$\left[\frac{\sigma\left(p_T\right)}{p_T}\right]^2 = \left[\frac{\sigma\left(p_T\right)}{p_T}\right]^2_{RECO} - \left[\frac{\sigma\left(p_T\right)}{p_T}\right]^2_{GEN} \tag{6.10}$$

The fractional jet p_T resolution is then fit with:

$$\frac{\sigma\left(p_T\right)}{p_T} = \sqrt{sgn\left(N\right) \cdot \left(\frac{N}{p_T}\right)^2 + S^2 \cdot p_T^{m-1} + C^2} \tag{6.11}$$

where N represents the noise parameter, S the stochastic parameter and C the constant parameter. To improve the fit for jet types that include information from the tracking system, an additional parameter m is introduced. The noise term includes contributions from electronic, digitization, and pile-up noise, and mostly influences the low-p_T region. Fluctuations in the energy deposited in the calorimeters and in the lateral shower spread contribute to the stochastic term, which dominates the high-p_T region. The constant term includes mostly inter-calibration errors and energy leakage, and is important for the very high-p_T region.

Figure 36 shows the jet p_T resolution from data compared to MC truth, for calorimeter and PF jets. To account for the small discrepancy between data and MC, a constant term is added to the MC truth. A likely cause of this discrepancy is an imperfect MC modeling of the CMS detector.

The p_T resolution is better for PF jets than for calorimeter jets at lower p_T values because the reconstruction of PF jets rely also on the tracker system, which has a much better p_T resolution than the calorimeter system. Therefore, the PF jets represent a better choice to perform various jet measurements.

6.4   Jet Position Resolution

The jet position resolution (57) in both η and φ is determined from QCD events generated with PYTHIA6. The method relies on a spatial comparison between generated
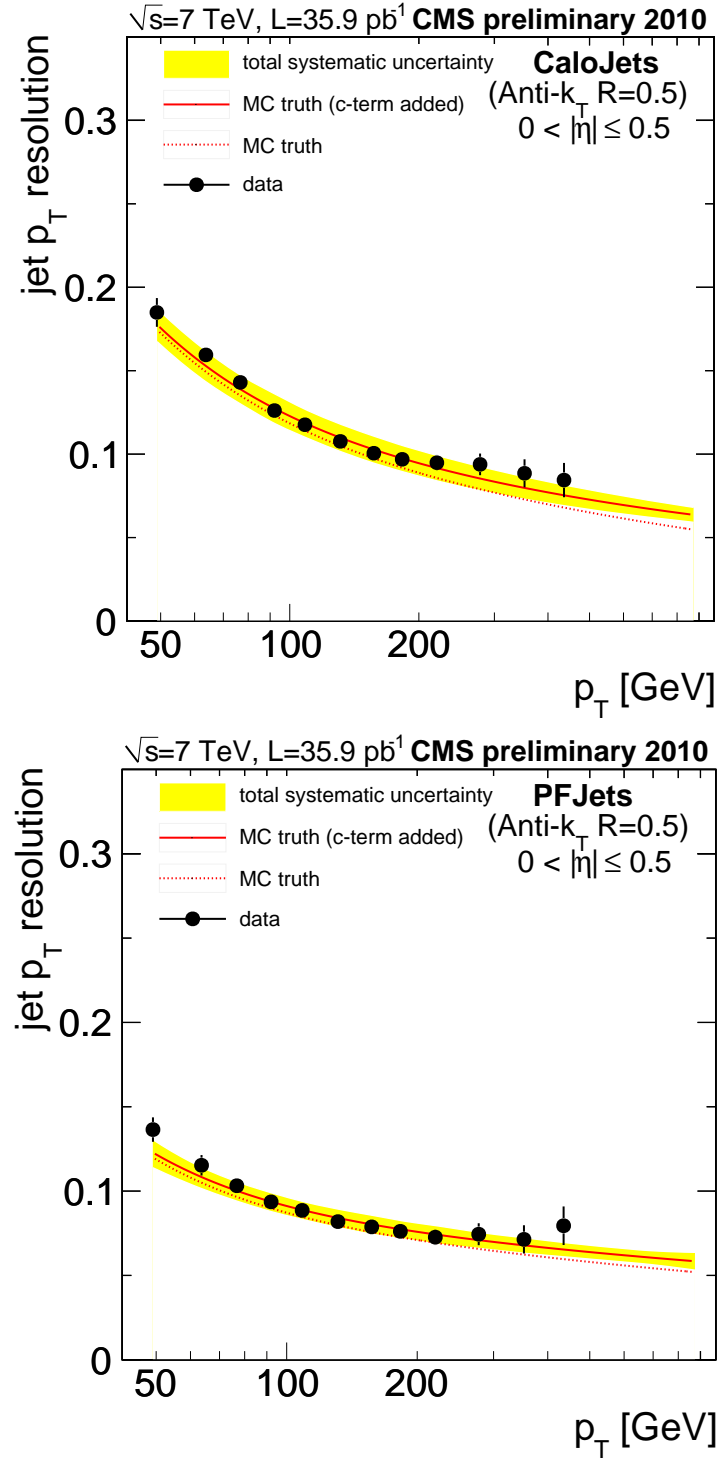
Figure 36. Jet p_T resolution from data compared to MC truth for calorimeter jets (top) and PF jets (bottom).

jets and reconstructed jets. A similar approach could be used in data to evaluate the position resolution for calorimeter jets by replacing the generated jets with track jets.

To determine the jet position resolution, generated jets are matched with reconstructed jets within a $\Delta R = 1.0$. An additional requirement of $\Delta\varphi(jet1, jet2) > 2.0$ is imposed on the two leading jets in order to select dijet events. The jet position resolutions are calculated as the means of the following distributions:

$$\Delta\eta = sign\left(\eta_{gen}\right) \cdot \left(\eta - \eta_{gen}\right) \tag{6.12}$$

$$\Delta\varphi = \varphi - \varphi_{gen}. \tag{6.13}$$

This is calculated for the two leading jets only. The sign of η_{gen} is included in the expression of $\Delta\eta$ to remove the bias of binning in $|\eta_{gen}|$.

Figure 37 shows the calorimeter and PF jet position resolutions in η as a function of generated jet p_T, for several η regions. Similar resolutions are showed in Figure 38 for jet φ position.
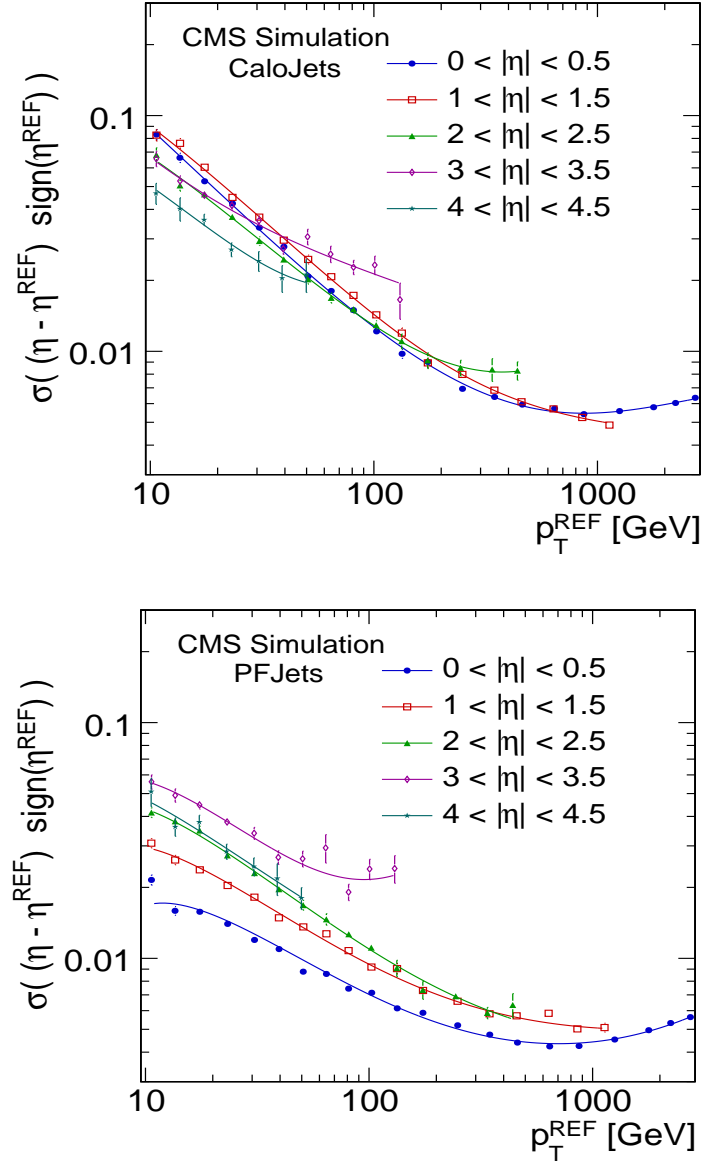
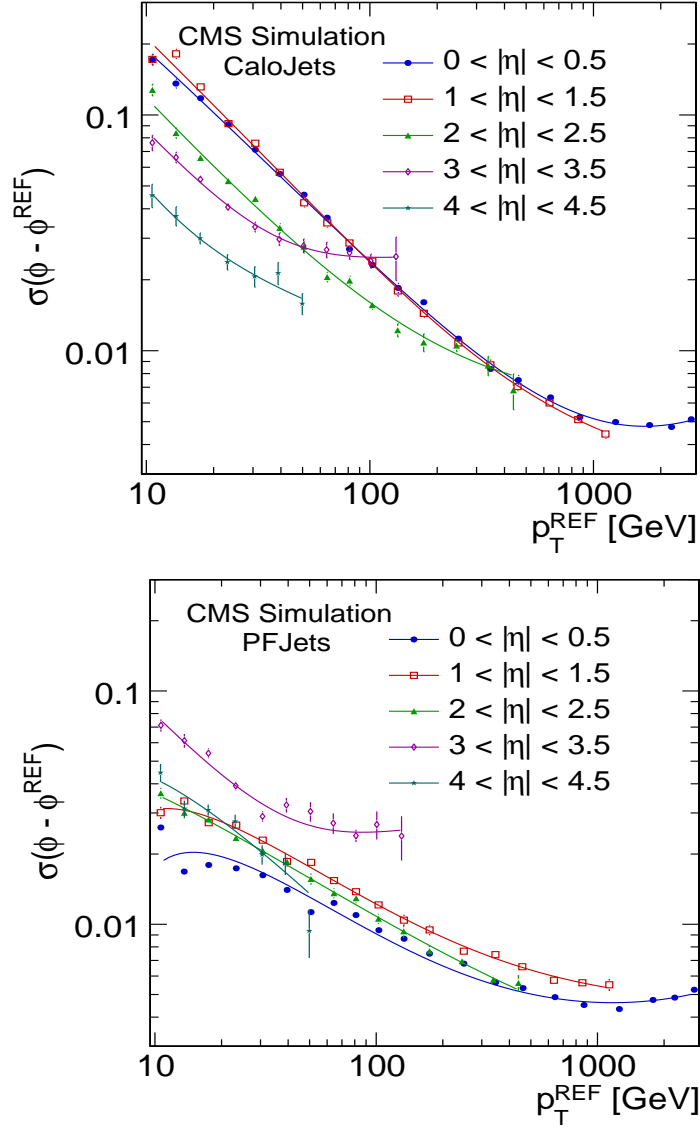Figure 37. MC truth η resolutions for calorimeter jets (top) and PF jets (bottom) in several η regions.

Figure 38. MC truth φ resolutions for calorimeter jets (top) and PF jets (bottom) in several η regions.

CHAPTER 7

DIJET AZIMUTHAL DECORRELATIONS

7.1 Event Selection

The analysis is based on an inclusive dijet event sample from the 2010 data taking period and corresponds to an integrated luminosity of 2.9 pb^{-1}. Only runs with all sub-detectors fully functional are considered. The selection of events is discussed in the following sections.

7.1.1 Online Selection

Events are selected using two inclusive single-jet triggers: HLT_Jet30U and HLT_Jet50U. The HLT_Jet30U trigger requires a L1T jet with $p_T > 20$ GeV and a HLT jet with $p_T > 30$ GeV, while the HLT_Jet50U trigger requires a L1T jet with $p_T > 30$ GeV and a HLT jet with $p_T > 50$ GeV. The higher p_T-threshold trigger is required since the lower one becomes prescaled at higher instantaneous luminosities.

The trigger efficiency for a given corrected p_T-threshold of the highest-p_T (leading) jet is measured using events selected by a lower-threshold trigger. Figure 39 shows the trigger efficiencies for HLT_Jet30U and HLT_Jet50U as a function of the offline PF jet p_T. HLT_Jet30U becomes 99% efficient starting with 78 GeV, while HLT_Jet50U becomes 99% efficient starting with 110 GeV.
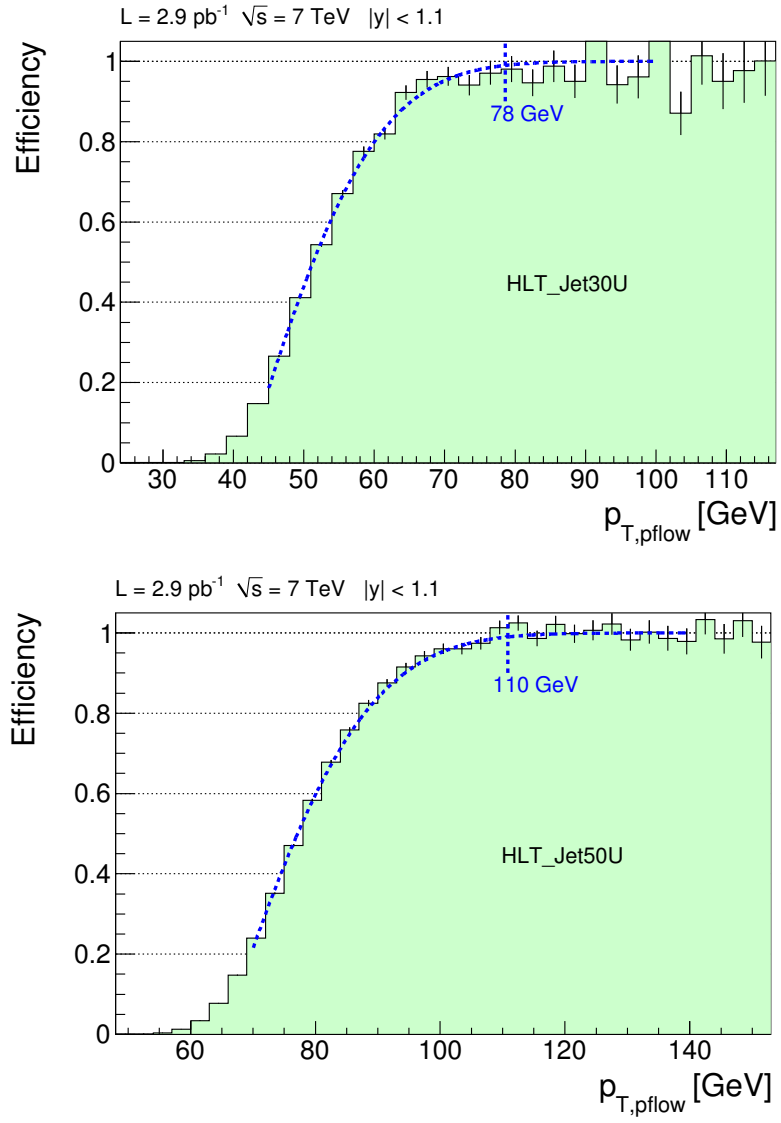
Figure 39. Trigger efficiency for HLT_Jet30U (top) and HLT_Jet50U (bottom) derived from data. HLT_Jet30U becomes fully efficient above 78 GeV, while HLT_Jet50U becomes fully efficient above 110 GeV.

7.1.2   Offline Selection

Jets are reconstructed offline using the anti-k_t jet clustering algorithm with a distance parameter $R = 0.5$. The four-vectors of particles reconstructed by the PF algorithm are used as inputs. The same jet clustering algorithm is also applied to final-state particles in MC event generators to obtain the particle-level jets.

The jet energy is calibrated following the procedure described in Section 6.2. For the 2010 data taking period, on average, only one additional interaction per event occurred. Given this low pile-up environment, the offset correction is not applied.

Spurious jets from noise and non-collision backgrounds are removed by applying a set of quality cuts, which are described in Section 5.5.3. In addition, the events are required to have a primary vertex reconstructed along the beam axis within 24 cm of the detector center and with $n_{dof} > 4$. The distributions from data for the PF jet identification cuts and the primary vertex selection cuts are shown in Appendix B. An additional filter that requires more than 10 good tracks with $p_T > 250$ MeV per event is applied to reject interactions from the beam halo.

Each event is required to have the two highest-p_T jets in the central region of the detector ($|y| < 1.1$). Furthermore, both jets are required to have $p_T > 30$ GeV. The same selection criterion is applied to all types of jets used.

The selected events are split into five mutually exclusive regions, based on the p_T of the leading jet ($p_{T,max}$) in the event. The lowest $p_{T,max}$ region is defined by the 99%

efficiency thresholds of the two single-jet triggers used. The number of events that pass the selection criterion for each $p_{T,max}$ region are listed in Table VIII, while Table IX contains the number of events rejected by different event requirements.

$p_{T,max}$ [GeV]	80 - 110	110 - 140	140 - 200	200 - 300	300 - ∞
Number of Events	60837	160388	69009	14383	2284

TABLE VIII

NUMBER OF EVENTS THAT PASS THE SELECTION CRITERION FOR EACH $p_{T,max}$
REGION.

$p_{T,max}$ [GeV]	80 - 110	110 - 140	140 - 200	200 - 300	300 - ∞
Primary Vertex Cut	9	18	11	1	0
1st Jet ID	36	118	82	13	13
2nd Jet ID	31	119	44	6	3

TABLE IX

NUMBER OF EVENTS REJECTED BY DIFFERENT EVENT REQUIREMENTS.

The data sample for the lowest $p_{T,max}$ region corresponds to 0.3 pb^{-1}, while for the other $p_{T,max}$ regions it corresponds to 2.9 pb^{-1}. The uncertainty on the integrated luminosity is estimated to be 11% (58). The selected events are part of the following runs:

- $138564 \leq N_{run} \leq 141881$, taken between June 25 and July 29, 2010

- $141956 \leq N_{run} \leq 144114$, taken between July 29 and August 30, 2010

7.2 $\Delta\varphi$ Distributions

The dijet azimuthal decorrelation probes different levels of parton radiation over its entire $\Delta\varphi_{dijet}$ region. In the absence of quark and gluon radiation, the shape of the $\Delta\varphi_{dijet}$ distribution corresponds to $\Delta\varphi_{dijet} = \pi$. Any additional parton radiation increases the tail of the $\Delta\varphi_{dijet}$ distribution towards smaller $\Delta\varphi_{dijet}$ values.

The raw dijet azimuthal decorrelations from data (L = 2.9 pb^{-1}), for all $p_{T,max}$ regions, are shown in Figure 40. The distributions are scaled by multiplicative factors for presentation purposes. As expected, the $\Delta\varphi_{dijet}$ distributions are strongly peaked at π and get narrower for higher $p_{T,max}$ regions.

7.3 Data to MC Comparisons

Multiple data to MC comparisons are performed in order to select MC event generators that describe the data better. The events simulated with these MC generators are used to correct the measured $\Delta\varphi_{dijet}$ distributions back to particle level. Therefore,
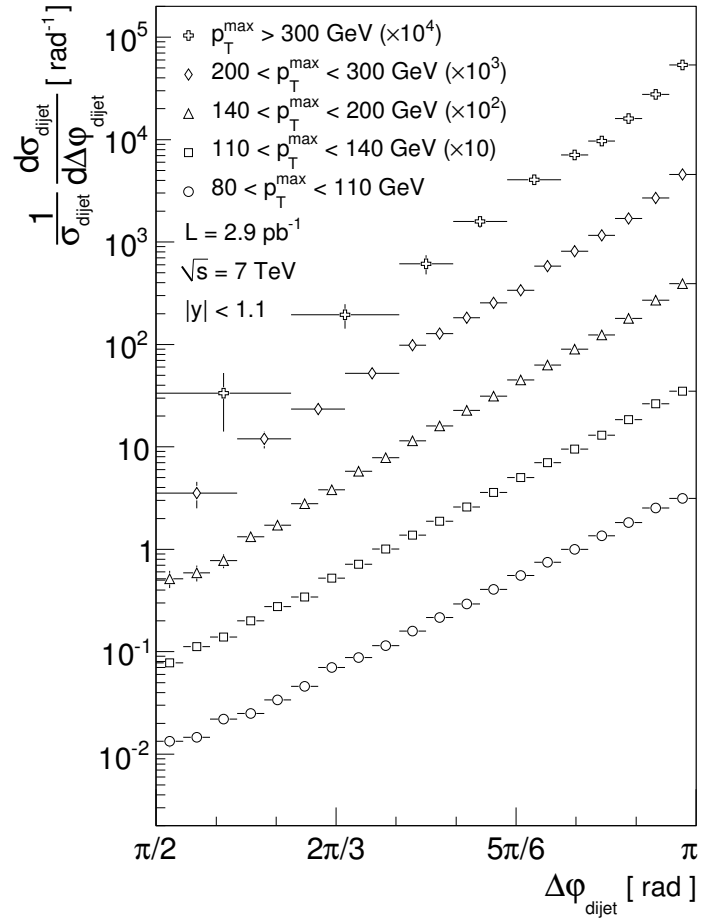
Figure 40. Uncorrected dijet azimuthal decorrelations from data (L = 2.9 pb^{-1}) for several $p_{T,max}$ regions.

various comparisons of jet kinematic distributions between data and several MC generators (PYTHIA6 tune D6T (59), PYTHIA6 tune Z2[1], PYTHIA8, HERWIG++, and MADGRAPH) are performed. The MC distributions are obtained using generated jets with their momenta, energies, and positions smeared according to the measured p_T and position resolutions. These comparisons are shown in Appendix C. Included are comparisons for the $\Delta\varphi_{dijet}$ distributions, the first, second, and third jet p_T distributions, the first and second jet rapidity distributions, and p_T ratios between the second and first jet and third and second jet. For each observable, a direct comparison and ratios between data and the MC generators are shown.

The $\Delta\varphi_{dijet}$ distributions and the first jet p_T distribution are well described by all MC generators. However, differences between MC and data become more visible for the second and third jet p_T distributions, as well as for the p_T ratio distributions between the leading jets. The rapidity distributions for the first and second jet show good agreement with data, for all tested MC generators.

Based on these comparisons, the PYTHIA6 tune D6T and HERWIG++ MC generators are found to better describe the data, and therefore are used to extract the unfolding corrections and to determine the systematic uncertainties associated with these measurements.

---

[1]The PYTHIA6 tune Z2 is identical to the tune Z1 (59) except that Z2 uses the CTEQ6L PDFs while Z1 uses CTEQ5L

7.4   Pile-up Effects

The pile-up effects are introduced by the presence of more than one proton-proton interaction during a time interval corresponding to the response time of the CMS detector. These effects can be estimated by counting the number of good primary vertices in each event (Figure 41). The pile-up effects are probed by comparing the dijet azimuthal decorrelations for events with only one good primary vertex and events with multiple good primary vertices.
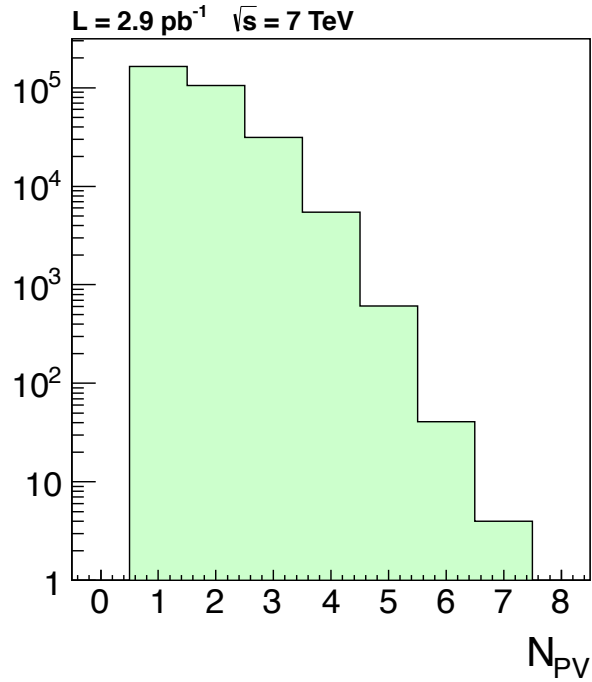

Figure 41. Number of good primary vertices per event for the data sample used.

Figure 42 shows a direct comparison for the $\Delta\varphi_{dijet}$ distributions between the two cases of pile-up conditions, for all $p_{T,max}$ regions, while Figure 43 shows the ratios between them. Based on these comparisons, no significant pile-up effects on the $\Delta\varphi_{dijet}$ distributions are observed.

7.5   Resolution Effects

Event migration effects due to the finite jet p_T and position resolutions of the detector have a sizable impact on the $\Delta\varphi_{dijet}$ distributions. The dijet azimuthal decorrelations are sensitive to the jet p_T resolution because fluctuations in the jet response can cause low-p_T jets to be misidentified as leading jets and events to migrate between different $p_{T,max}$ regions. The finite resolution in azimuthal angle causes event migration between $\Delta\varphi_{dijet}$ bins, while the resolution in rapidity can move jets in and out of the central rapidity region ($|\eta| < 1.1$).

7.5.1   Jet Energy Resolution Effects

Electronic noise, sampling fluctuations, and miss-calibrations of the CMS detector contribute to the jet energy resolution. To evaluate these effects, the momenta and energies of generated jets are smeared according to the measured p_T-resolutions. In the smearing process, Gaussian distributions are used to quantify the core of the jet p_T resolution distributions. The effects introduced by the non-Gaussian tails are small and are covered by the systematic uncertainties associated with the smearing process. The smeared generated jets are reordered in p_T and new values of the dijet azimuthal
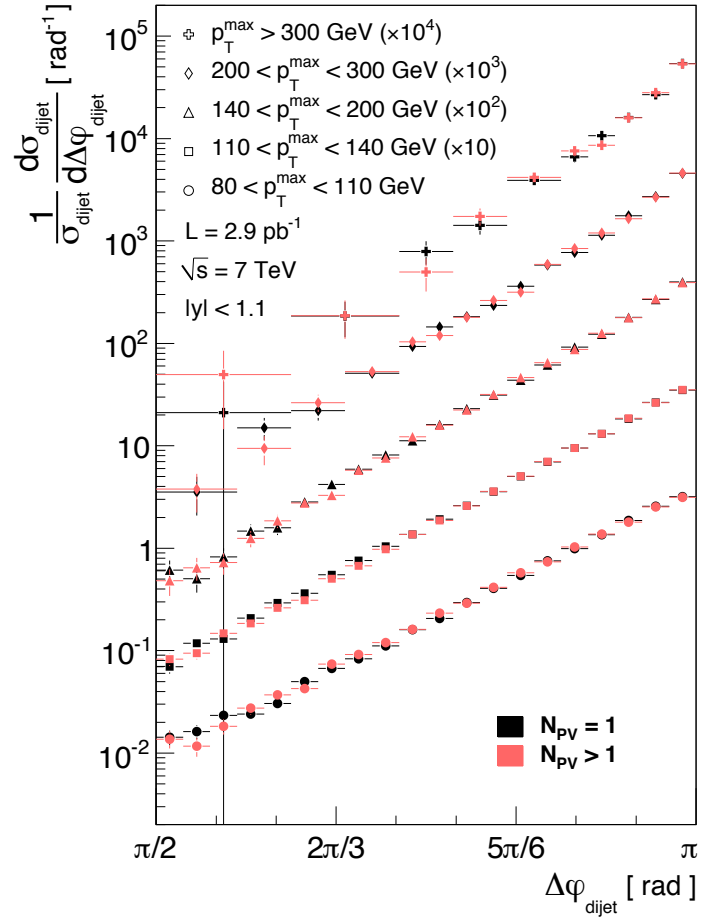
Figure 42. Dijet azimuthal decorrelations from data for events with only one good primary vertex ($N_{PV} = 1$) and events with multiple good primary vertices ($N_{PV} > 1$), for several $p_{T,max}$ regions.
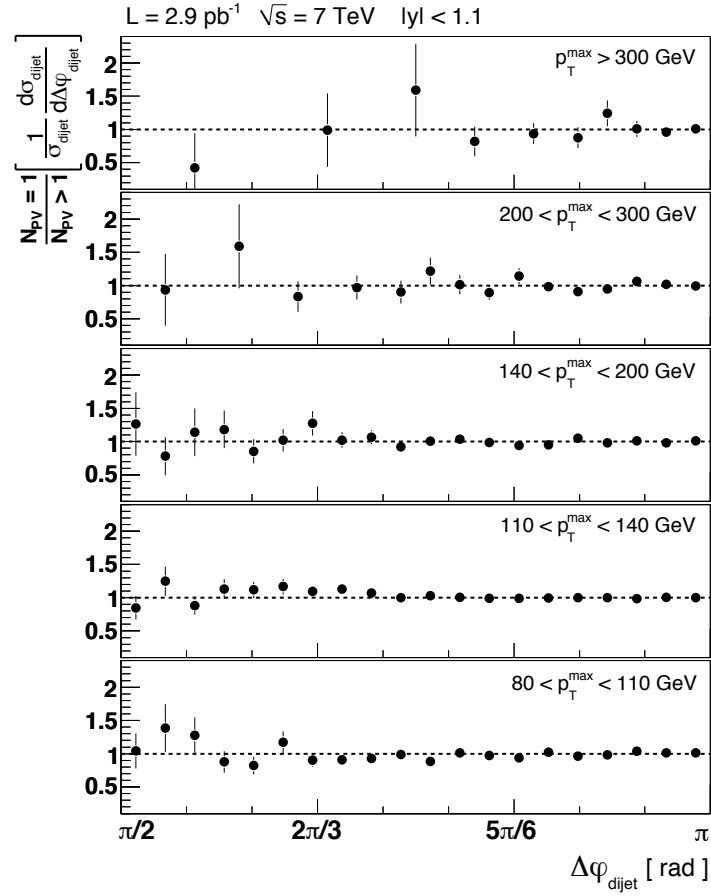
Figure 43. Pile-up effects on the dijet azimuthal decorrelations for several $p_{T,max}$ regions. $N_{PV} = 1$ represents events with only one good primary vertex, while $N_{PV} > 1$ events with multiple good primary vertices.

decorrelations are calculated. The same kinematic jet selection criteria are applied to the smeared and generated jets.

The jet energy resolution effects on the dijet azimuthal decorrelations are determined from the ratio of the $\Delta\varphi_{dijet}$ distributions using generated jets to the distributions using generated jets smeared by the detector p_T-resolution. This is shown in Figure 44 for two independent MC samples, PYTHIA6 D6T and HERWIG++, for all $p_{T,max}$ regions. For $\Delta\varphi_{dijet} > 2\pi/3$ the effects are relatively small, while below this value the effects are as high as 20%.

7.5.2   Jet Position Resolution Effects

The PF jet position resolution is mainly driven by the finite size of the tracker silicon strips and the calorimeter clusters. To evaluate the effects of the jet position resolutions on the $\Delta\varphi_{dijet}$ distributions, the φ and η positions of generated jets are smeared according to the measured resolutions. The effects are extracted from ratios between the nominal generated $\Delta\varphi_{dijet}$ distributions and the smeared ones.

The effects of the jet φ and η position resolution on the $\Delta\varphi_{dijet}$ distributions are shown in Figure 45 and Figure 46. The dijet azimuthal decorrelations are found to be almost insensitive to the jet position resolution in both φ and η for all $p_{T,max}$ regions.

7.6   Unfolding Corrections

The measured $\Delta\varphi_{dijet}$ distributions have to be corrected back to the particle level before comparing them to various MC event generators. The correction factors are de-
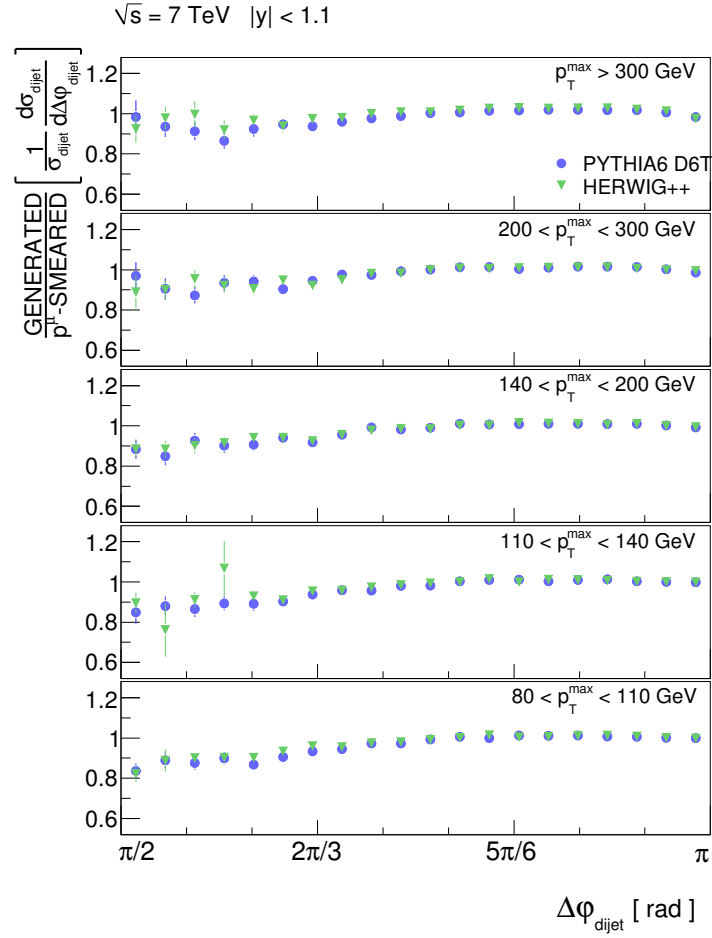
Figure 44. Ratios of dijet azimuthal decorrelations from generated jets and generated jets with smeared momenta and energies in PYTHIA6 D6T and HERWIG++, for several $p_{T,max}$ regions.
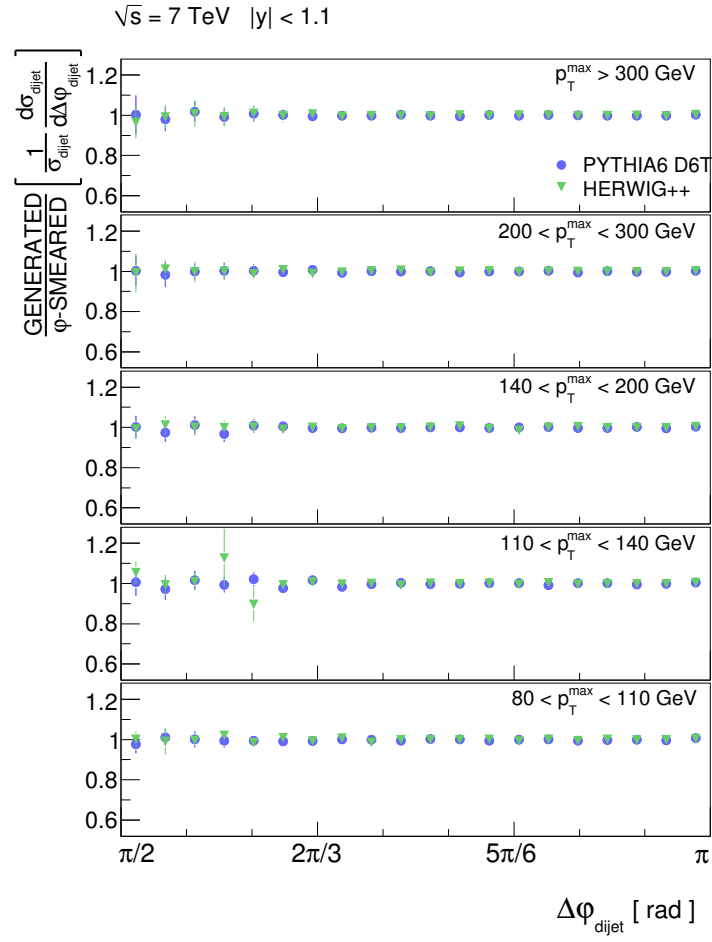
Figure 45. Ratios of dijet azimuthal decorrelations from generated jets and generated jets with smeared positions in φ in PYTHIA6 D6T and HERWIG++, for several $p_{T,max}$ regions.
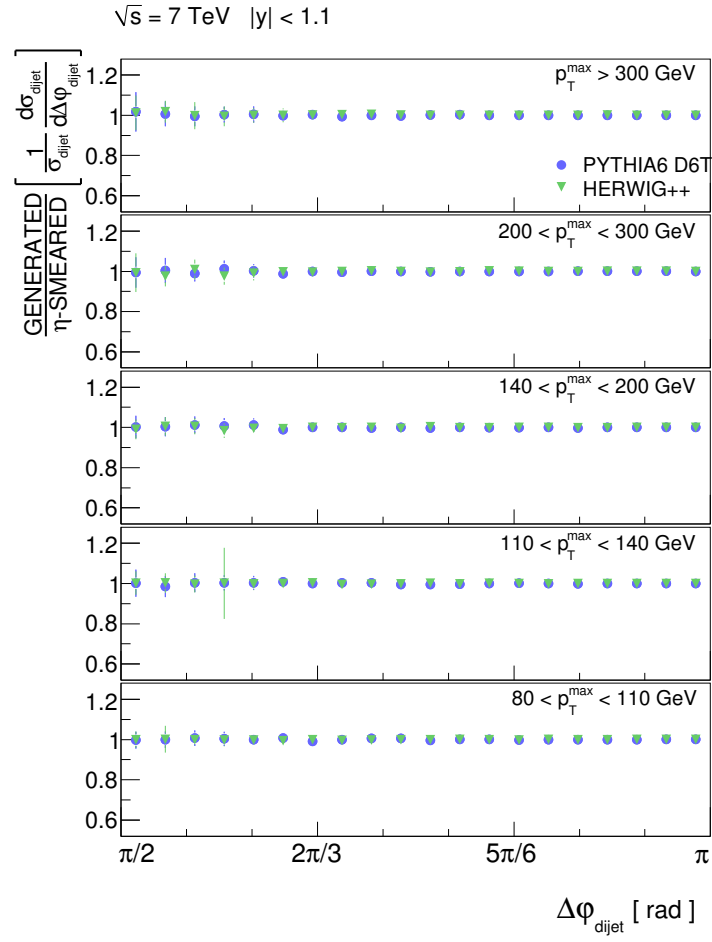
Figure 46. Ratios of dijet azimuthal decorrelations from generated jets and generated jets with smeared positions in η in PYTHIA6 D6T and HERWIG++, for several $p_{T,max}$ regions.

termined using two independent MC samples, PYTHIA6 D6T and HERWIG++. The momenta, energies, and positions in $\eta - \varphi$ of generated jets are smeared according to the measured p_T and position resolutions. The ratio between the $\Delta\varphi_{dijet}$ distributions of the generated and smeared jets determines the unfolding correction factors for each $p_{T,max}$ region, for a given MC sample.

The average of the correction factors for each $p_{T,max}$ region from the two MC samples are used as the final unfolding corrections applied to data (Figure 47). The unfolding correction factors modify the measured $\Delta\varphi_{dijet}$ distributions by less than 2% for $5\pi/6 < \Delta\varphi_{dijet} < \pi$. For $\Delta\varphi_{dijet} \sim \pi/2$, the changes range from 11% for the highest $p_{T,max}$ region to 19% for the lowest.

The unfolding correction factors are applied to the $\Delta\varphi_{dijet}$ distributions from smeared generated jets ,which are then compared to the nominal generated $\Delta\varphi_{dijet}$ distributions. Figure 48 shows these comparisons in both PYTHIA6 D6T and HERWIG++ for all $p_{T,max}$ regions. The ratios show a good closure over the entire $\Delta\varphi_{dijet}$ range.

To validate the use of Gaussian-smearing to generated jets for determining the unfolding correction factors, a comparison between the $\Delta\varphi_{dijet}$ distributions from reconstructed jets (using full detector simulation) and smeared generated jets in PYTHIA6 D6T is performed for each $p_{T,max}$ region. These are shown in Figure 49. The deviations from unity are taken as an additional systematic uncertainty.
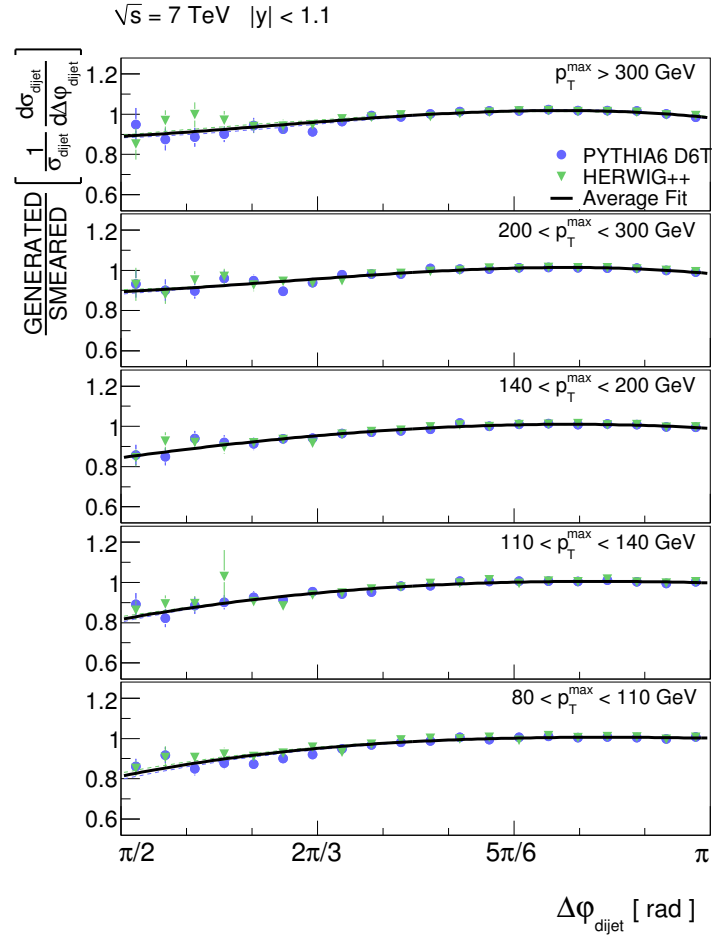
Figure 47. Ratios of dijet azimuthal decorrelations from generated jets and generated jets with smeared momenta and positions in $\eta - \varphi$ in PYTHIA6 D6T and HERWIG++, for several $p_{T,max}$ regions.
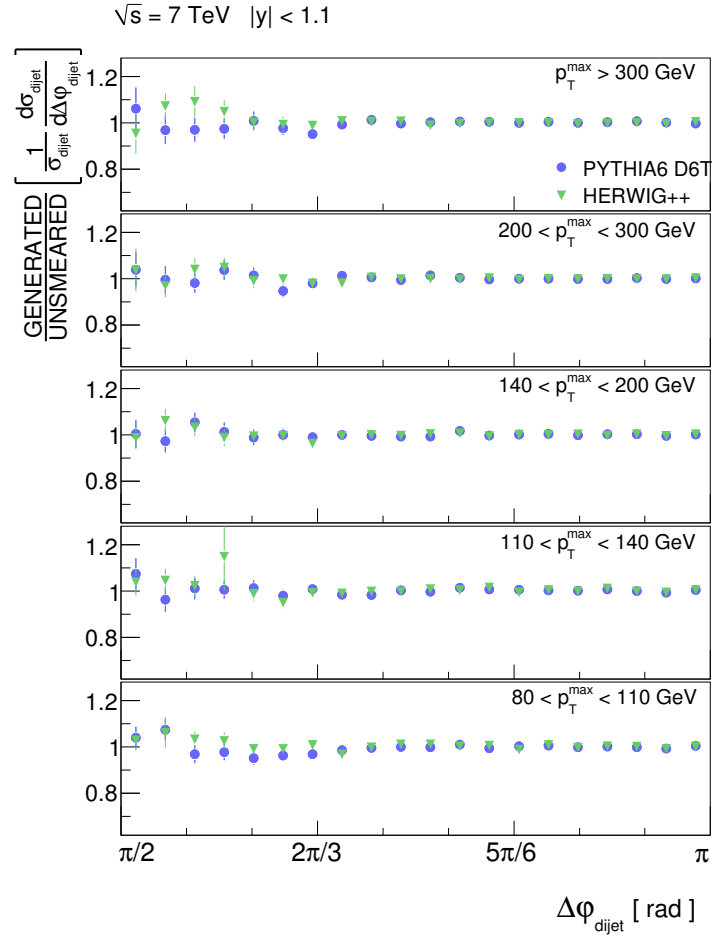
Figure 48. Ratios between nominal generated $\Delta\varphi_{dijet}$ distributions and unfolded $\Delta\varphi_{dijet}$ distributions from generated jets with smeared momenta and positions in $\eta - \varphi$ in PYTHIA6 D6T and HERWIG++, for several $p_{T,max}$ regions.
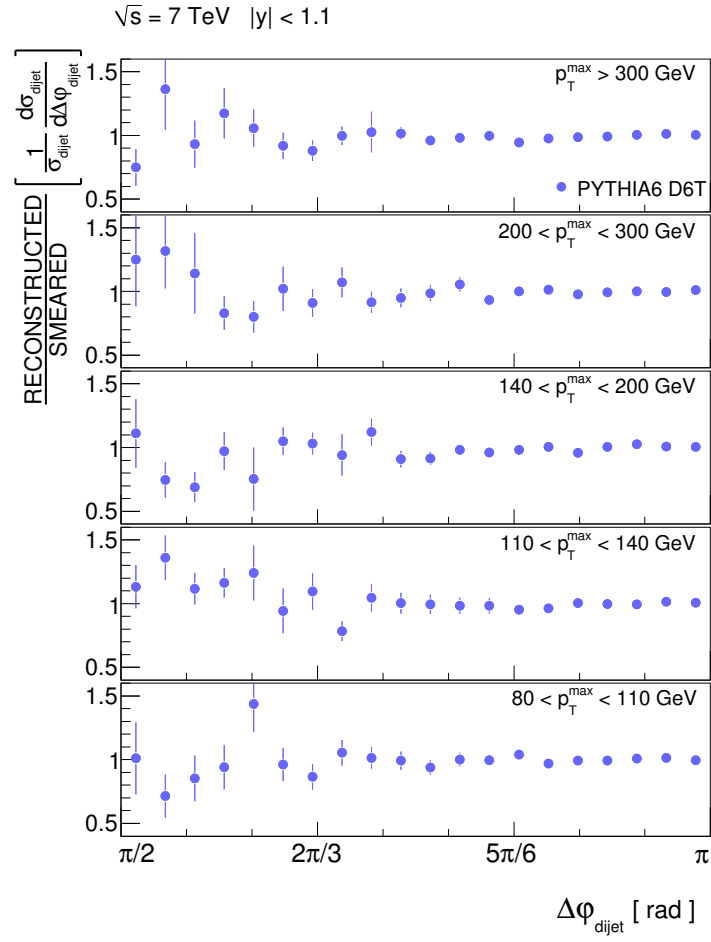
Figure 49. Ratios of dijet azimuthal decorrelations from reconstructed jets and generated jets with smeared momenta and positions in $\eta - \varphi$ in PYTHIA6 D6T, for several $p_{T,max}$ regions.

The validity of the bin-by-bin unfolding correction factors is tested by calculating the deviations between the $\Delta\varphi_{dijet}$ distributions for uncorrected data and smeared PYTHIA6 D6T, and for unfolded data and generated distributions. These comparisons are shown in Figure 50 and Figure 51. χ^2 values are calculated for each $p_{T,max}$ region and found to be similar for the two cases, suggesting that the bin-by-bin correction factors do not alter the conclusions of the analysis.

7.7   Systematic Uncertainties

The main sources of systematic uncertainty for this measurement arise from uncertainties in the jet energy calibration, the jet p_T resolution, and the unfolding correction. The jet energy calibration uncertainties are propagated as variations in the jet energy as a function of jet p_T and η, while uncertainties in the jet p_T resolution are propagated through the smearing process of generated jets. The uncertainties of the unfolding corrections are quantified by looking at different MC samples.

7.7.1   Jet Energy Scale Uncertainties

The jet energy calibration uncertainties are calculated as a function of the jet p_T and η with typical values, in the considered phase space, between 2.5% and 3.5%. The effects of these uncertainties on the $\Delta\varphi_{dijet}$ are extracted from the ratios between the $\Delta\varphi_{dijet}$ distributions of the standard smeared generated jets and new ones with momenta and energies modified according to the measured jet energy calibration uncertainties.
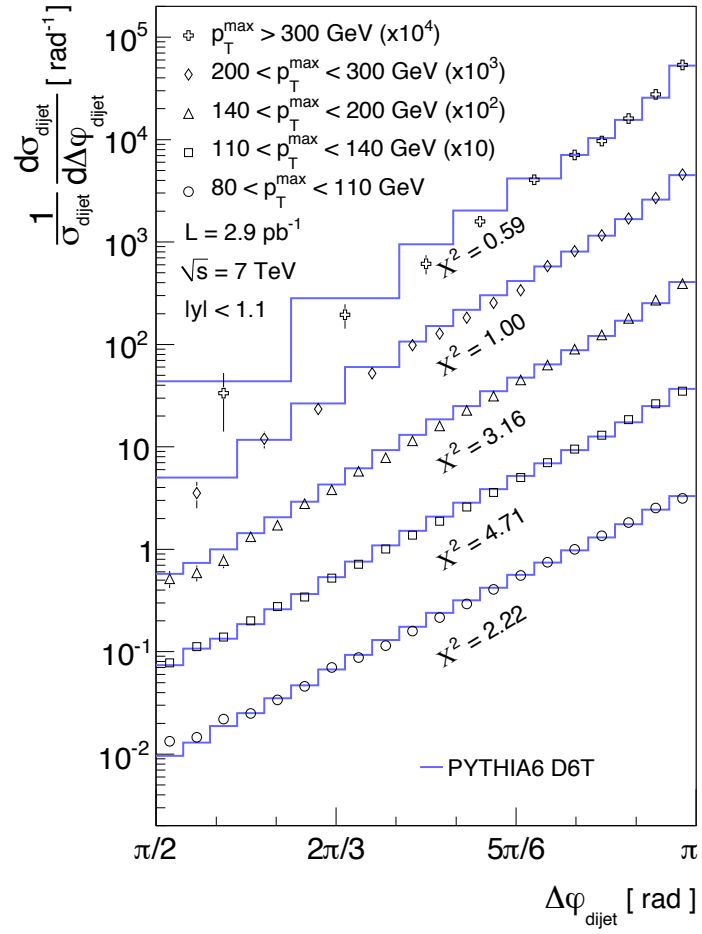
Figure 50. Deviations in the dijet azimuthal decorrelations between data and smeared generated jets from PYTHIA6 D6T, for several $p_{T,max}$ regions.
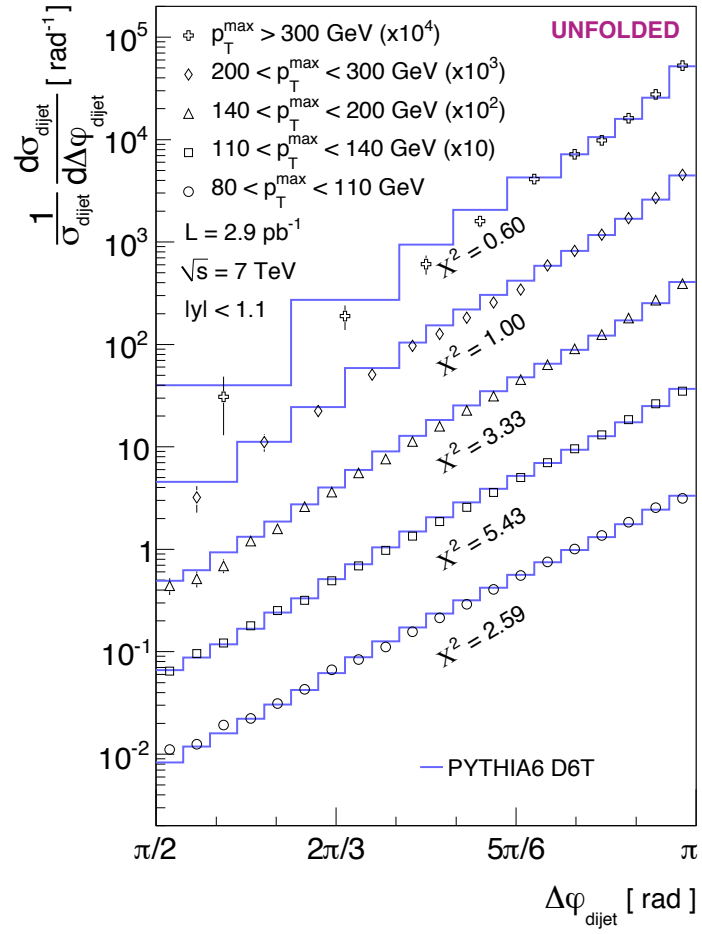
Figure 51. Deviations in the dijet azimuthal decorrelations between unfolded data and generated jets from PYTHIA6 D6T, for several $p_{T,max}$ regions.

For each $\Delta\varphi_{dijet}$ bin, and for each MC sample, the deviations from unity, due to the varied jet energies, are sorted and the maximum and minimum deviations are constructed. The deviations from PYTHIA6 D6T and HERWIG++ are combined using a weighted average procedure. The weighted average $(\widehat{\Delta\varphi_i})$ and the standard deviation $(\sigma_{\Delta\varphi_i})$ for each $\Delta\varphi_{dijet}$ bin are calculated as:

$$\widehat{\Delta\varphi_i} = \frac{1}{\omega_i} \sum_{j=1}^{2} \frac{\Delta\varphi_{ij}}{\sigma_{ij}^2} \tag{7.1}$$

$$\sigma_{\Delta\varphi_i} = \frac{1}{\sqrt{\omega_i}} \tag{7.2}$$

$$\omega_i = \sum_{j=1}^{2} \frac{1}{\sigma_{ij}^2} \tag{7.3}$$

where $\Delta\varphi_{ij}$ represents the bin content for each MC generator and σ_{ij} the bin error.

The resulting uncertainties on the dijet azimuthal decorrelations range from 5% at $\Delta\varphi_{dijet} \sim \pi/2$ to 1% at $\Delta\varphi_{dijet} \sim \pi$. These are illustrated in Figure 52 for all $p_{T,max}$ regions.

7.7.2 Jet Energy Resolution Uncertainties

The effects of the jet energy resolution uncertainties on the dijet azimuthal decorrelations are estimated by varying the jet p_T resolutions by $\pm 10\%$ and comparing the $\Delta\varphi_{dijet}$ distributions before and after the change.

The effects from PYTHIA6 D6T and HERWIG++ are combined using the weighted average procedure described in the previous section. This yields a variation on the $\Delta\varphi_{\text{dijet}}$
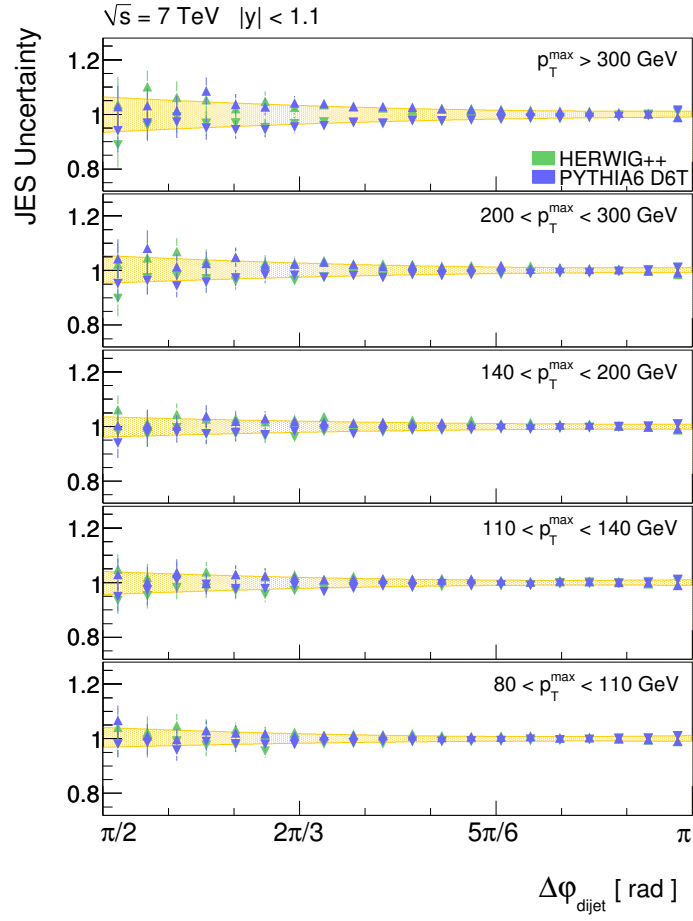
Figure 52. Effects of the jet energy scale uncertainties on the dijet azimuthal decorrelations in both PYTHIA6 D6T and HERWIG++ for several $p_{T,max}$ regions.

distributions ranging from 5% at $\Delta\varphi_{dijet} \sim \pi/2$ to 1% at $\Delta\varphi_{dijet} \sim \pi$, which is shown in Figure 53 for all $p_{T,max}$ regions.

7.7.3   Unfolding Uncertainties

The uncertainties on the unfolding correction factors are estimated by comparing the corrections from PYTHIA6 D6T with large variations of ISR. Appendix D includes comparisons between jet kinematic distributions for data and PYTHIA6 D6T simulations with different ISR conditions. As shown by these comparisons, the data distributions lie within the PYTHIA6 D6T simulations with the two extreme ISR conditions, for all jet kinematic distributions tested. These two extreme PYTHIA6 D6T simulations are used to estimate the systematic uncertainties of the unfolding correction factors related to the physics modeling. The unfolding correction factors from MADGRAPH, PYTHIA8, and PYTHIA6 Z2 also lie between these two extreme PYTHIA6 D6T simulations. The unfolding uncertainties vary from 8% at $\Delta\varphi_{dijet} \sim \pi/2$ to 1.5% at $\Delta\varphi_{dijet} \sim \pi$ (Figure 54).

The systematic uncertainty from using a parametrized model to simulate the finite jet p_T and position resolutions of the detector is estimated by the RMS of the ratio between the $\Delta\varphi_{dijet}$ distributions of the reconstructed and smeared generated jets in PYTHIA6 D6T, which includes the full GEANT simulation of the CMS detector. These small discrepancies could be due to non-Gaussian resolution tails or additional detector effects not considered in the smearing process. The uncertainty is estimated to be about 2.5% in all $p_{T,max}$ regions (Figure 55).
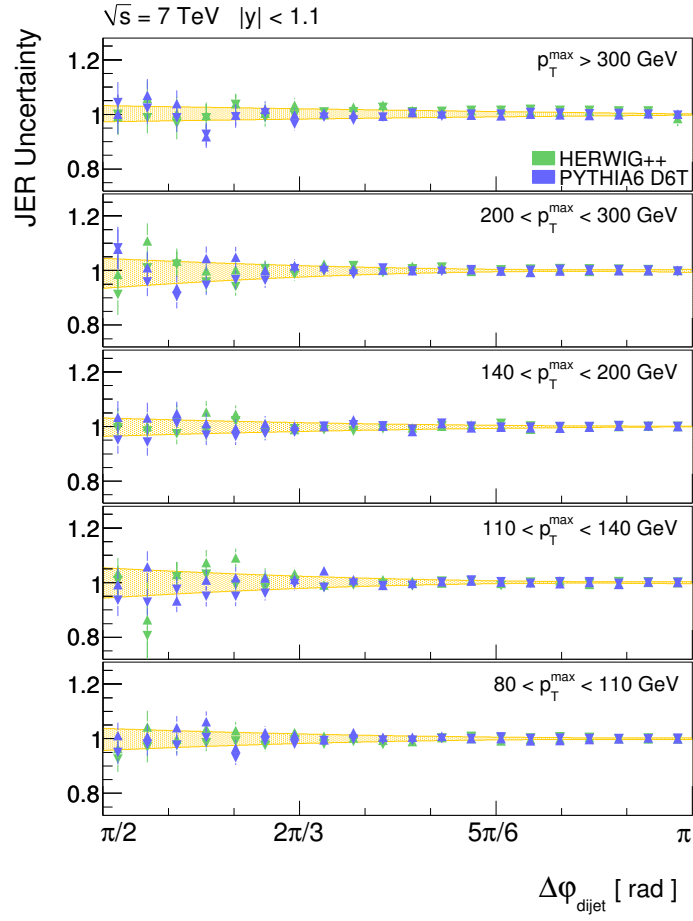
Figure 53. Effects of the jet energy resolution uncertainties on the dijet azimuthal decorrelations in both PYTHIA6 D6T and HERWIG++ for several $p_{T,max}$ regions.
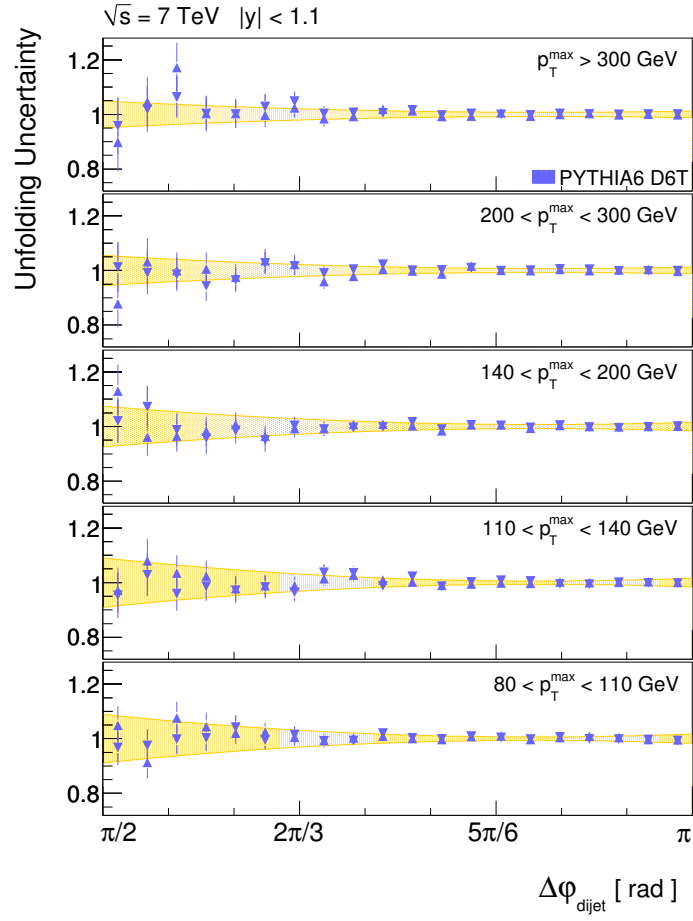
Figure 54. Unfolding correction uncertainties as calculated from PYTHIA6 D6T with different ISR values for several $p_{T,max}$ regions.
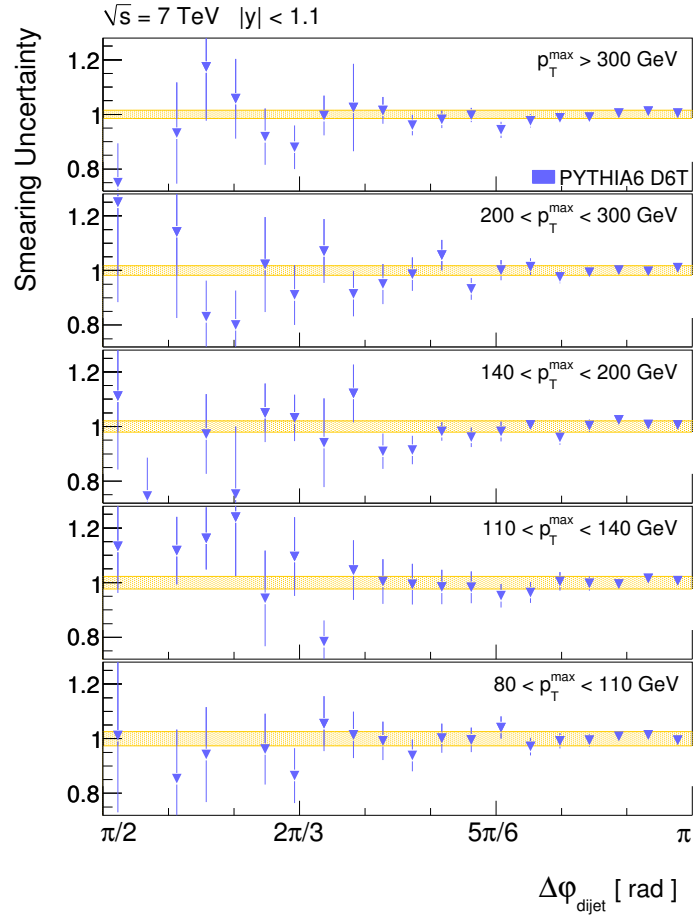
Figure 55. Systematic uncertainties introduced by the smearing process of generated jets in PYTHIA6 D6T for several $p_{T,max}$ regions.

7.8 Non-Perturbative Corrections and Uncertainties

The pQCD predictions do not account for UE, MPI, and hadronization effects. When compared to the unfolded data, these effects need to be added to the pQCD calculations.

The non-perturbative correction factors are determined using two independent MC generators, PYTHIA6 D6T and HERWIG++, with UE, MPI, and hadronization turned on and off. In PYTHIA6, this is achieved by setting "MSTP(81) = 0" to turn off UE and MPI, and "MSTJ(1) = 0" to turn off hadronization. In HERWIG++, UE and MPI are turned off by "set /Herwig/Shower/ShowerHandler:MPIHandler NULL" while hadronization is turned off by "set /Herwig/EventHandlers/LHCHandler:HadronizationHandler NULL".

The average of the ratios between the dijet azimuthal decorrelations from the two MC samples with UE, MPI, and hadronization turned on and off provide the correction factors which amount to 13% at $\Delta\varphi_{dijet} \sim \pi/2$ and 4% at $\Delta\varphi_{dijet} \sim \pi$ (Figure 56).

The systematic uncertainties associated with the non-perturbative corrections are estimated from the difference between the individual corrections derived from PYTHIA6 D6T and HERWIG++ and the average correction. The systematic uncertainties are found to be 6% at $\Delta\varphi_{dijet} \sim \pi/2$ and 2% at $\Delta\varphi_{dijet} \sim \pi$. These are shown in Figure 57 for all $p_{T,max}$ regions.
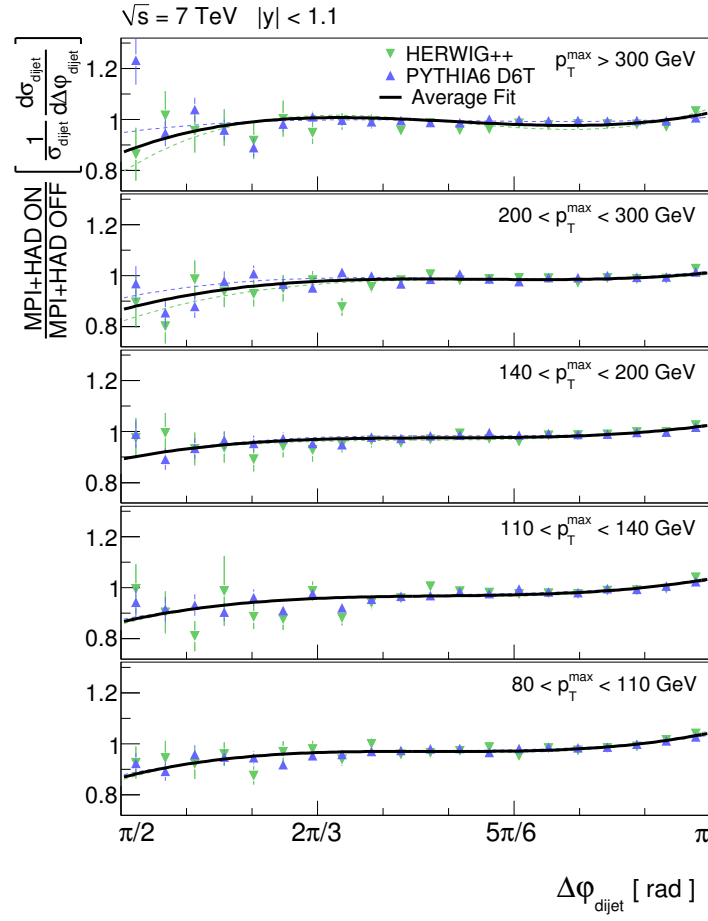
Figure 56. Non-perturbative correction factors as determined from PYTHIA6 D6T and HERWIG++ for several $p_{T,max}$ regions.
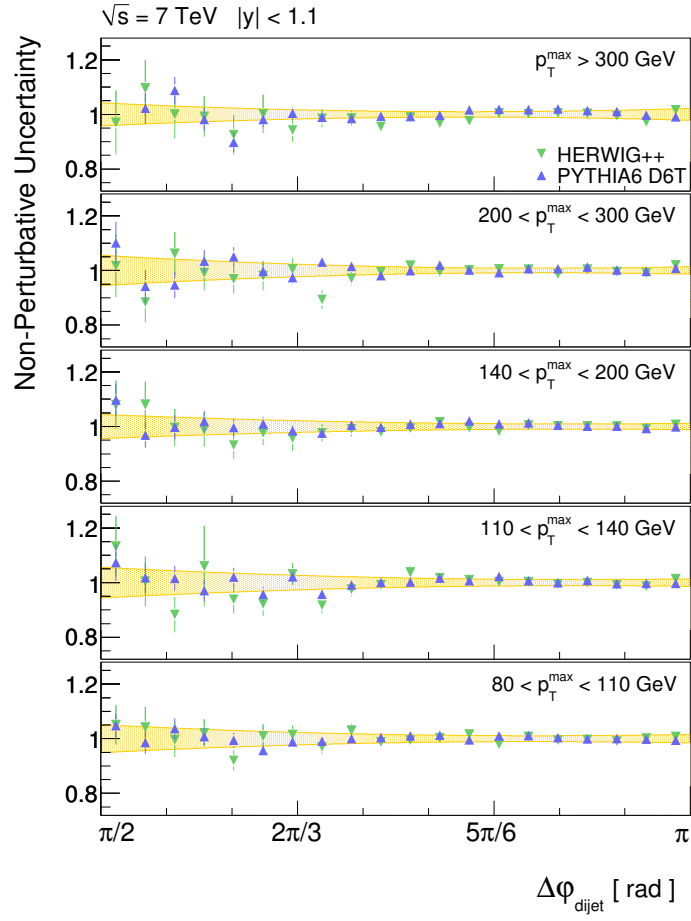
Figure 57. Systematic uncertainties associated with the non-perturbative correction factors for several $p_{T,max}$ regions.

CHAPTER 8

RESULTS AND CONCLUSIONS

8.1   Results

The unfolded differential $\Delta\varphi_{dijet}$ distributions, normalized to the integrated dijet cross-section, in each $p_{T,max}$ region, are shown in Figure 58. The distributions are scaled by multiplicative factors for presentation purposes. The error bars on the data points represent the statistical and systematic uncertainties added in quadrature. The total systematic uncertainties vary from 11% at $\Delta\varphi_{dijet} \sim \pi/2$ to 3% at $\Delta\varphi_{dijet} \sim \pi$. Each data point is plotted at the abscissa value for which the predicted differential $\Delta\varphi_{dijet}$ distribution has the same value as the bin average obtained using PYTHIA6 D6T, which provides a good description of the data (60). A detailed list of all data points[1] and their associated uncertainties, for all $p_{T,max}$ regions, is presented in Appendix E.

The $\Delta\varphi_{dijet}$ distributions from PYTHIA6 D6T, PYTHIA6 Z2, PYTHIA8, HER-WIG++, and MADGRAPH event generators are also presented for comparison. The PYTHIA6 (D6T and Z2), PYTHIA8, and MADGRAPH event generators use the CTEQ6L (61) PDFs, while HERWIG++ uses the MRST2001 (62) PDFs. The MADGRAPH event gen-

---

[1] All data points are available also online in the Durham HepData Reaction Database (http://hepdata.cedar.ac.uk/view/p7938)

137

erator uses PYTHIA6 for parton showering and hadronization, and the MLM method (63) to map the parton-level event into a parton shower history.

Figure 59 shows ratios of the measured $\Delta\varphi_{dijet}$ distributions to MC predictions for all $p_{T,max}$ regions. The total systematic uncertainties are shown by the shaded bands.

The predictions from PYTHIA6 and HERWIG++ describe the shape of the data distributions well, while MADGRAPH (PYTHIA8) predicts less (more) azimuthal decorrelation than what is observed in data.

Figure 60 shows comparisons between the measured $\Delta\varphi_{dijet}$ distributions and LO and NLO pQCD calculations from the parton-level generator NLOJET++ (7) within the FASTNLO framework (8). The predictions near $\Delta\varphi_{dijet} = \pi$ are excluded because of their sensitivity to higher-order corrections which are not included in the present calculations. The PDFs are from CTEQ6.6 (61), while the renormalization and factorization scales are chosen to be $\mu_r = \mu_f = p_{T,max}$. The LO curves represent processes with three partons in the final state, normalized to the LO $\sigma_{dijet}(2 \to 2)$ cross section, with non-zero contributions from $2\pi/3$ to π, while NLO predictions include $2 \to 3$ processes at NLO, normalized to σ_{dijet} at NLO.

$$\frac{1}{\sigma_{dijet}}\bigg|_{(N)LO} \times \frac{d\sigma_{dijet}}{d\Delta\varphi_{dijet}}\bigg|_{(N)LO} \tag{8.1}$$

Ratios between the measured $\Delta\varphi_{dijet}$ distributions and NLO pQCD predictions are also shown in Figure 61. The error bars on the data points include statistical and
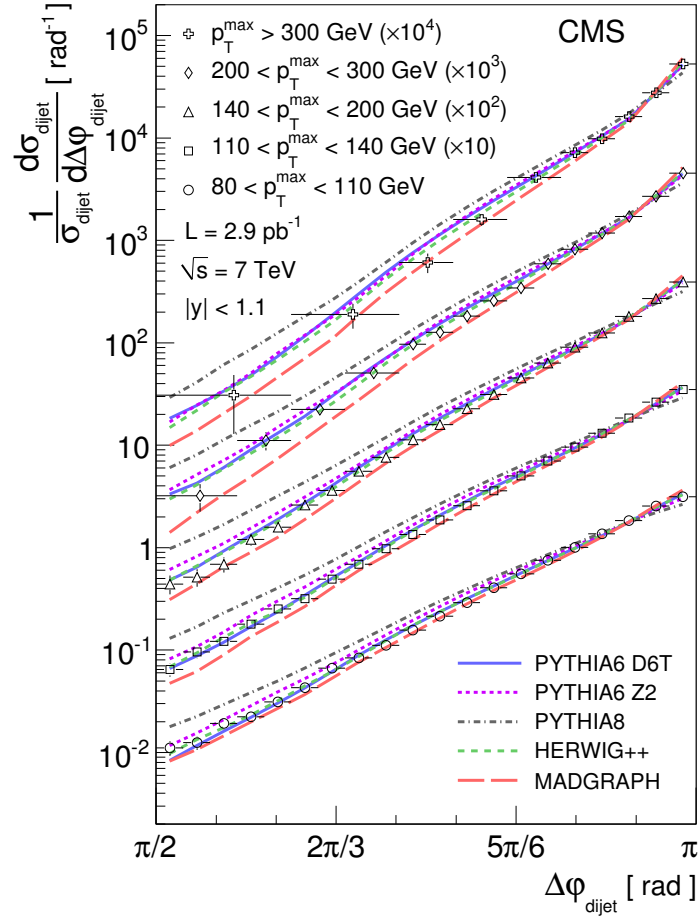
Figure 58. Normalized $\Delta\varphi_{dijet}$ distributions in several $p_{T,max}$ regions scaled by multiplicative factors for easier presentation. The curves represent predictions from PYTHIA6, PYTHIA8, HERWIG++ and MADGRAPH. The error bars on the data points include statistical and systematic uncertainties.
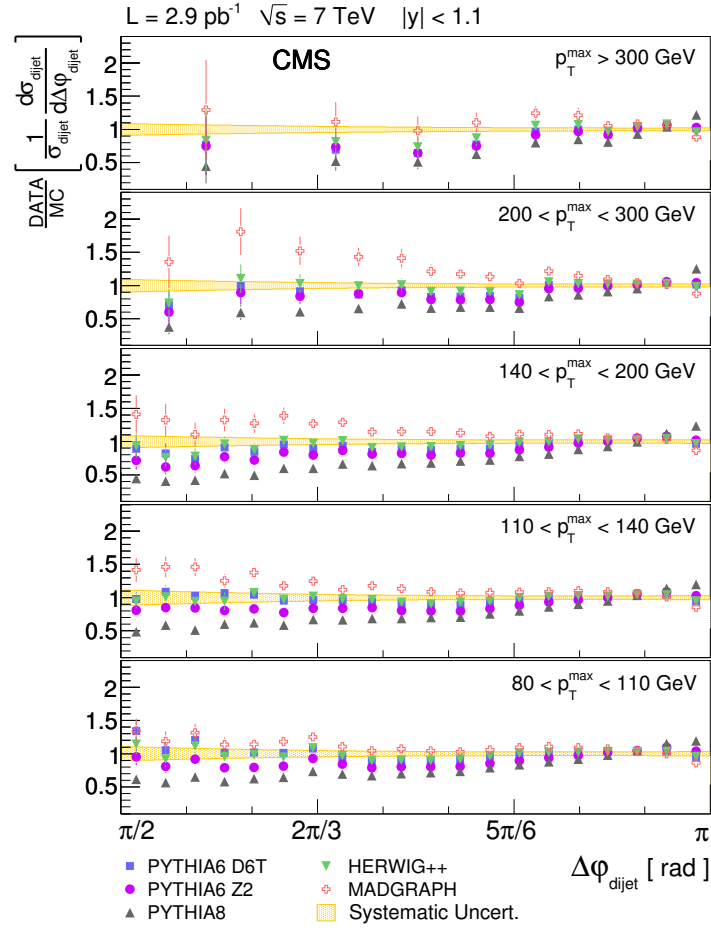
Figure 59. Ratios of measured normalized $\Delta\varphi_{dijet}$ distributions to PYTHIA6, PYTHIA8, HERWIG++ and MADGRAPH predictions in several $p_{T,max}$ regions. The shaded bands indicate the total systematic uncertainty.

systematic uncertainties. The effects on the NLO pQCD predictions due to μ_r and μ_f scale variations and PDF uncertainties, as well as uncertainties from the non-perturbative corrections are shown.

Uncertainties due to the renormalization and factorization scales are evaluated by varying the default choice of $\mu_r = \mu_f = p_{T,max}$ between $p_{T,max}/2$ and $2 \cdot p_{T,max}$ in the following six combinations:

$$\mu_r = p_{T,max}/2 \text{ and } \mu_f = p_{T,max}/2 \tag{8.2}$$

$$\mu_r = 2 \cdot p_{T,max} \text{ and } \mu_f = 2 \cdot p_{T,max} \tag{8.3}$$

$$\mu_r = p_{T,max} \text{ and } \mu_f = p_{T,max}/2 \tag{8.4}$$

$$\mu_r = p_{T,max} \text{ and } \mu_f = 2 \cdot p_{T,max} \tag{8.5}$$

$$\mu_r = p_{T,max}/2 \text{ and } \mu_f = p_{T,max} \tag{8.6}$$

$$\mu_r = 2 \cdot p_{T,max} \text{ and } \mu_f = p_{T,max} \tag{8.7}$$

The largest variation is used to calculate the systematic uncertainties associated with the renormalization and factorization scales. These scale variations modify the predictions of the normalized $\Delta\varphi_{dijet}$ distributions by less than 50%.

The PDF uncertainties are derived using the 22 CTEQ6.6 uncertainty eigenvectors and are found to be 9% at $\Delta\varphi_{dijet} \sim \pi/2$ and 2% for $\Delta\varphi_{dijet} < \pi$. Following the proposal
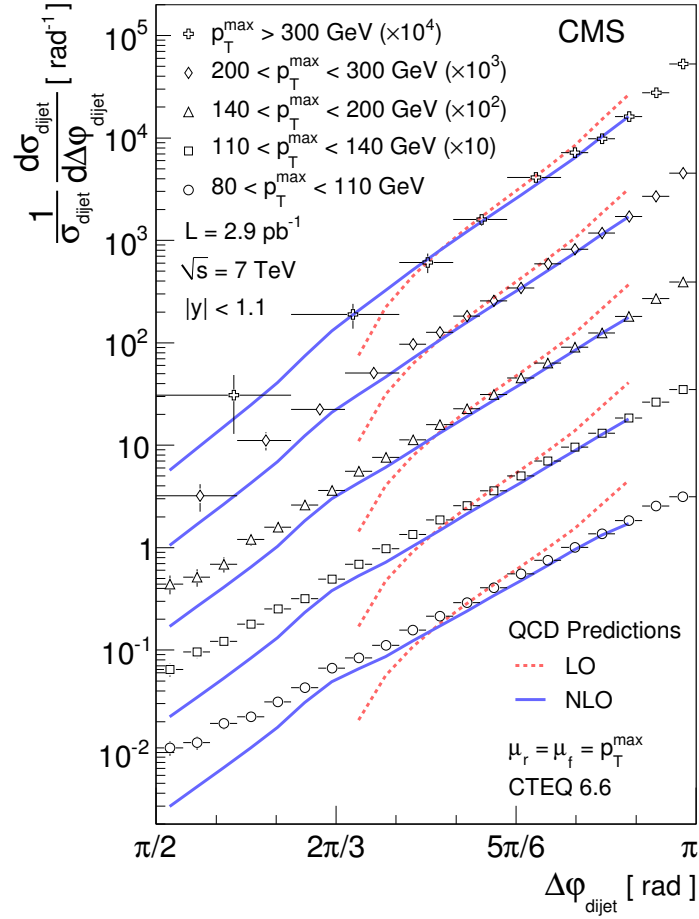
Figure 60. Normalized $\Delta\varphi_{dijet}$ distributions in several $p_{T,max}$ regions scaled by multiplicative factors for easier presentation. The curves represent predictions from LO and NLO pQCD. Non-perturbative corrections have been applied to the predictions. The error bars on the data points include statistical and systematic uncertainties.
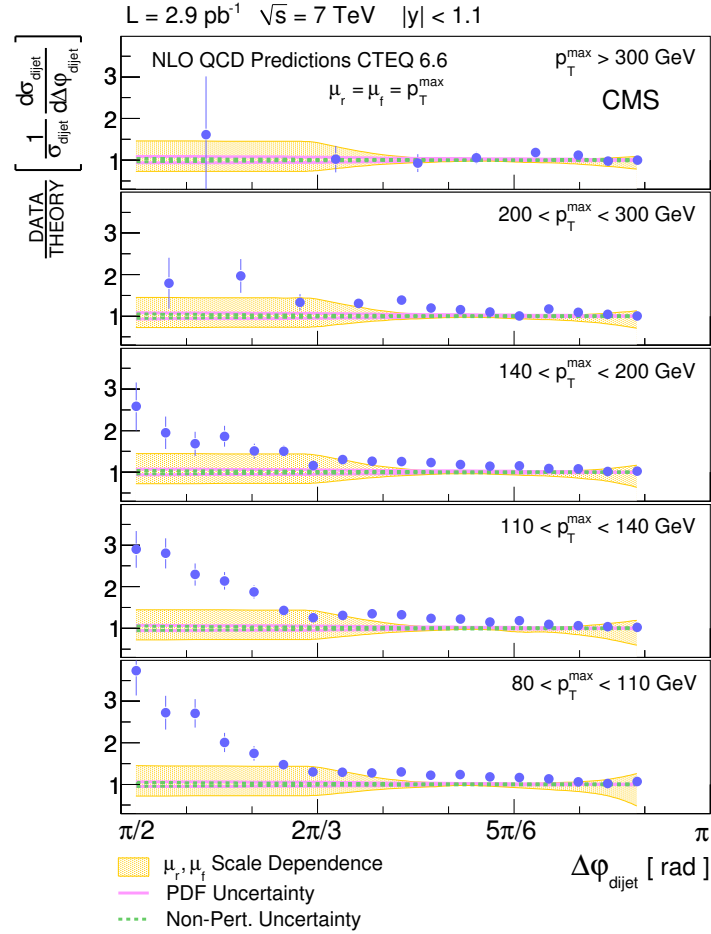
Figure 61. Ratios of measured normalized $\Delta\varphi_{dijet}$ distributions to NLO pQCD predictions with the non-perturbative corrections applied, for several $p_{T,max}$ regions. The error bars on the data points include statistical and systematic uncertainties. The effects on the NLO pQCD predictions due to μ_r and μ_f scale variations and PDF uncertainties, as well as uncertainties from the non-perturbative corrections are shown.

of the PDF4LHC working group (64), the impact of other global PDF fits are found to be negligible in the context of this analysis.

The NLO predictions provide a good description of the shape of the data distributions over much of the $\Delta\varphi_{dijet}$ range. Compared to data, the reduced decorrelation in the theoretical prediction and the increased sensitivity to the μ_r and μ_f scale variations for $\Delta\varphi_{dijet} < 2\pi/3$ are attributed to the fact that the pQCD predictions in this region are effectively available only at leading order, since the contribution from tree-level four-parton final states dominates.

8.2 Sensitivity to ISR and FSR in PYTHIA6

The sensitivity of the $\Delta\varphi_{dijet}$ distributions to ISR and FSR is investigated by varying the input parameters $k_{ISR} \equiv PARP(67)$ and $k_{FSR} \equiv PARP(71)$ in PYTHIA6. The product of k_{ISR} (k_{FSR}) and the square of the hard-scattering scale gives the maximum allowed parton virtuality in the initial (final) state shower. Previous studies have shown that k_{ISR} and k_{FSR} are the only parameters in PYTHIA6 with a visible impact on the $\Delta\varphi_{dijet}$ distributions (65). The default values of $k_{ISR} = 2.5$ and $k_{FSR} = 4.0$ in PYTHIA6 D6T were determined from the DØ dijet azimuthal decorrelation results (9).

Figure 62 shows comparisons of the measured $\Delta\varphi_{dijet}$ distributions to PYTHIA6 distributions with different k_{ISR} values. The effects are more pronounced for smaller $\Delta\varphi_{dijet}$ angles where multi-gluon radiation dominates. Ratios of measured $\Delta\varphi_{dijet}$ distributions to PYTHIA6 with different values of k_{ISR} are shown in Figure 63.

Similar comparisons are shown in Figure 64 and Figure 65 for $\Delta\varphi_{dijet}$ distributions from data and PYTHIA6 with different k_{FSR} values.

By varying k_{ISR} by ± 0.5 from its default value a change of about 30% is observed in the PYTHIA6 prediction for $\Delta\varphi_{dijet} \sim \pi/2$ (Figure 66). A much wider variation of k_{FSR} from 2.5 to 8.0 (4.0 being its default value) generates less than 10% changes in the $\Delta\varphi_{dijet}$ distributions, in all $p_{T,max}$ regions (Figure 67). This suggests that the dijet azimuthal decorrelations could be used to further tune parameters in the MC event generators that control radiative effects in the initial state.

8.3 Conclusions

Dijet azimuthal decorrelations in several $p_{T.max}$ regions are measured from proton-proton collisions at $\sqrt{s} = 7$ TeV. The PYTHIA6 and HERWIG++ event generators are found to best describe the shape of the measured distributions over the entire $\Delta\varphi_{dijet}$ range. The MADGRAPH event generator predicts less azimuthal decorrelation than what is observed in data while PYTHIA8 predicts more. The predictions from NLO pQCD are in reasonable agreement with the measured distributions, except at small $\Delta\varphi_{dijet}$ values where multi-parton radiation effects dominate. The $\Delta\varphi_{dijet}$ distributions are found to be sensitive to initial-state gluon radiation. The analysis is published in the Physical Review Letters (11).
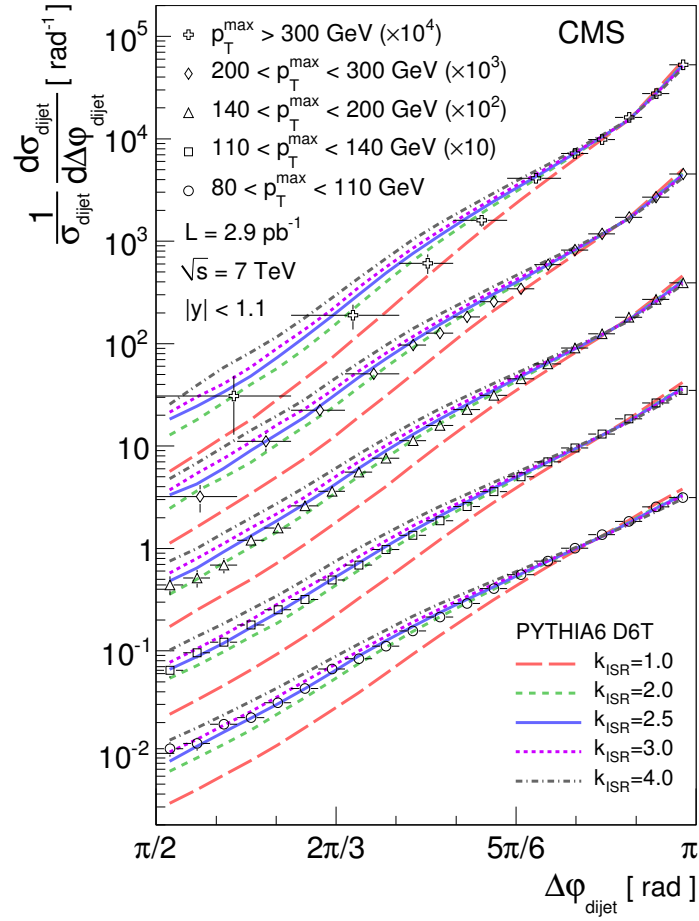
Figure 62. Normalized $\Delta\varphi_{dijet}$ distributions in several $p_{T,max}$ regions scaled by multiplicative factors for easier presentation. The curves represent predictions from PYTHIA6 with different values of k_{ISR}. The error bars on the data points include statistical and systematic uncertainties.
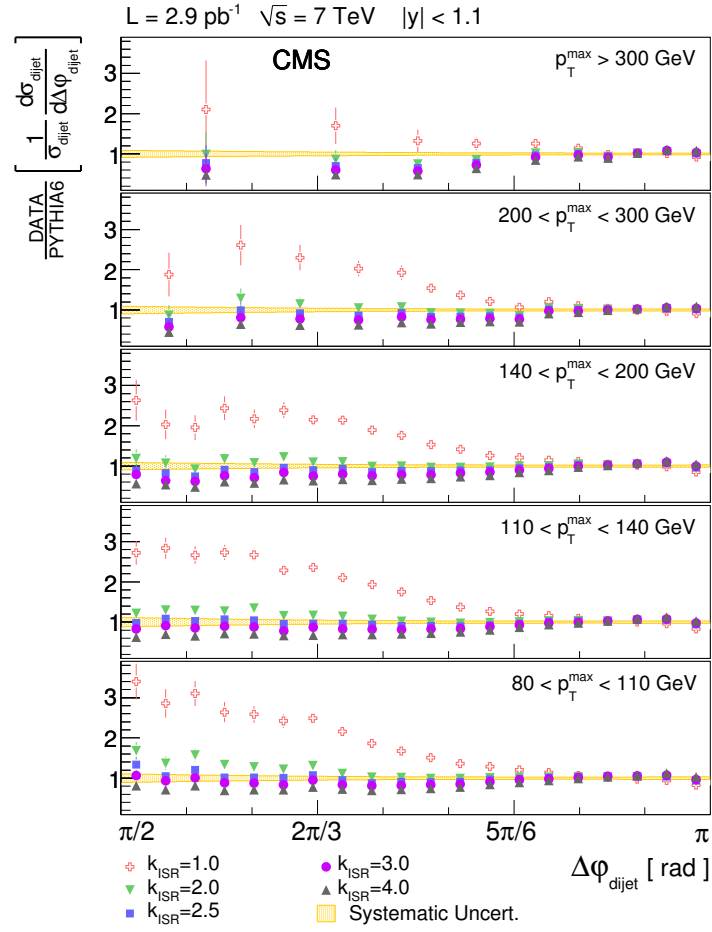
Figure 63. Ratios of measured normalized $\Delta\varphi_{dijet}$ distributions to PYTHIA6 with different values of k_{ISR} in several $p_{T,max}$ regions. The shaded bands indicate the total systematic uncertainties.
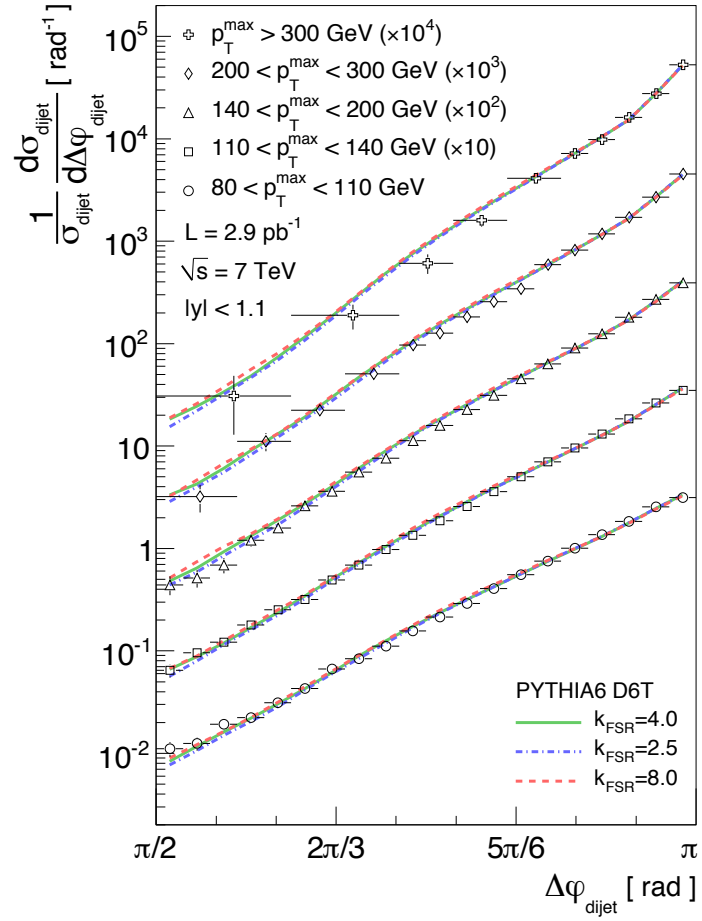
Figure 64. Normalized $\Delta\varphi_{dijet}$ distributions in several $p_{T,max}$ regions scaled by multiplicative factors for easier presentation. The curves represent predictions from PYTHIA6 with different values of k_{FSR}. The error bars on the data points include statistical and systematic uncertainties.
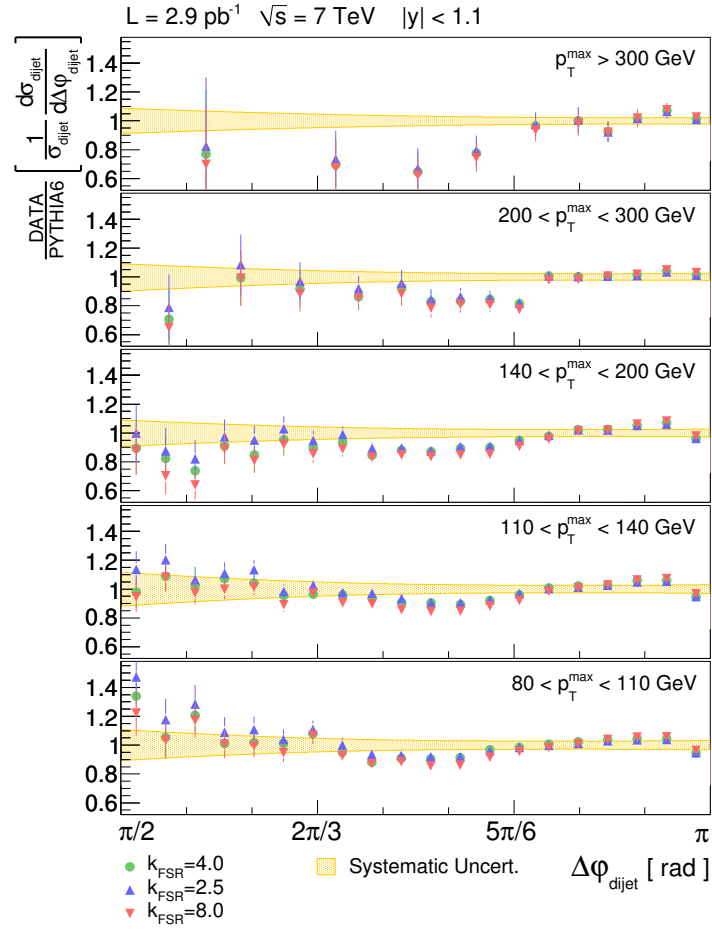
Figure 65. Ratios of measured normalized $\Delta\varphi_{dijet}$ distributions to PYTHIA6 with different values of k_{FSR} in several $p_{T,max}$ regions. The shaded bands indicate the total systematic uncertainties.
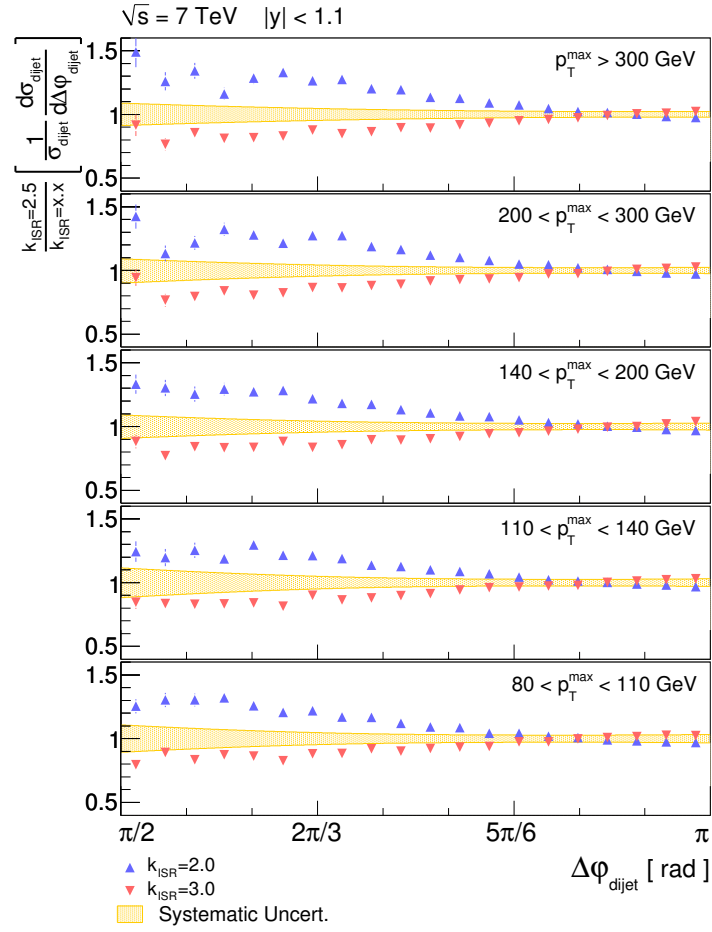
Figure 66. Ratios of $\Delta\varphi_{dijet}$ distributions in PYTHIA6 for different values of k_{ISR}, for several $p_{T,max}$ regions. The shaded bands indicate the total systematic uncertainty.
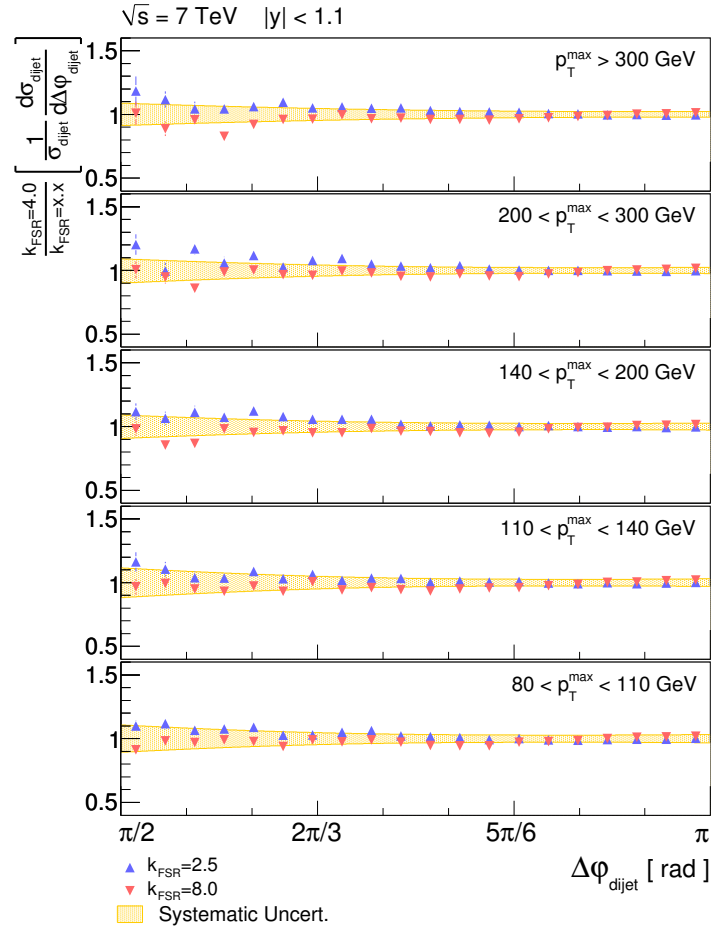
Figure 67. Ratios of $\Delta\varphi_{dijet}$ distributions in PYTHIA6 for different values of k_{FSR}, for several $p_{T,max}$ regions. The shaded bands indicate the total systematic uncertainty.

APPENDICES

Appendix A

DETERMINATION OF THE CALORIMETER JET RECONSTRUCTION EFFICIENCY

The determination of the jet reconstruction efficiency (66) is based on a multi-step procedure involving MC and data measurements. The first step is to measure the jet matching efficiency in data and MC based on a tag-and-probe approach in back-to-back $Z + jet$ events, with a Z boson reconstructed in a dilepton final state.

The tag configuration is defined as a Z boson balanced in p_T by a track jet, while the probe represents a calorimeter jet that matches spatially with the track jet. The jet matching efficiency is then defined as the number of probe calorimeter jets matched to track jets within a $\Delta R = 0.5$, divided by the total number of tags. This topology is illustrated in Figure 68.

The $Z(\mu\mu)+jet$ sample is generated with PYTHIA6 and passed through a GEANT 4 simulation of the CMS detector. Although other final states such as $Z(ee)+jet$ or $\gamma+jet$ can be used as well, it is expected that in the early running of the experiment the $Z \rightarrow \mu\mu$ channel will provide a cleaner signature compared to the other channels.

Events are selected using a double-muon trigger that requires two muons with $p_T > 3$ GeV and $|\eta| < 2.5$. Offline, Z boson candidates are identified by requiring the invariant mass of the two leading muons in the event $(m_{\mu\mu})$ to be within the range $80 < m_{\mu\mu} <$
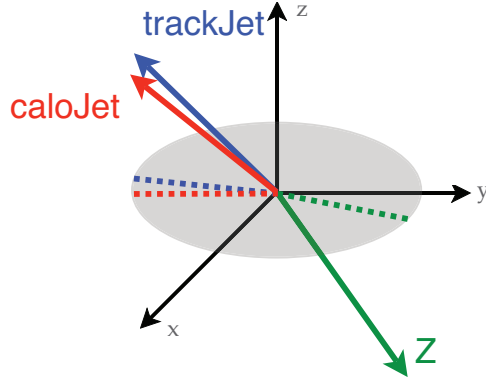
Figure 68. Illustration of a tag-and-probe topology in a $Z + jet$ event.

100 GeV. Both calorimeter and track jets are reconstructed using a seedless infrared-safe cone algorithm with $R = 0.5$. The leading track jet is required to be nearly opposite in azimuth to the Z boson ($\Delta\varphi > 2.7$ radians) and within $|y| < 1.1$. To reduce the additional jet activity, cuts are applied to the p_T ratio between the leading track jet and the Z boson, and between the second track jet and leading track jet. The complete event selection is summarized in Table X.

The tag-and-probe jet matching efficiency in data and MC can be calculated either as a function of the track jet p_T or Z boson p_T. The two observables are complementary with different systematic uncertainties, thus providing a valuable cross-check on the procedure. If the matching efficiency from data is found to disagree with the MC efficiency, the MC will be adjusted to match the data distributions. Once the MC is tuned, the next step is to extract the jet reconstruction efficiency using the mapping technique described below.

Appendix A (Continued)

Selection Cut	Value
Z mass	$80 < m_{\mu\mu} < 100$ GeV
Leading track jet rapidity	$|y| < 1.1$
Topology	$\Delta\varphi(jet1, Z) > 2.7$
Leading track jet p_T	$0.2 < p_{T,jet1}/p_{T,Z} < 0.7$
Second track jet p_T	$p_{T,jet2}/p_{T,jet1} < 0.4$

TABLE X

LIST OF SELECTION CUTS FOR $Z(\mu\mu) + jet$ EVENTS.

The MC truth matching efficiency between generated and calorimeter jets, as a function of the generated jet p_T and for several calorimeter jet p_T thresholds, is shown in Figure 69. The matching criterion is based on $\Delta R < 0.5$ with no explicit restriction on the p_T of calorimeter jets.

To compare the MC truth matching efficiency to the efficiencies extracted by the tag-and-probe method, the generated jet p_T has to be mapped onto the Z boson p_T and the track jet p_T. For this, mapping functions that describe the response and resolution of the generated jet p_T onto the Z boson p_T and track jet p_T as a function of the generated jet p_T are derived and applied to the generated jets accordingly. To account for the effects of different p_T spectra for both Z bosons and track jets, in events with and without a probe calorimeter jet, the two cases are treated separately.

The MC matching efficiency derived from the smeared events is referred to as the mapped MC jet matching efficiency, and labeled in Figure 70 as either MC Truth* if
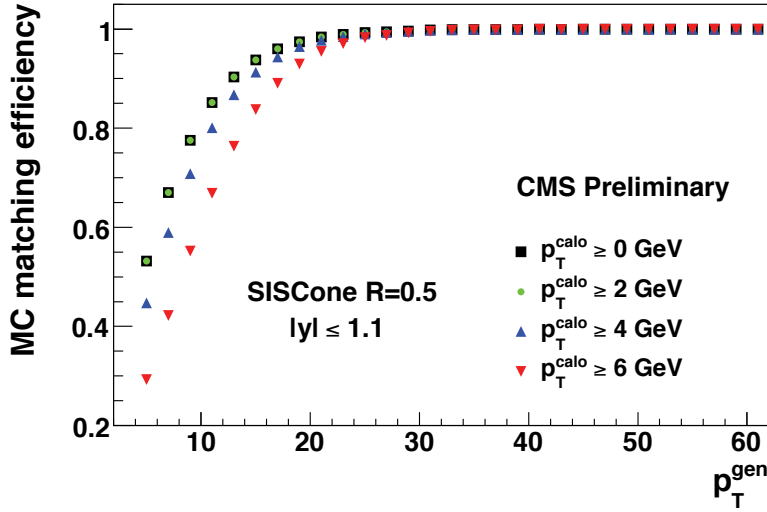
Appendix A (Continued)

Figure 69. MC truth matching efficiency for several calorimeter jet p_T thresholds.

events with and without a probe are treated inclusively or MC Truth** otherwise. Both procedures yield good agreement with the tag-and-probe results.

Systematic uncertainties are estimated by varying each of the event selection requirements ($m_{\mu\mu}$, $\Delta\varphi(jet1, Z)$, $p_{T,jet1}/p_{T,Z}$, and $p_{T,jet2}/p_{T,jet1}$) and repeating the analysis procedure. Furthermore, the track jet energies are varied by $\pm10\%$ in anticipation of possible discrepancies between early collision data and the simulation. All individual contributions are summed in quadrature and the total systematic uncertainty derived.

In order to extract the fully corrected jet reconstruction efficiency, the MC matching efficiency, that yields good agreement with the data tag-and-probe results, needs to be corrected for the finite position resolution in η and φ of calorimeter jets. This is done
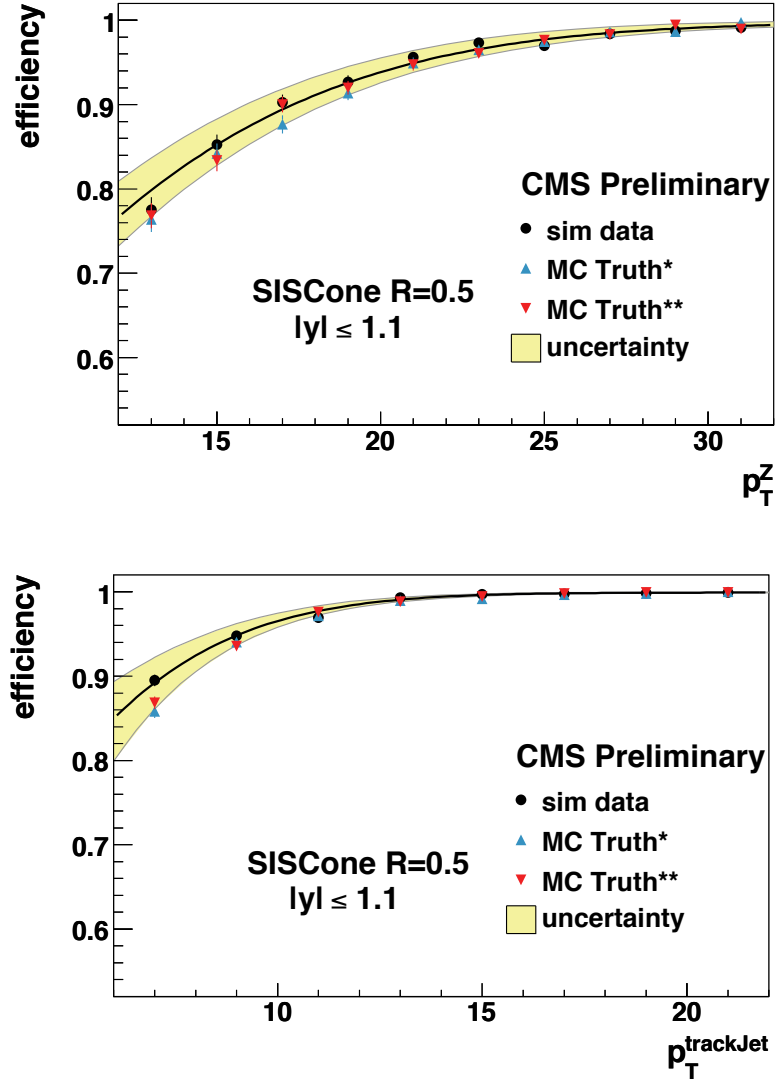
Appendix A (Continued)

Figure 70. The tag-and-probe jet matching efficiency enveloped by the total systematic uncertainty as a function of Z boson p_T (top) and uncorrected track jet p_T (bottom). The minimum p_T of the Z boson and the track jet are selected to correspond to a generated jet p_T of ≈ 7 GeV. The line represents a fit to the simulated data.

Appendix A (Continued)

by smearing the position of generated jets with the measured resolution in η and φ of calorimeter jets.

Figure 71 demonstrates the probability of a spatially smeared generated jet to satisfy the matching criterion of $\Delta R < 0.5$ with respect to its original location as a function of the generated jet p_T. The effect is found to be sizable only for $p_T < 15$ GeV, consistent with the fact that the position resolution improves with p_T.
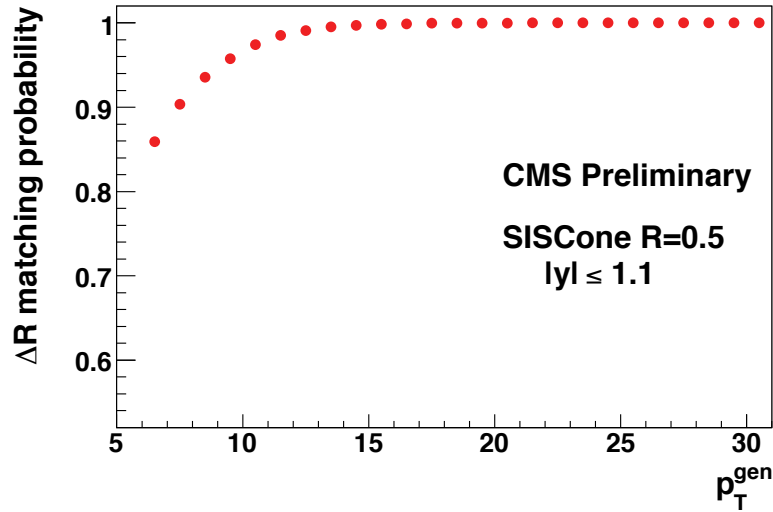

Figure 71. Matching probability between spatially smeared generated jets and generated jets for $\Delta R < 0.5$.

Appendix A (Continued)

The fully corrected jet reconstruction efficiency (Figure 72) as a function of the gener-

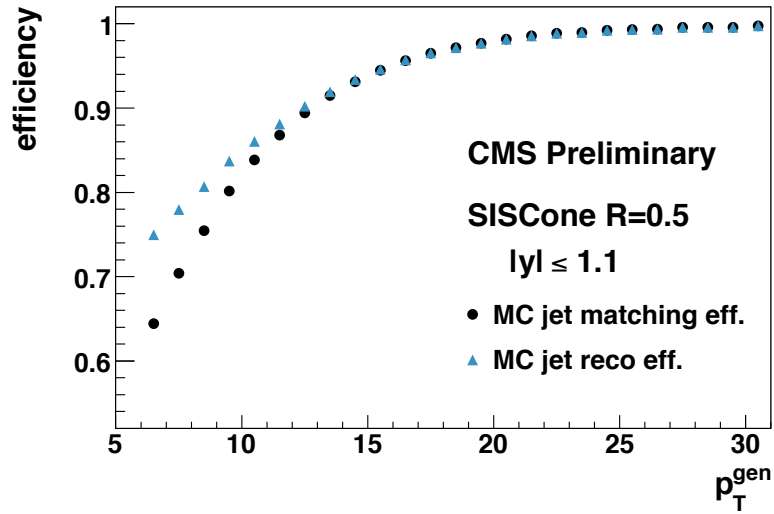ated jet p_T is obtained by applying the position resolution correction to the MC matching

efficiency.

Figure 72. MC jet matching efficiency (black circles) and fully corrected MC jet
reconstruction efficiency (blue triangles).
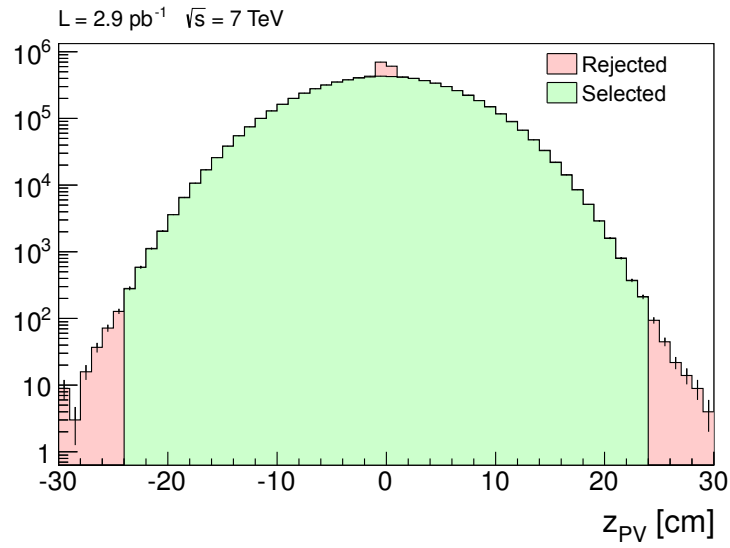
Appendix B

PRIMARY VERTEX AND JET ID CUTS

Figure 73. Primary vertex position on the z-axis in data before and after applying the primary vertex selection cuts (Section 7.1.2).
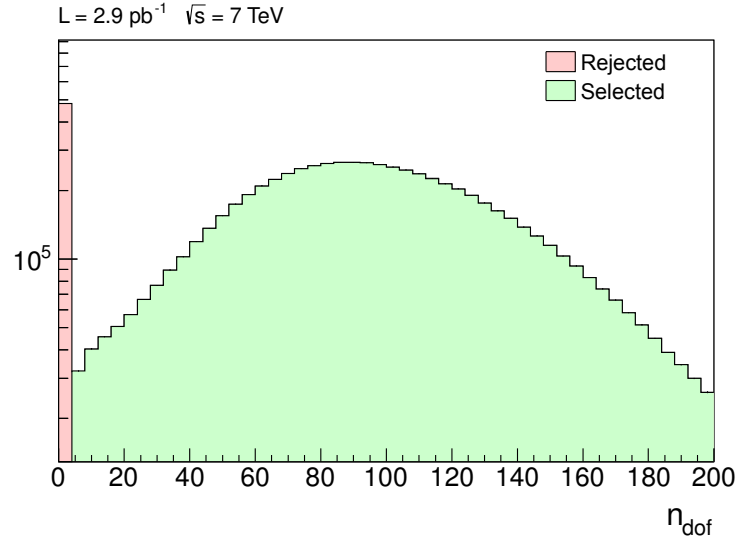
Appendix B (Continued)

Figure 74. Number of degrees of freedom for the primary vertex in data before and after applying the primary vertex selection cuts (Section 7.1.2).
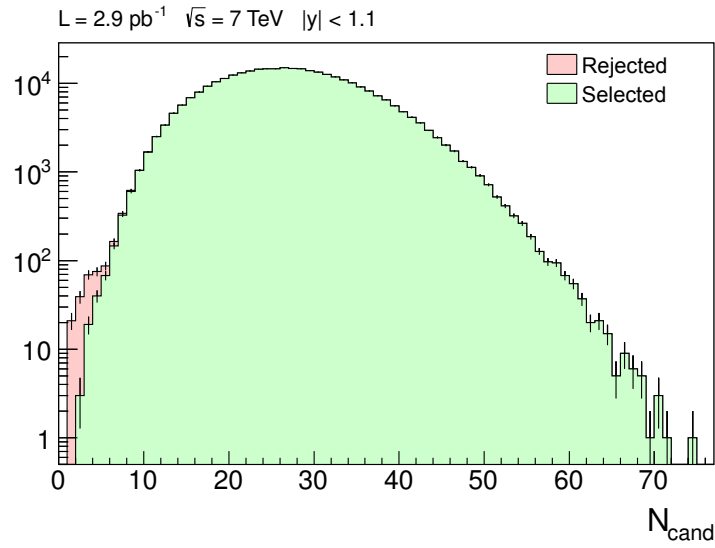

Figure 75. Number of candidates for the leading PF jet in data before and after applying the PF jet identification (Section 5.5.3).
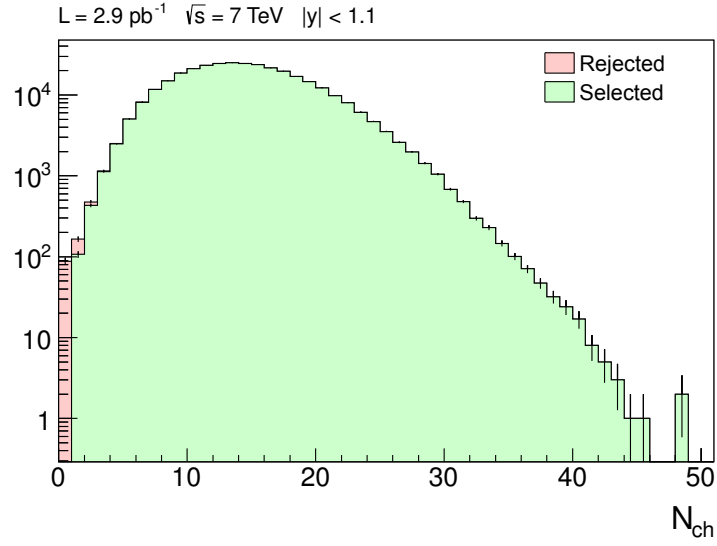
Appendix B (Continued)

Figure 76. Number of charged hadrons for the leading PF jet in data before and after applying the PF jet identification (Section 5.5.3).
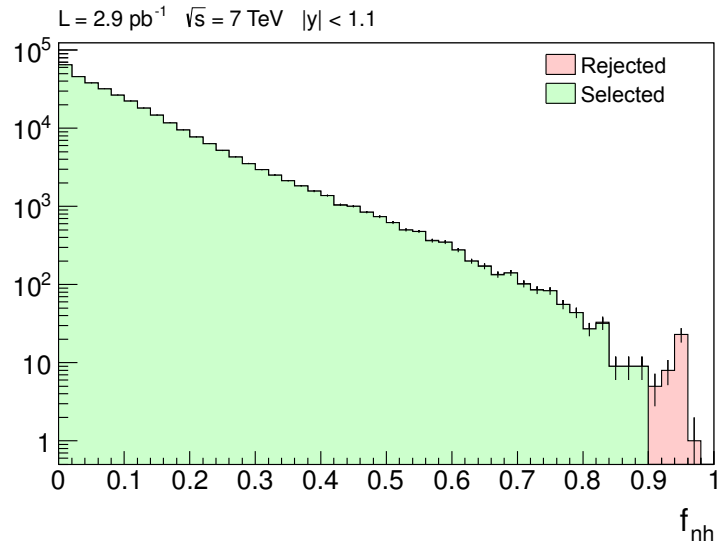

Figure 77. Fraction of energy contributed by neutral hadrons to the leading PF jet in data before and after applying the PF jet identification (Section 5.5.3).
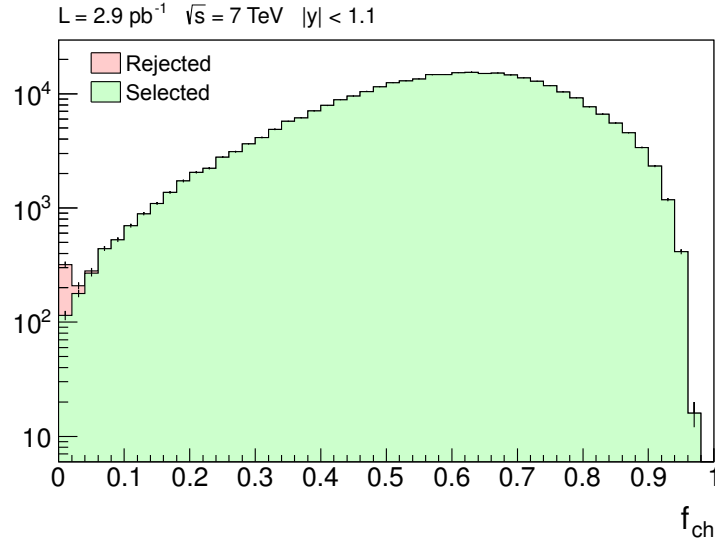
Appendix B (Continued)

Figure 78. Fraction of energy contributed by charged hadrons to the leading PF jet in data before and after applying the PF jet identification (Section 5.5.3).
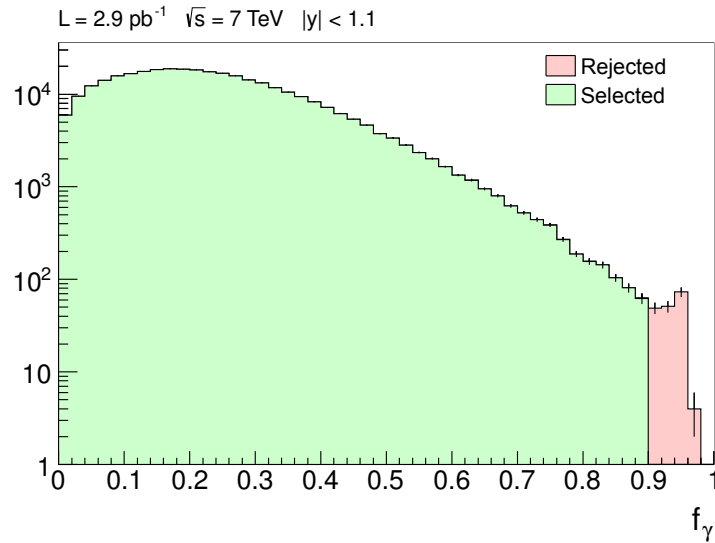

Figure 79. Fraction of energy contributed by neutral EM particles to the leading PF jet in data before and after applying the PF jet identification (Section 5.5.3).

Appendix B (Continued)
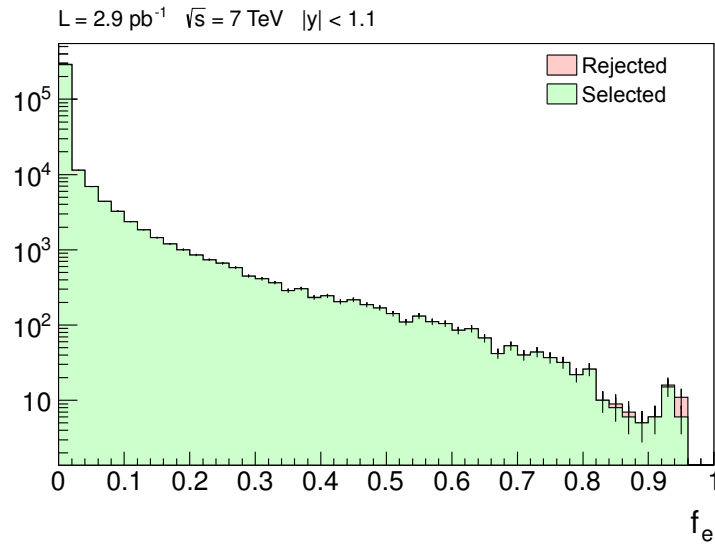

Figure 80. Fraction of energy contributed by charged EM particles to the leading PF jet in data before and after applying the PF jet identification (Section 5.5.3).

Appendix C

DATA TO MONTE CARLO COMPARISONS
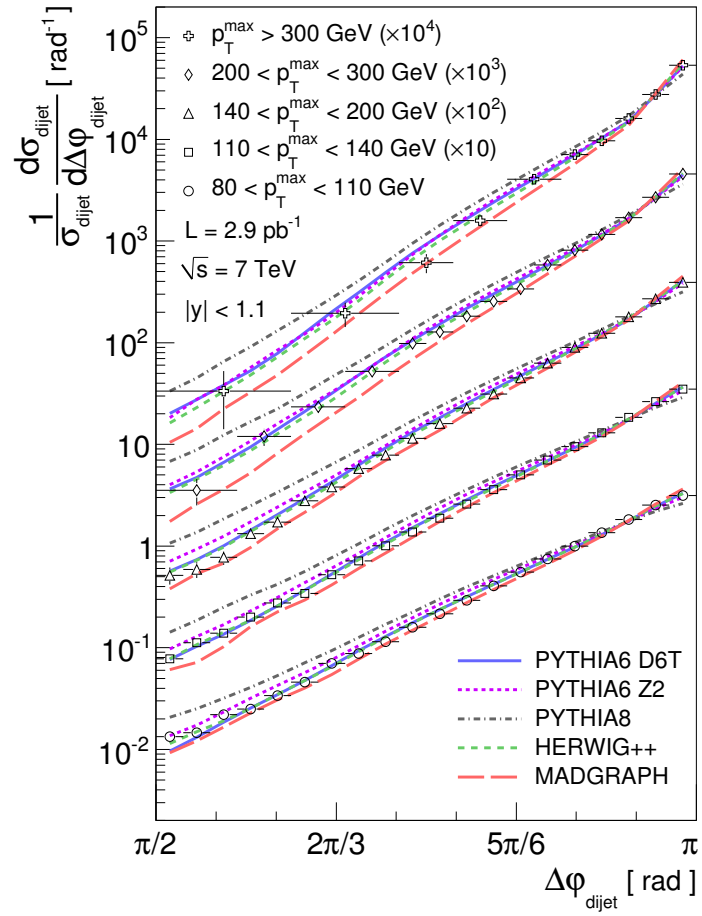
Figure 81. $\Delta\varphi_{dijet}$ distributions in data and MC.

Appendix C (Continued)
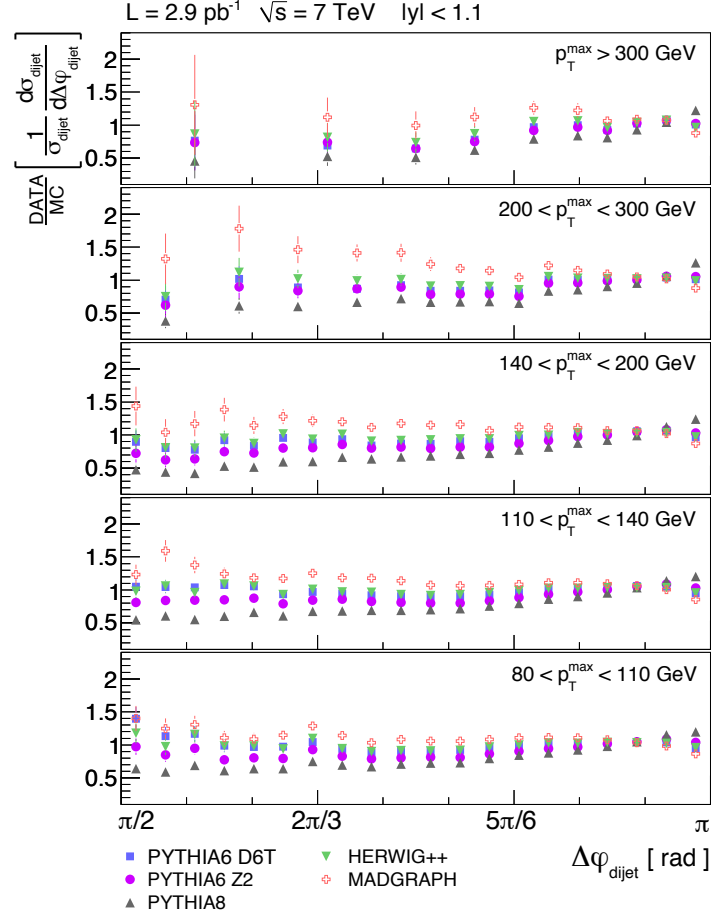
Figure 82. Ratios of $\Delta\varphi_{dijet}$ distributions from data and MC.

Appendix C (Continued)

Figure 83. First jet p_T distributions for $80 < p_{T,max} < 110$ GeV in data and MC (top) and ratios between data and MC (bottom).

Appendix C (Continued)

Figure 84. First jet p_T distributions for $p_{T,max} > 110$ GeV in data and MC (top) and ratios between data and MC (bottom).

Appendix C (Continued)

L = 2.9 pb⁻¹ √s = 7 TeV |y| < 1.1

$80 < p_T^{max} < 110$ GeV

PYTHIA6 D6T
PYTHIA6 Z2
PYTHIA8
HERWIG++
MADGRAPH
DATA

$p_{T,jet2}$ [GeV]

L = 2.9 pb⁻¹ √s = 7 TeV |y| < 1.1

$\frac{DATA}{MC}$

$80 < p_T^{max} < 110$ GeV

PYTHIA6 D6T
PYTHIA6 Z2
PYTHIA8
HERWIG++
MADGRAPH

$p_{T,jet2}$ [GeV]
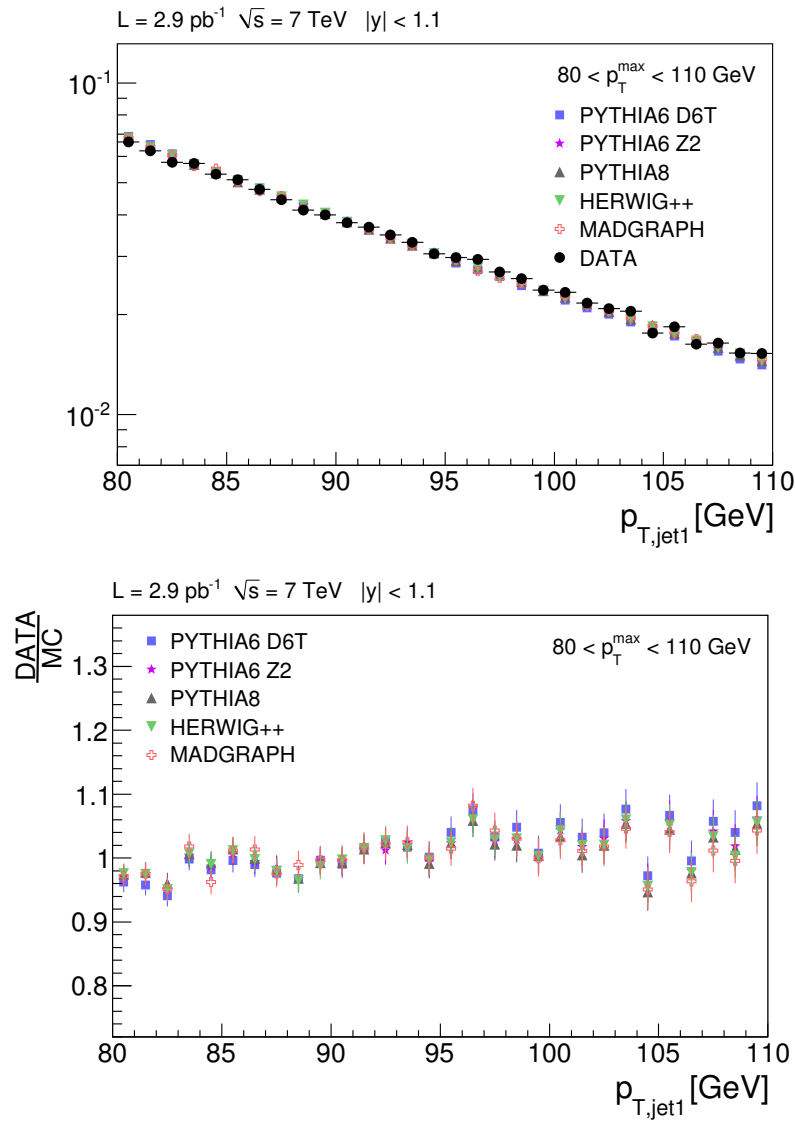
Figure 85. Second jet p_T distributions for $80 < p_{T,max} < 110$ GeV in data and MC (top) and ratios between data and MC (bottom).

Appendix C (Continued)

Figure 86. Second jet p_T distributions for $p_{T,max} > 110$ GeV in data and MC (top) and ratios between data and MC (bottom).

Appendix C (Continued)

L = 2.9 pb⁻¹ √s = 7 TeV |y| < 1.1

$80 < p_T^{max} < 110$ GeV

PYTHIA6 D6T
PYTHIA6 Z2
PYTHIA8
HERWIG++
MADGRAPH
DATA

$p_{T,jet3}$ [GeV]

Figure 87. Third jet p_T distributions for $80 < p_{T,max} < 110$ GeV in data and MC (top) and ratios between data and MC (bottom).

Appendix C (Continued)

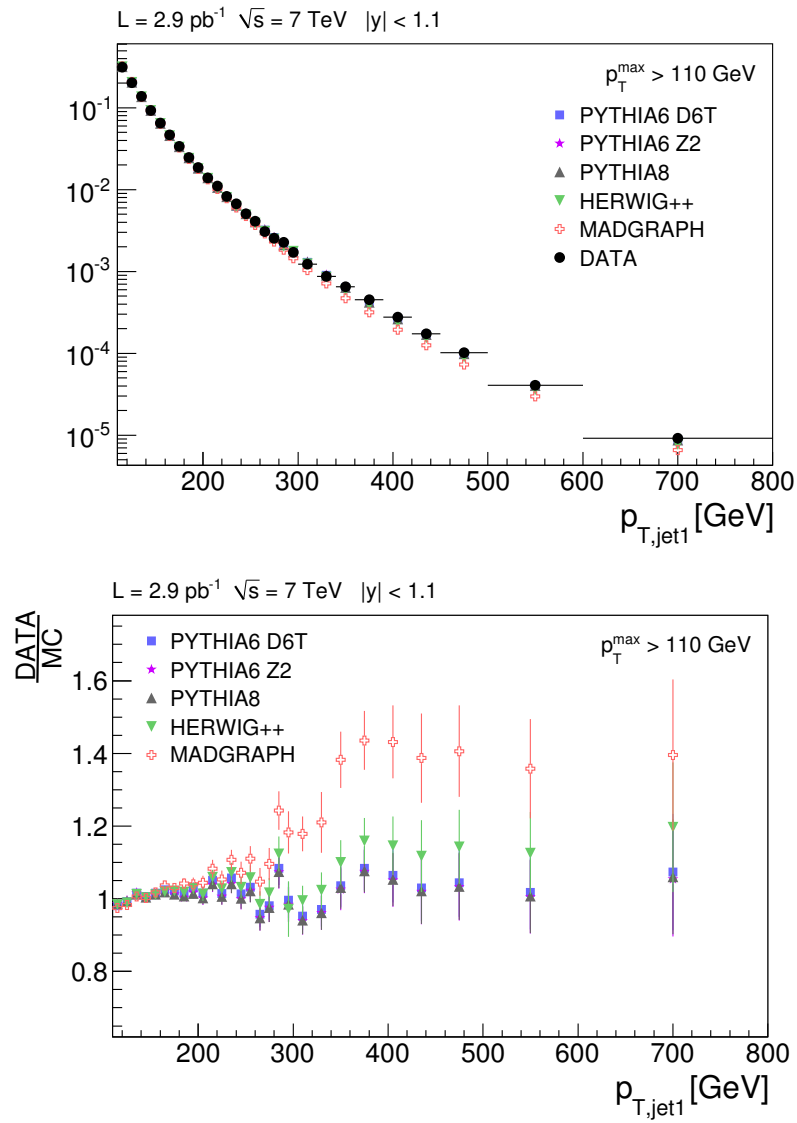Figure 88. Third jet p_T distributions for $p_{T,max} > 110$ GeV in data and MC (top) and ratios between data and MC (bottom).

Appendix C (Continued)

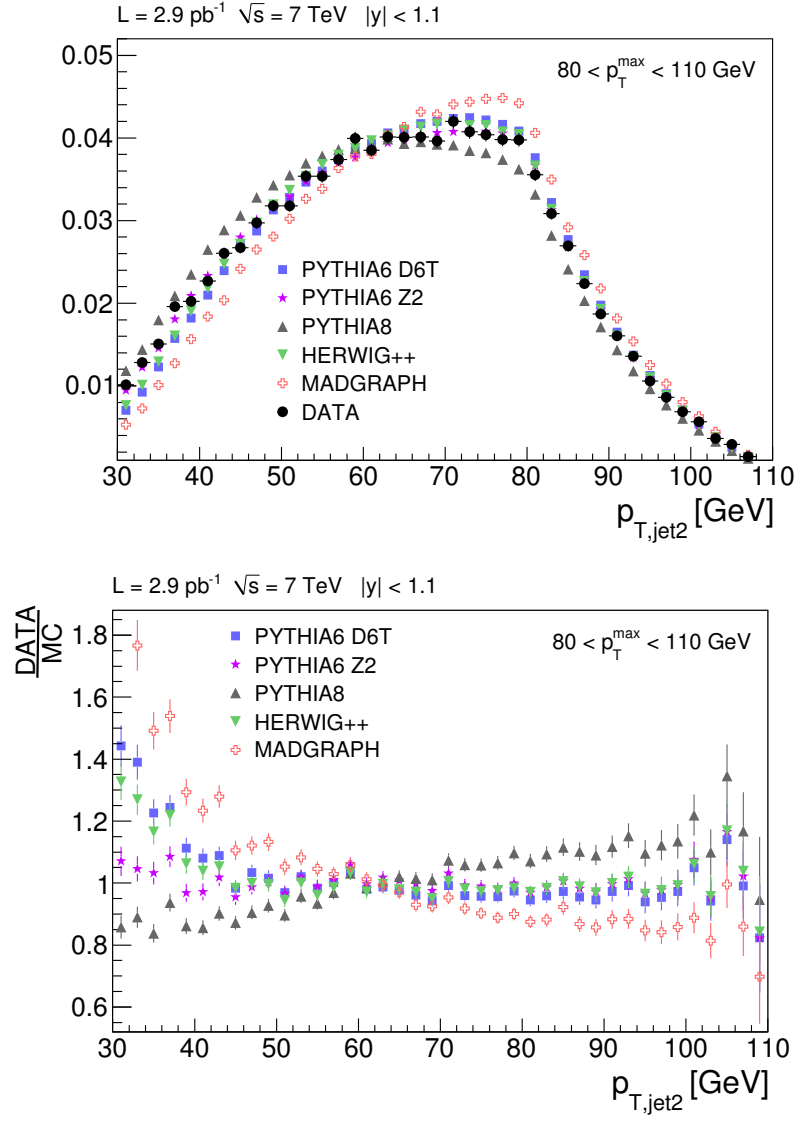Figure 89. $p_{T,jet2}/p_{T,jet1}$ distributions for $80 < p_{T,max} < 110$ GeV in data and MC (top) and ratios between data and MC (bottom).

Appendix C (Continued)

Figure 90. $p_{T,jet2}/p_{T,jet1}$ distributions for $p_{T,max} > 110$ GeV in data and MC (top) and ratios between data and MC (bottom).

Appendix C (Continued)
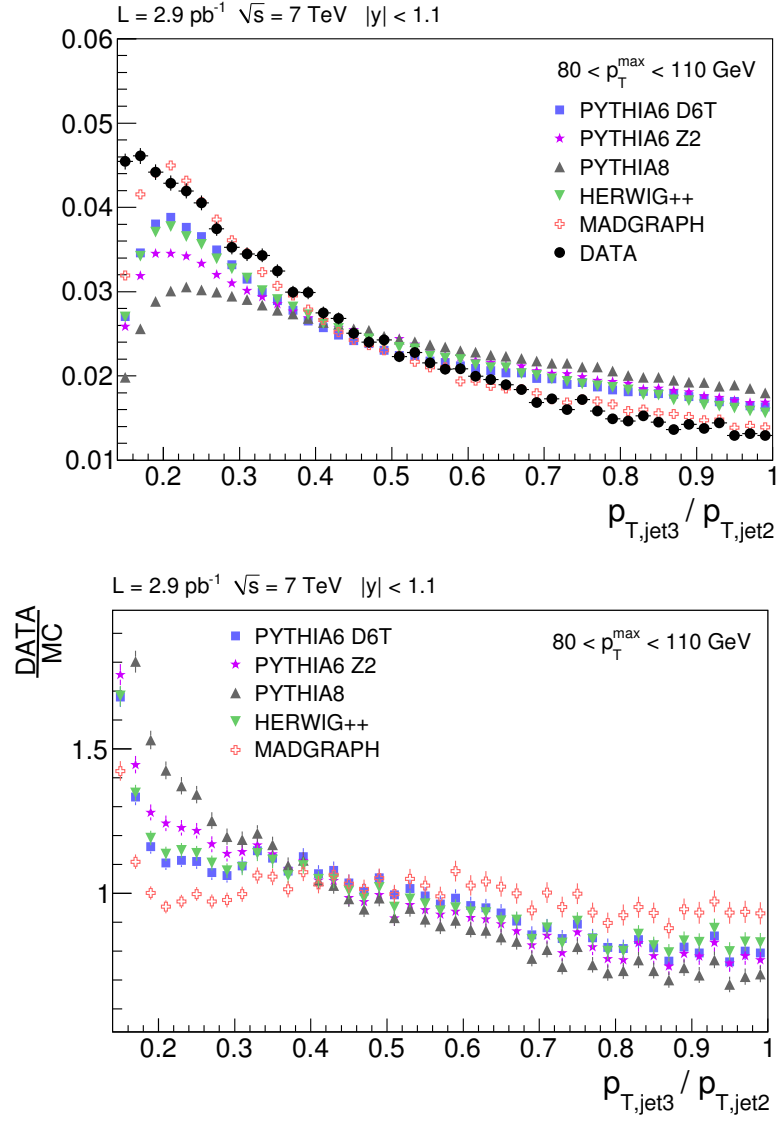
Figure 91. $p_{T,jet3}/p_{T,jet2}$ distributions for $80 < p_{T,max} < 110$ GeV in data and MC (top) and ratios between data and MC (bottom).

Appendix C (Continued)
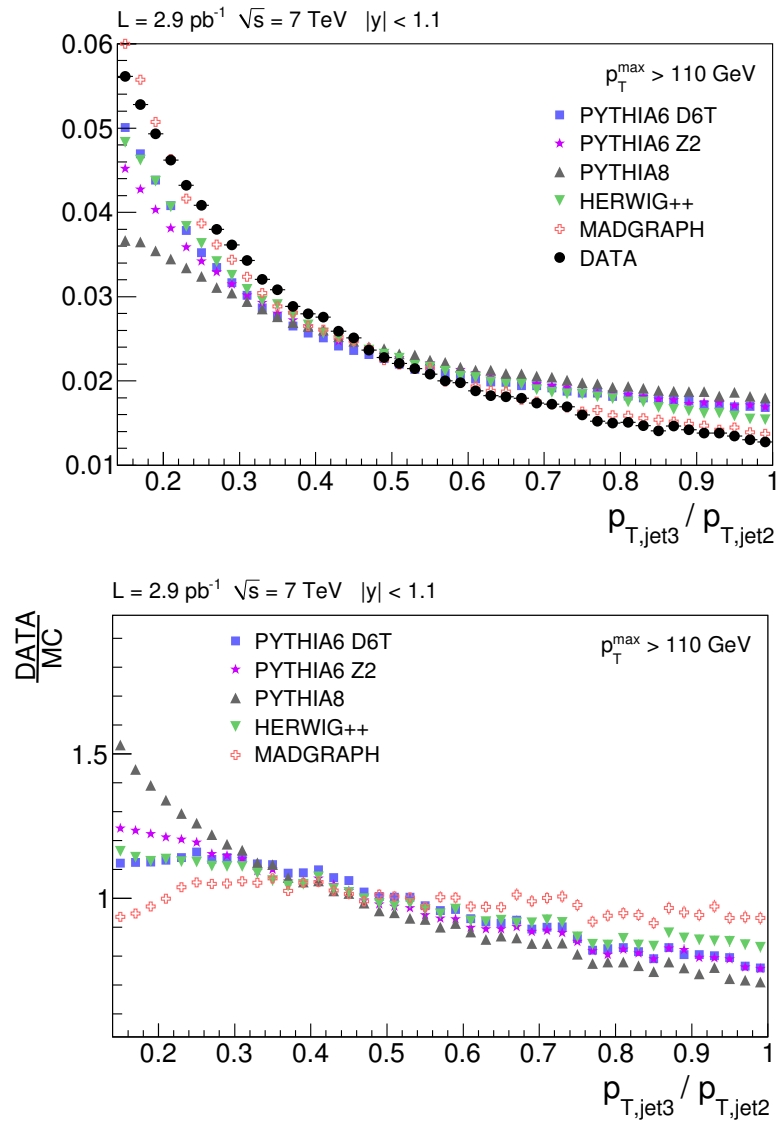
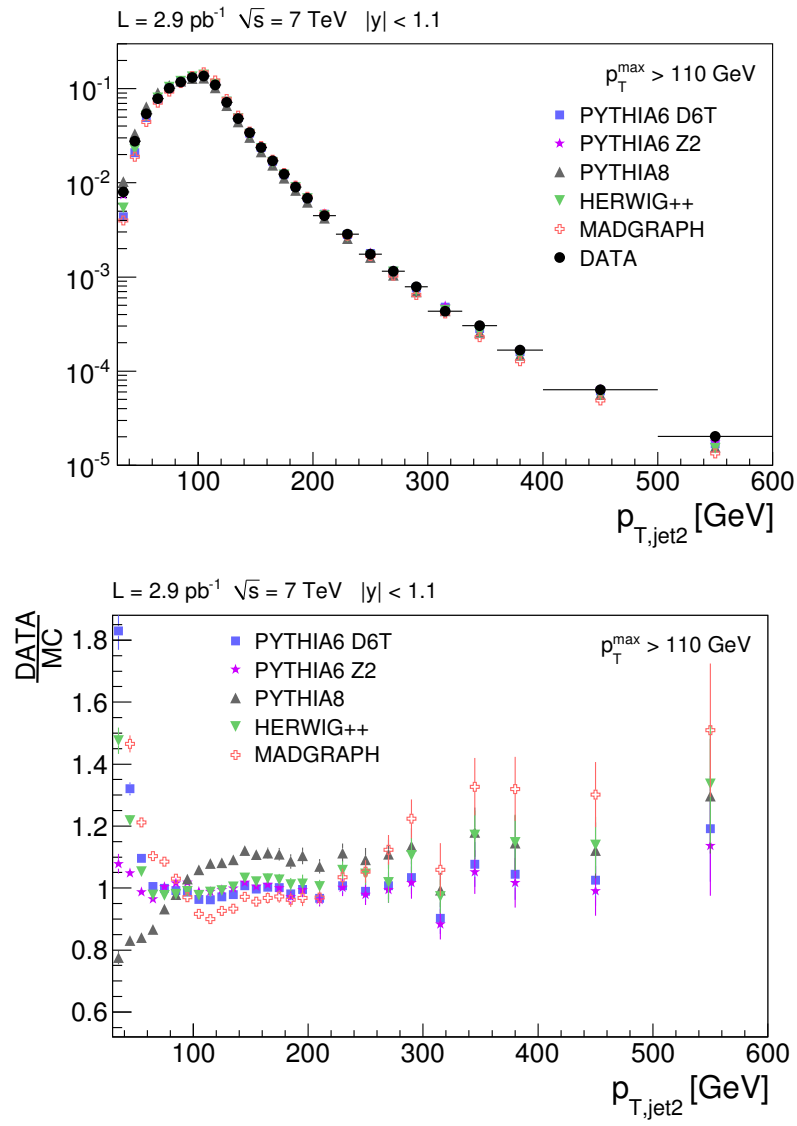Figure 92. $p_{T,jet3}/p_{T,jet2}$ distributions for $p_{T,max} > 110$ GeV in data and MC (top) and ratios between data and MC (bottom).

Appendix C (Continued)
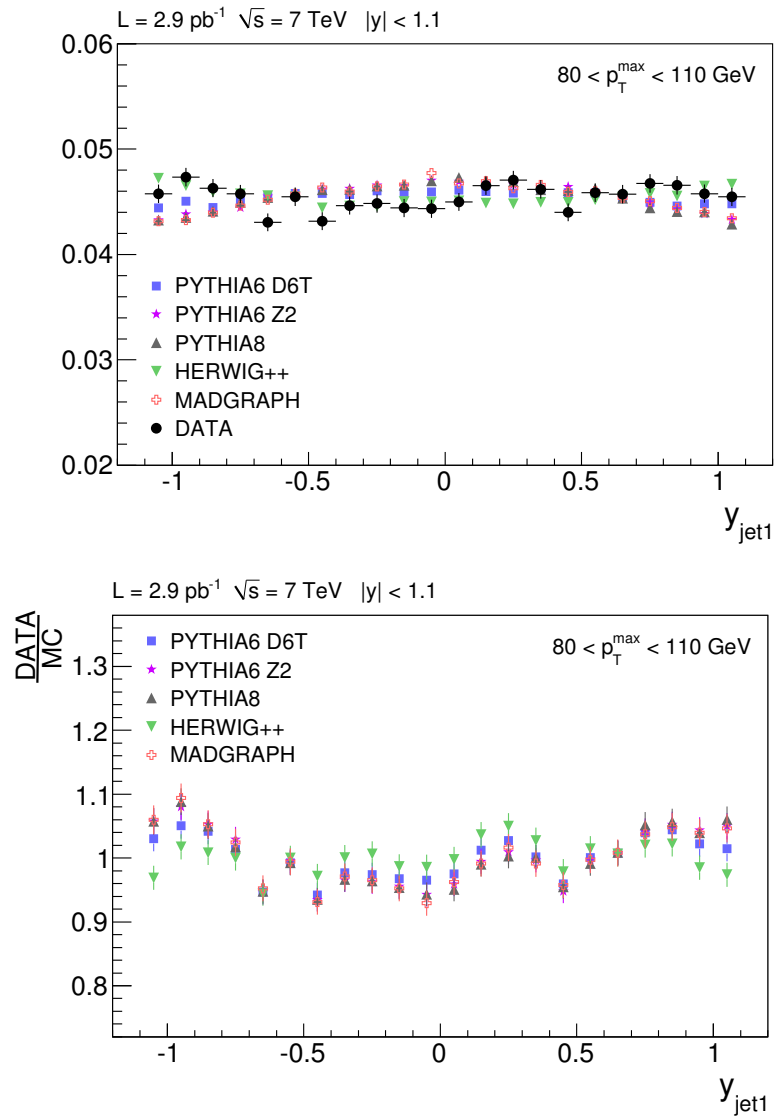
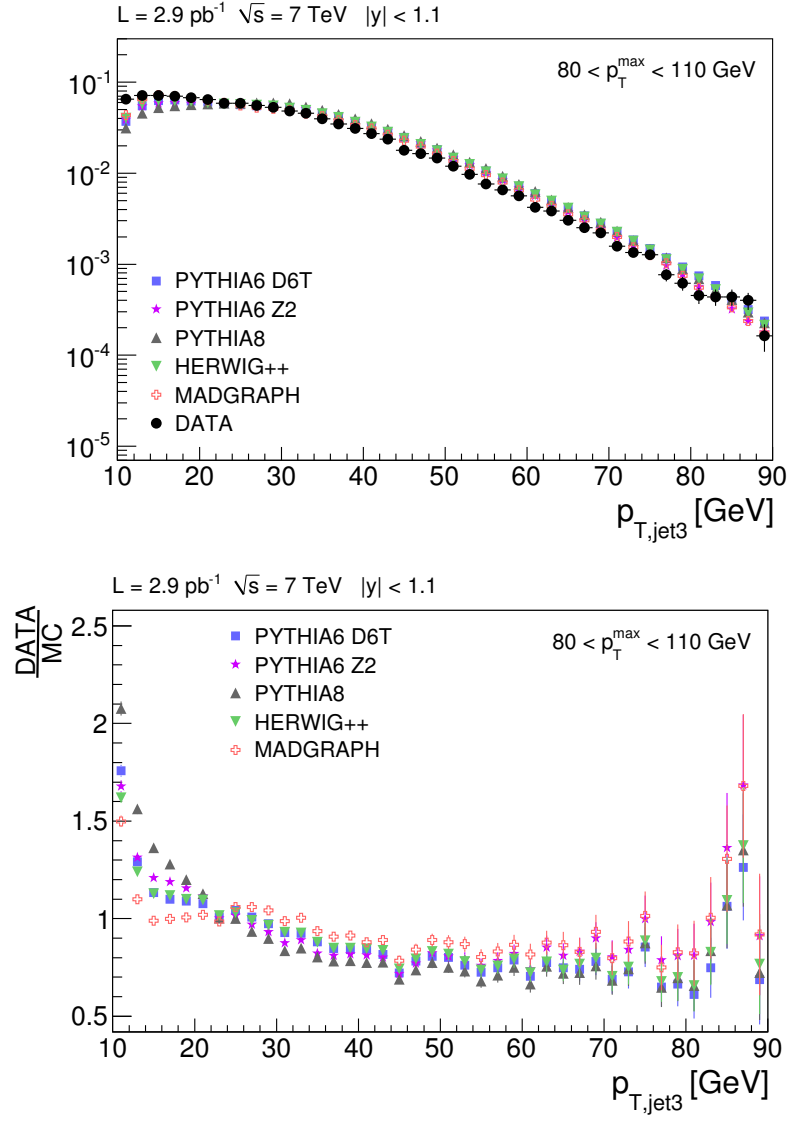Figure 93. First jet rapidity distributions for $80 < p_{T,max} < 110$ GeV in data and MC (top) and ratios between data and MC (bottom).

Appendix C (Continued)
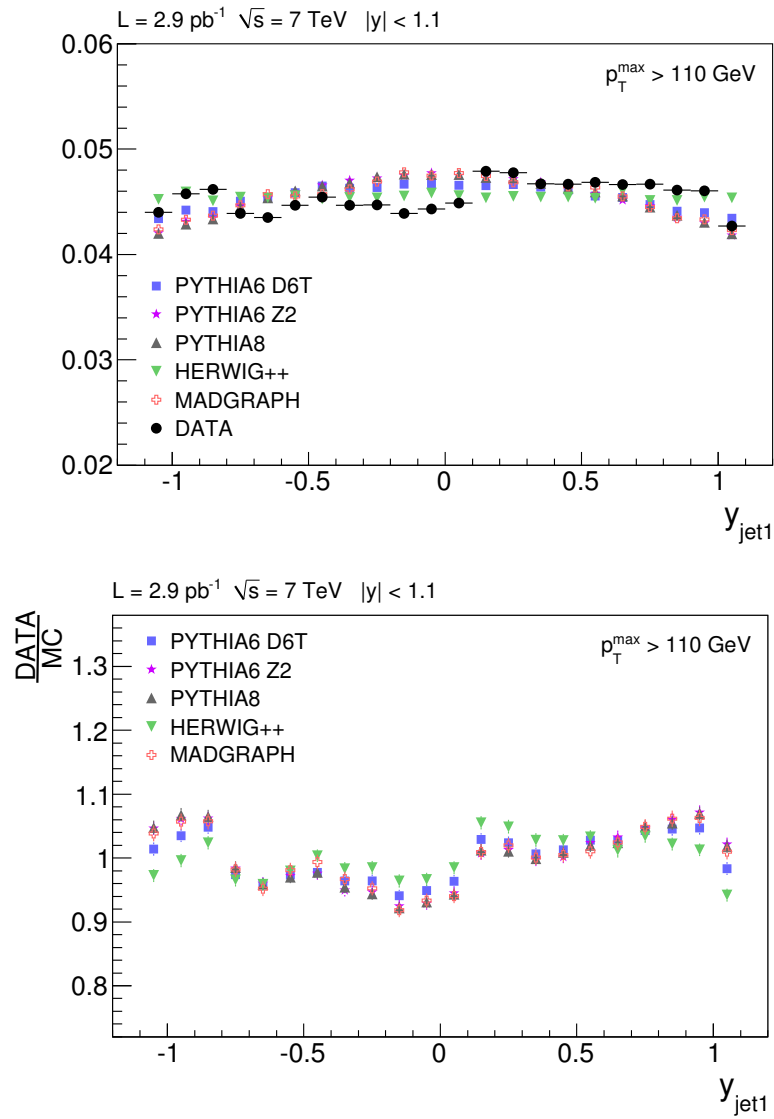
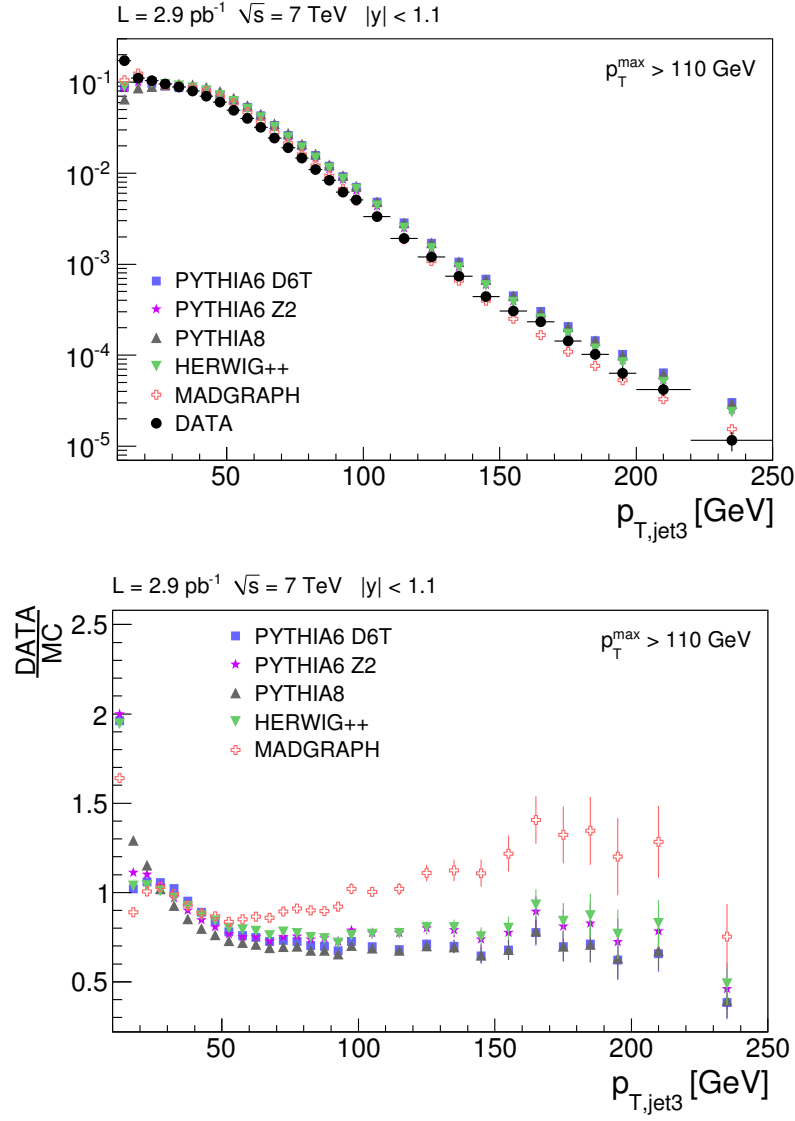

Figure 94. First jet rapidity distributions for $p_{T,max} > 110$ GeV in data and MC (top) and ratios between data and MC (bottom).

Appendix C (Continued)
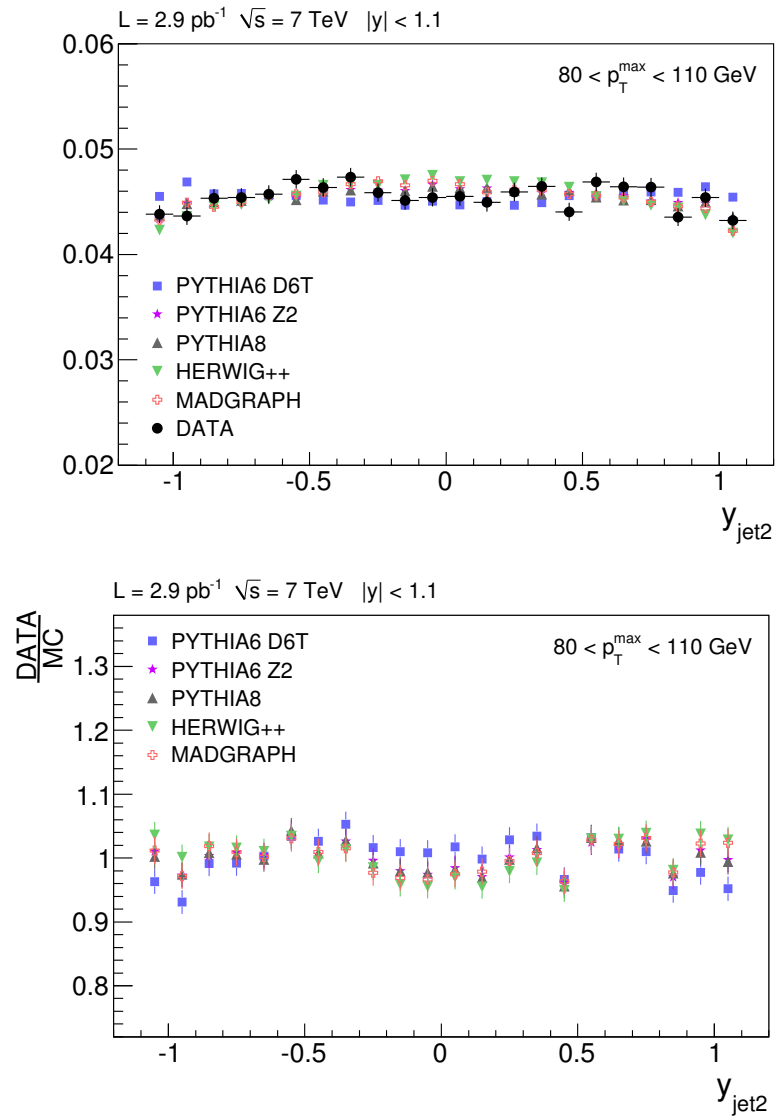
Figure 95. Second jet rapidity distributions for $80 < p_{T,max} < 110$ GeV in data and MC (top) and ratios between data and MC (bottom).

Appendix C (Continued)

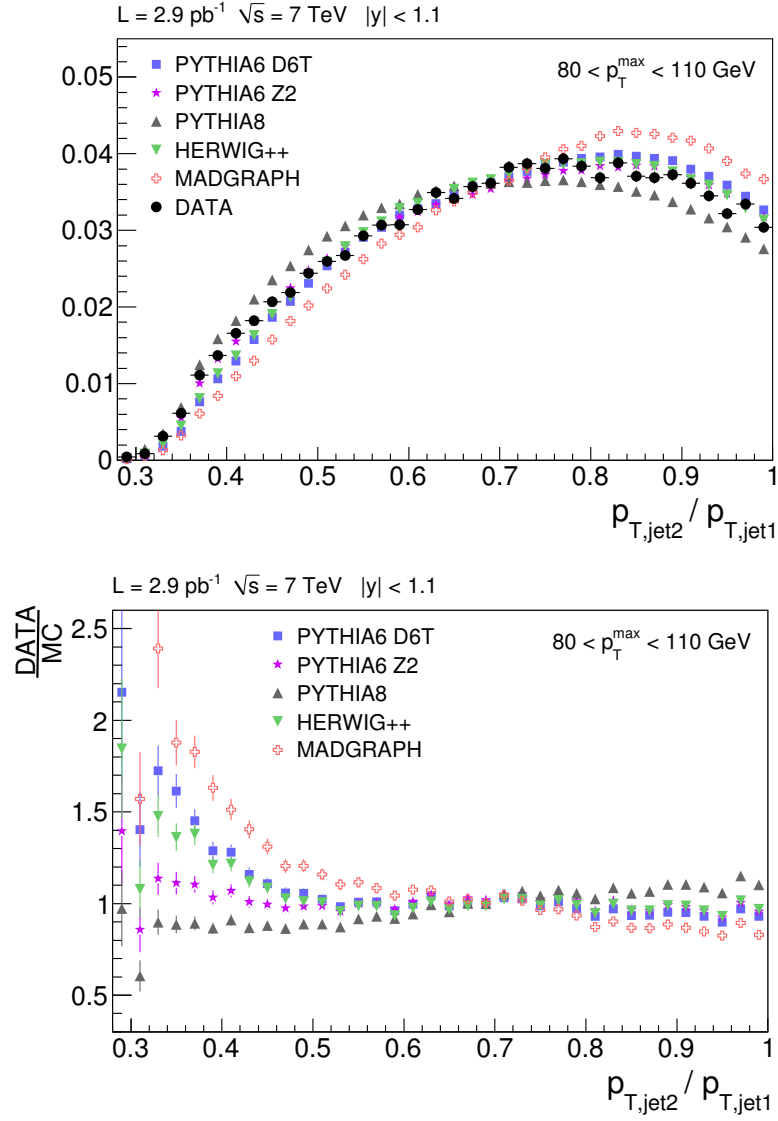

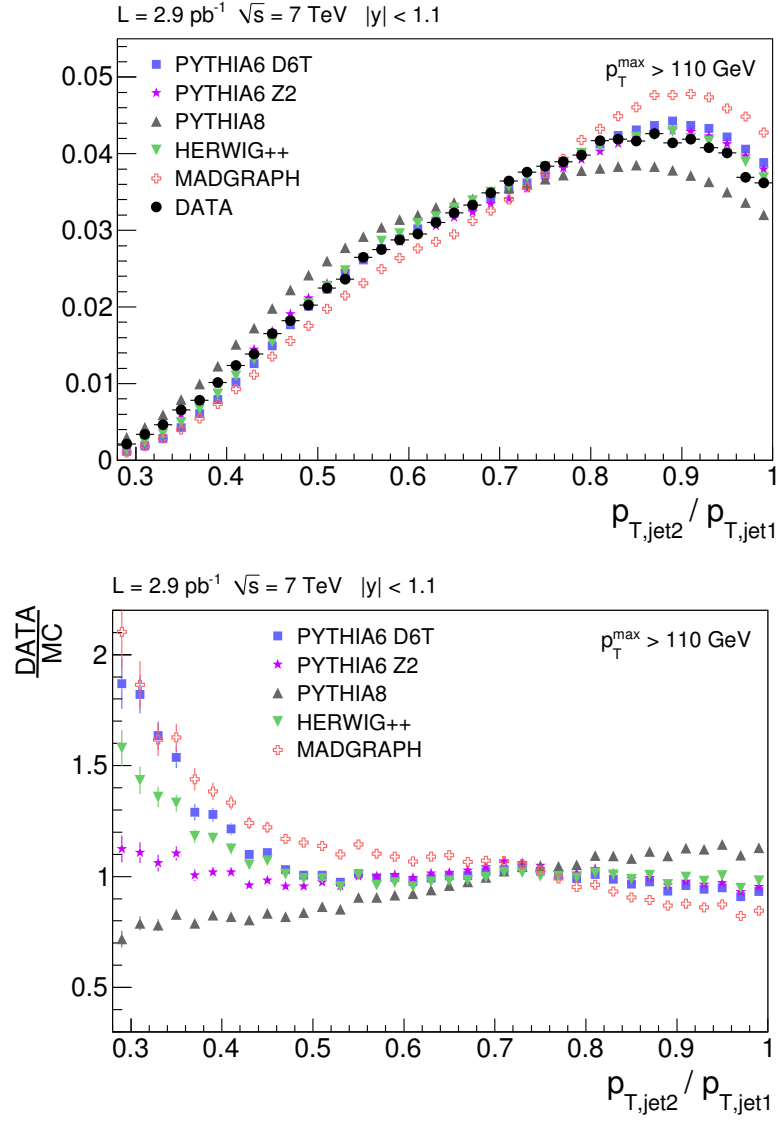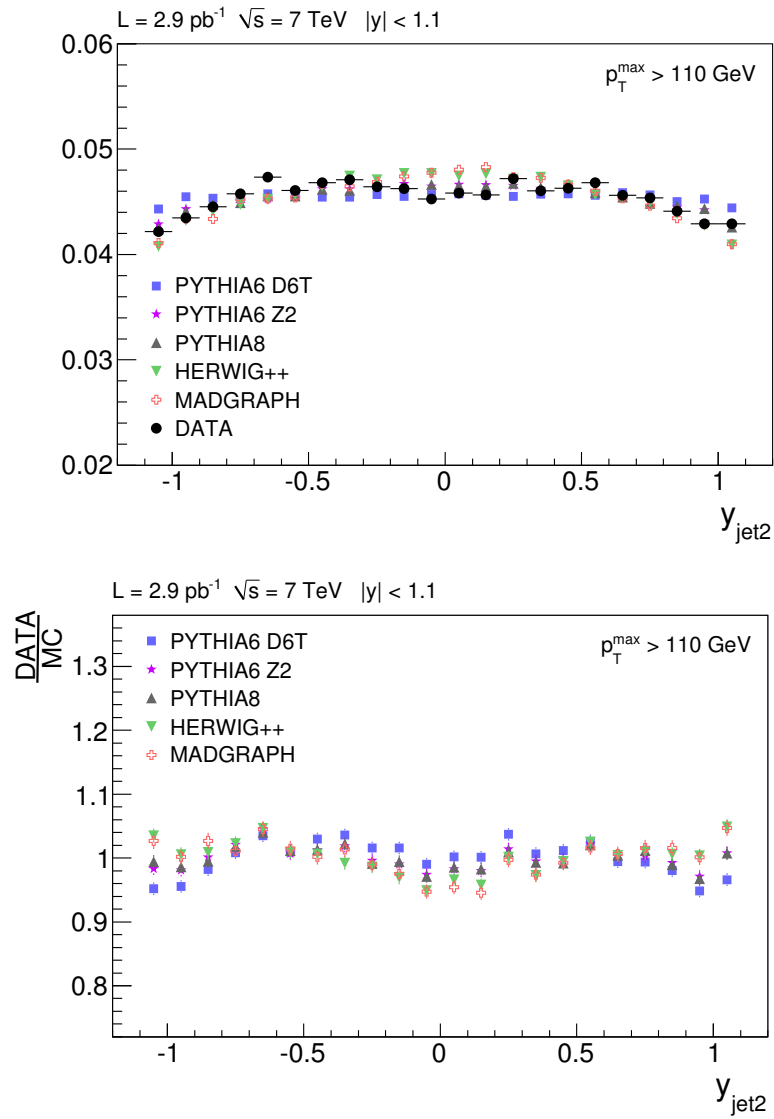Figure 96. Second jet rapidity distributions for $p_{T,max} > 110$ GeV in data and MC (top) and ratios between data and MC (bottom).

Appendix D

COMPARISONS BETWEEN DATA AND PYTHIA6 D6T WITH DIFFERENT k_{ISR} VALUES

Appendix D (Continued)
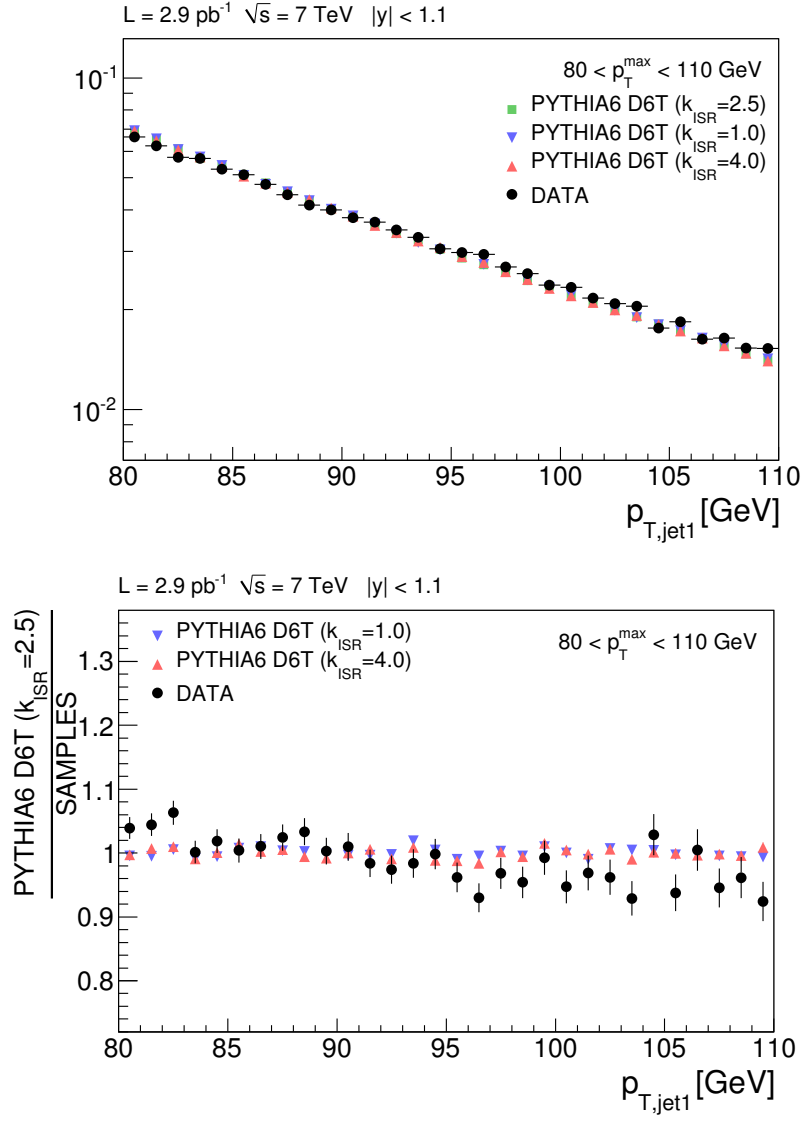
Figure 97. First jet p_T distributions for $80 < p_{T,max} < 110$ GeV in data and PYTHIA6 D6T with different k_{ISR} values (top) and ratios between data and PYTHIA6 D6T (bottom).

Appendix D (Continued)
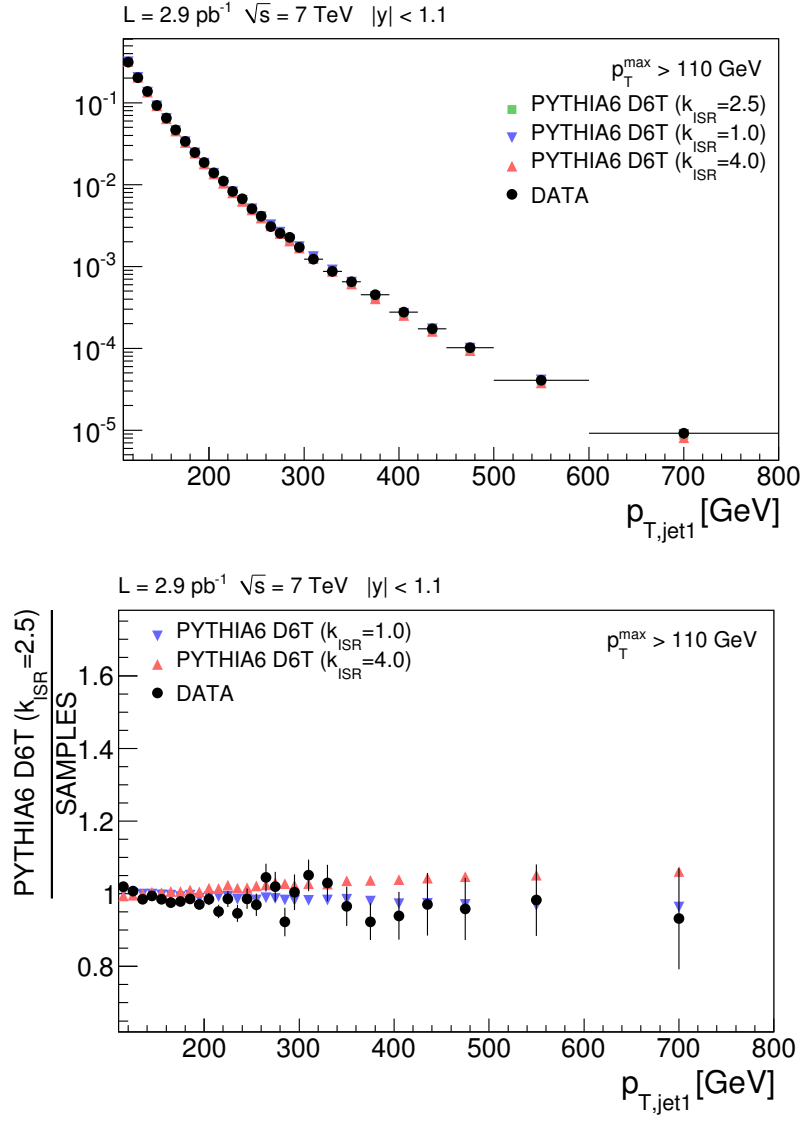
Figure 98. First jet p_T distributions for $p_{T,max} > 110$ GeV in data and PYTHIA6 D6T with different k_{ISR} values (top) and ratios between data and PYTHIA6 D6T (bottom).

Appendix D (Continued)
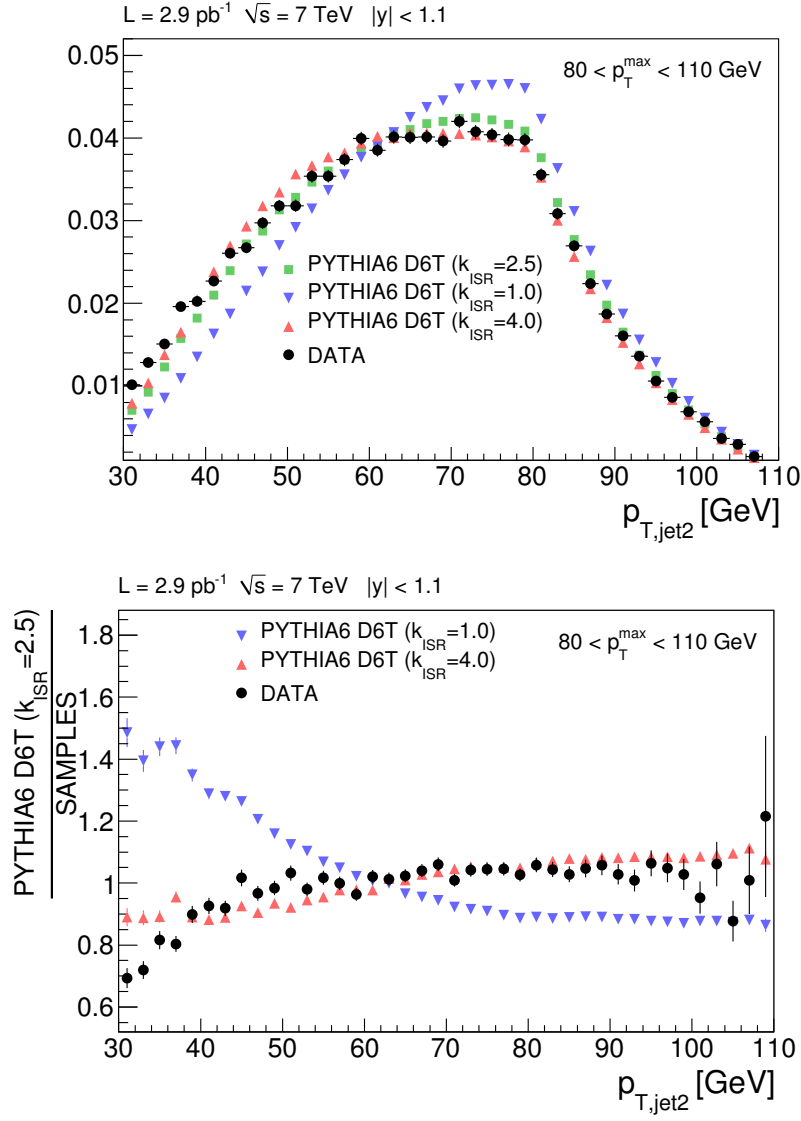
Figure 99. Second jet p_T distributions for $80 < p_{T,max} < 110$ GeV in data and PYTHIA6 D6T with different k_{ISR} values (top) and ratios between data and PYTHIA6 D6T (bottom).

Appendix D (Continued)
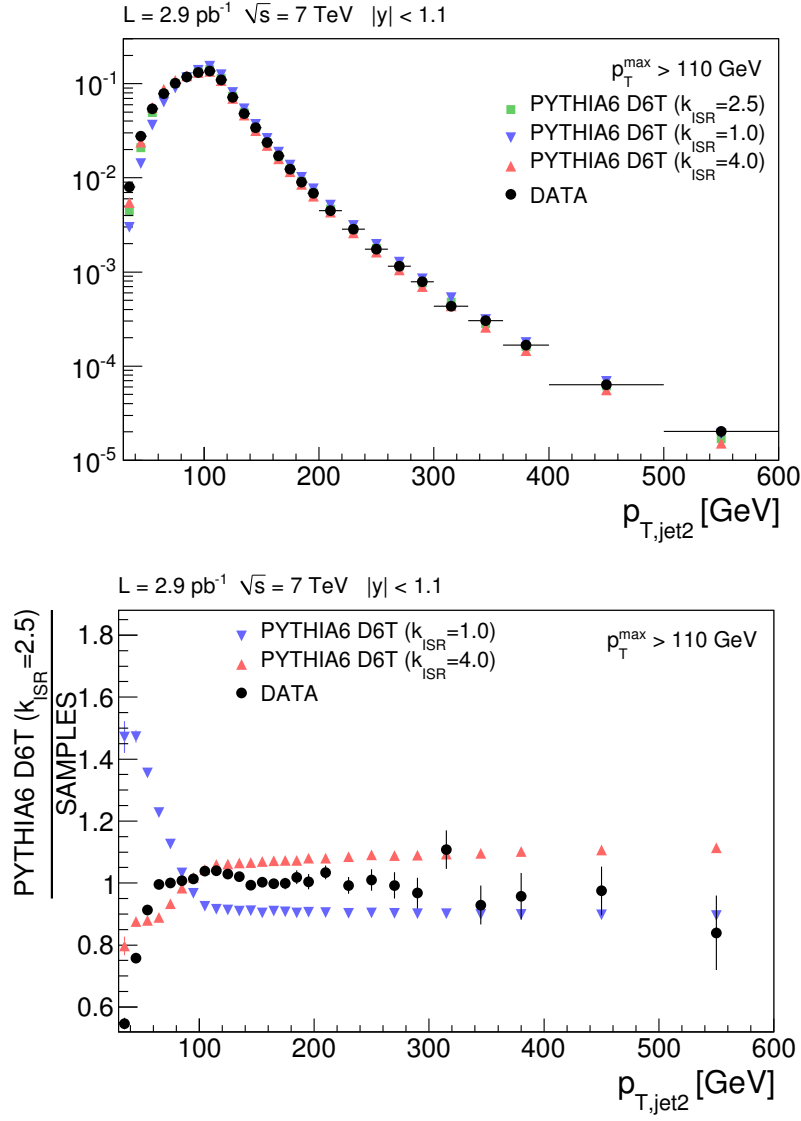
Figure 100. Second jet p_T distributions for $p_{T,max} > 110$ GeV in data and PYTHIA6 D6T with different k_{ISR} values (top) and ratios between data and PYTHIA6 D6T (bottom).

Appendix D (Continued)

Figure 101. Third jet p_T distributions for $80 < p_{T,max} < 110$ GeV in data and PYTHIA6 D6T with different k_{ISR} values (top) and ratios between data and PYTHIA6 D6T (bottom).

Appendix D (Continued)

L = 2.9 pb⁻¹ √s = 7 TeV |y| < 1.1

Figure 102. Third jet p_T distributions for $p_{T,max} > 110$ GeV in data and PYTHIA6 D6T with different k_{ISR} values (top) and ratios between data and PYTHIA6 D6T (bottom).

Appendix E

DIJET AZIMUTHAL DECORRELATIONS IN DATA

Appendix E (Continued)

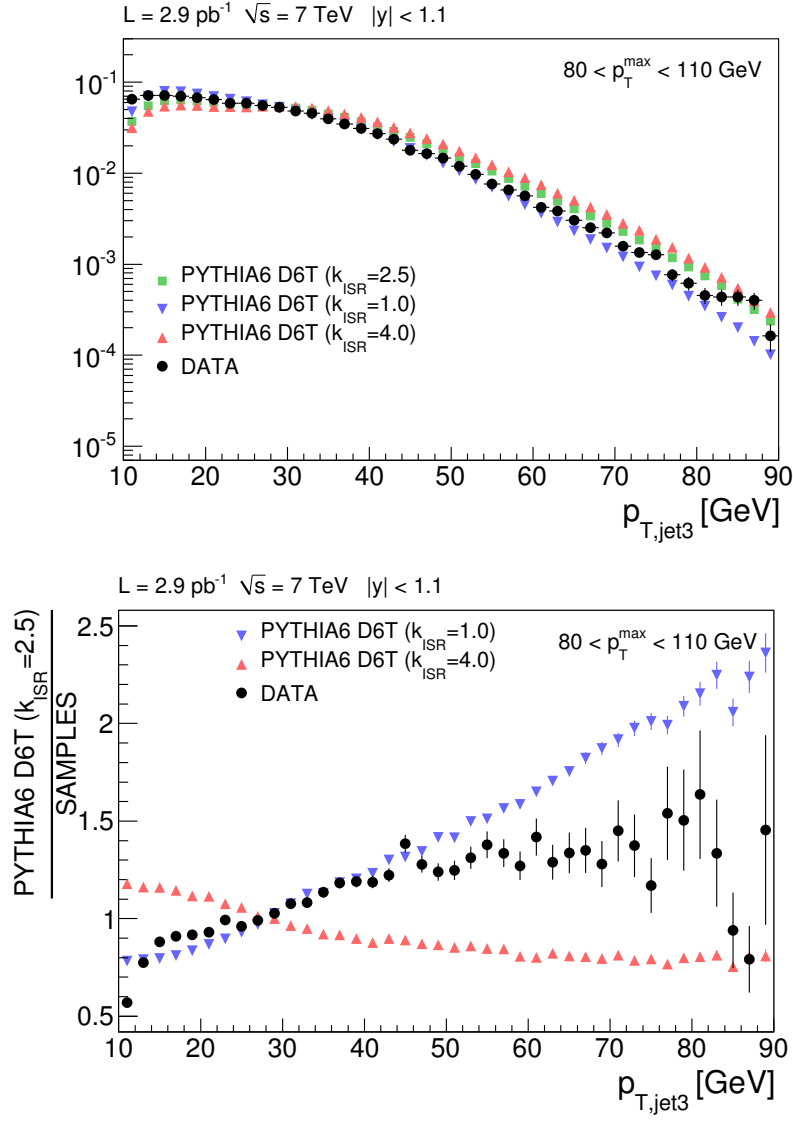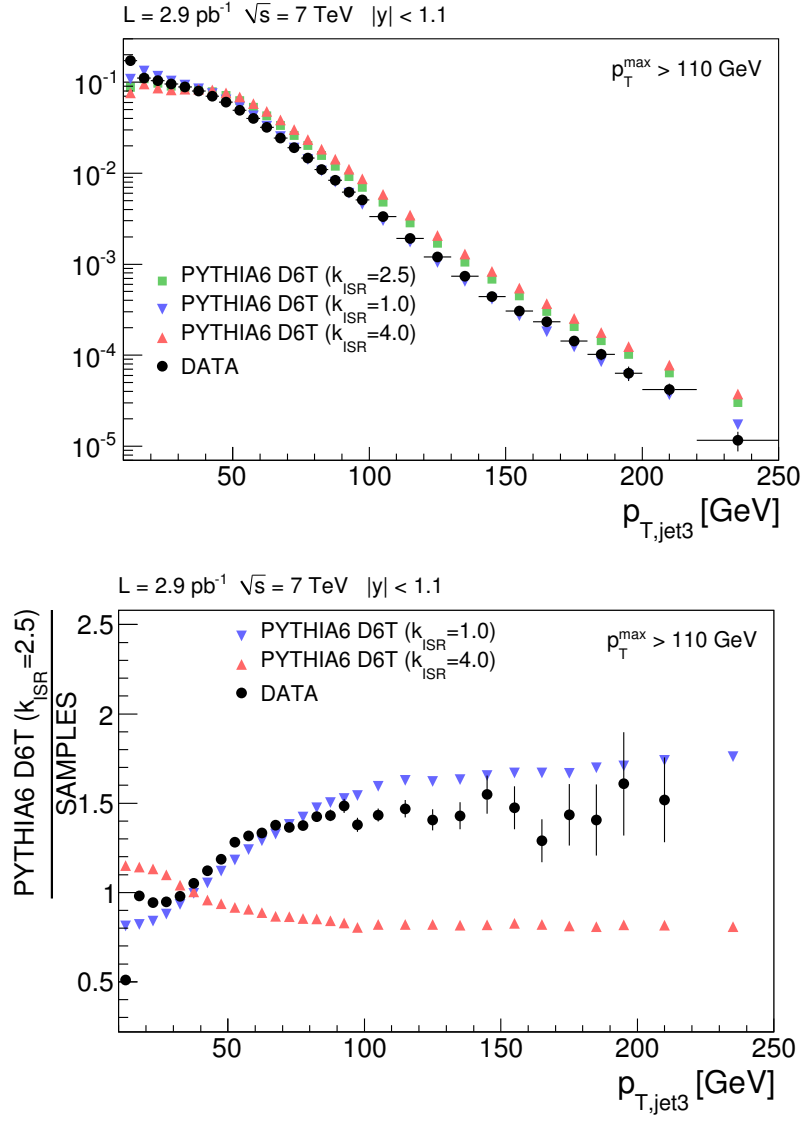| Bin Low [rad]	Bin High [rad]	$\Delta\varphi_{\text{dijet}}$ [rad]	$1/\sigma_{\text{dijet}}(\text{d}\sigma_{\text{dijet}}/\text{d}\Delta\varphi_{\text{dijet}})$ [rad^{-1}]
1.57	1.65	1.61	$1.108 \times 10^{-2} \pm 1.39 \times 10^{-3}\,^{+1.13\times10^{-3}}_{-1.12\times10^{-3}}$
1.65	1.73	1.69	$1.251 \times 10^{-2} \pm 1.49 \times 10^{-3}\,^{+1.13\times10^{-3}}_{-1.12\times10^{-3}}$
1.73	1.81	1.77	$1.928 \times 10^{-2} \pm 1.88 \times 10^{-3}\,^{+1.55\times10^{-3}}_{-1.53\times10^{-3}}$
1.81	1.88	1.85	$2.238 \times 10^{-2} \pm 2.05 \times 10^{-3}\,^{+1.58\times10^{-3}}_{-1.57\times10^{-3}}$
1.88	1.96	1.93	$3.111 \times 10^{-2} \pm 2.44 \times 10^{-3}\,^{+1.94\times10^{-3}}_{-1.92\times10^{-3}}$
1.96	2.04	2.00	$4.282 \times 10^{-2} \pm 2.89 \times 10^{-3}\,^{+2.34\times10^{-3}}_{-2.32\times10^{-3}}$
2.04	2.12	2.08	$6.652 \times 10^{-2} \pm 3.63 \times 10^{-3}\,^{+3.21\times10^{-3}}_{-3.18\times10^{-3}}$
2.12	2.20	2.16	$8.410 \times 10^{-2} \pm 4.11 \times 10^{-3}\,^{+3.59\times10^{-3}}_{-3.57\times10^{-3}}$
2.20	2.28	2.24	$1.111 \times 10^{-1} \pm 4.75 \times 10^{-3}\,^{+4.25\times10^{-3}}_{-4.23\times10^{-3}}$
2.28	2.36	2.32	$1.565 \times 10^{-1} \pm 5.67 \times 10^{-3}\,^{+5.44\times10^{-3}}_{-5.42\times10^{-3}}$
2.36	2.43	2.40	$2.133 \times 10^{-1} \pm 6.64 \times 10^{-3}\,^{+6.85\times10^{-3}}_{-6.85\times10^{-3}}$
2.43	2.51	2.47	$2.903 \times 10^{-1} \pm 7.77 \times 10^{-3}\,^{+8.79\times10^{-3}}_{-8.82\times10^{-3}}$
2.51	2.59	2.55	$4.062 \times 10^{-1} \pm 9.22 \times 10^{-3}\,^{+1.18\times10^{-2}}_{-1.19\times10^{-2}}$
2.59	2.67	2.63	$5.549 \times 10^{-1} \pm 1.08 \times 10^{-2}\,^{+1.57\times10^{-2}}_{-1.58\times10^{-2}}$
2.67	2.75	2.71	$7.518 \times 10^{-1} \pm 1.26 \times 10^{-2}\,^{+2.10\times10^{-2}}_{-2.11\times10^{-2}}$
2.75	2.83	2.79	$1.007 \pm 1.46 \times 10^{-2}\,^{+2.81\times10^{-2}}_{-2.82\times10^{-2}}$
2.83	2.91	2.87	$1.362 \pm 1.69 \times 10^{-2}\,^{+3.83\times10^{-2}}_{-3.85\times10^{-2}}$
2.91	2.98	2.95	$1.840 \pm 1.97 \times 10^{-2}\,^{+5.30\times10^{-2}}_{-5.30\times10^{-2}}$
2.98	3.06	3.02	$2.541 \pm 2.31 \times 10^{-2}\,^{+7.63\times10^{-2}}_{-7.59\times10^{-2}}$
3.06	3.14	3.10	$3.150 \pm 2.57 \times 10^{-2}\,^{+1.00\times10^{-1}}_{-9.93\times10^{-2}}$

TABLE XI

DIJET AZIMUTHAL DECORRELATIONS FOR $80 < p_{T,max} < 110$ GeV/c.

Appendix E (Continued)

Bin Low [rad]	Bin High [rad]	$\Delta\varphi_{\mathbf{dijet}}$ [rad]	$1/\sigma_{\mathbf{dijet}}(\mathbf{d}\sigma_{\mathbf{dijet}}/\mathbf{d}\Delta\varphi_{\mathbf{dijet}})$ [rad^{-1}]
1.57	1.65	1.61	$6.457 \times 10^{-3} \pm 6.52 \times 10^{-4}\,^{+7.04\times10^{-4}}_{-7.18\times10^{-4}}$
1.65	1.73	1.69	$9.562 \times 10^{-3} \pm 8.05 \times 10^{-4}\,^{+9.26\times10^{-4}}_{-9.43\times10^{-4}}$
1.73	1.81	1.77	$1.218 \times 10^{-2} \pm 9.20 \times 10^{-4}\,^{+1.04\times10^{-3}}_{-1.06\times10^{-3}}$
1.81	1.88	1.85	$1.794 \times 10^{-2} \pm 1.13 \times 10^{-3}\,^{+1.35\times10^{-3}}_{-1.37\times10^{-3}}$
1.88	1.96	1.93	$2.513 \times 10^{-2} \pm 1.35 \times 10^{-3}\,^{+1.66\times10^{-3}}_{-1.68\times10^{-3}}$
1.96	2.04	2.00	$3.178 \times 10^{-2} \pm 1.53 \times 10^{-3}\,^{+1.84\times10^{-3}}_{-1.85\times10^{-3}}$
2.04	2.12	2.08	$4.924 \times 10^{-2} \pm 1.92 \times 10^{-3}\,^{+2.49\times10^{-3}}_{-2.49\times10^{-3}}$
2.12	2.20	2.16	$6.861 \times 10^{-2} \pm 2.28 \times 10^{-3}\,^{+3.04\times10^{-3}}_{-3.03\times10^{-3}}$
2.20	2.28	2.24	$9.748 \times 10^{-2} \pm 2.74 \times 10^{-3}\,^{+3.81\times10^{-3}}_{-3.78\times10^{-3}}$
2.28	2.36	2.32	$1.347 \times 10^{-1} \pm 3.23 \times 10^{-3}\,^{+4.70\times10^{-3}}_{-4.65\times10^{-3}}$
2.36	2.43	2.40	$1.860 \times 10^{-1} \pm 3.82 \times 10^{-3}\,^{+5.88\times10^{-3}}_{-5.82\times10^{-3}}$
2.43	2.51	2.47	$2.561 \times 10^{-1} \pm 4.49 \times 10^{-3}\,^{+7.49\times10^{-3}}_{-7.41\times10^{-3}}$
2.51	2.59	2.55	$3.579 \times 10^{-1} \pm 5.32 \times 10^{-3}\,^{+9.88\times10^{-3}}_{-9.80\times10^{-3}}$
2.59	2.67	2.63	$5.013 \times 10^{-1} \pm 6.31 \times 10^{-3}\,^{+1.33\times10^{-2}}_{-1.32\times10^{-2}}$
2.67	2.75	2.71	$7.017 \times 10^{-1} \pm 7.48 \times 10^{-3}\,^{+1.82\times10^{-2}}_{-1.82\times10^{-2}}$
2.75	2.83	2.79	$9.562 \times 10^{-1} \pm 8.73 \times 10^{-3}\,^{+2.46\times10^{-2}}_{-2.46\times10^{-2}}$
2.83	2.91	2.87	$1.310 \pm 1.02 \times 10^{-2}\,^{+3.39\times10^{-2}}_{-3.39\times10^{-2}}$
2.91	2.98	2.95	$1.845 \pm 1.21 \times 10^{-2}\,^{+4.89\times10^{-2}}_{-4.88\times10^{-2}}$
2.98	3.06	3.02	$2.636 \pm 1.45 \times 10^{-2}\,^{+7.27\times10^{-2}}_{-7.26\times10^{-2}}$
3.06	3.14	3.10	$3.485 \pm 1.66 \times 10^{-2}\,^{+1.02\times10^{-1}}_{-1.02\times10^{-1}}$

TABLE XII

DIJET AZIMUTHAL DECORRELATIONS FOR $110 < p_{T,max} < 140$ GeV/c.

Appendix E (Continued)

Bin Low [rad]	Bin High [rad]	$\Delta\varphi_{\mathbf{dijet}}$ [rad]	$1/\sigma_{\mathbf{dijet}}(\mathrm{d}\sigma_{\mathbf{dijet}}/\mathrm{d}\Delta\varphi_{\mathbf{dijet}})$ [rad^{-1}]
1.57	1.65	1.61	$4.412 \times 10^{-3} \pm 8.34 \times 10^{-4} {}^{+3.80\times10^{-4}}_{-3.92\times10^{-4}}$
1.65	1.73	1.69	$5.155 \times 10^{-3} \pm 9.11 \times 10^{-4} {}^{+3.97\times10^{-4}}_{-4.12\times10^{-4}}$
1.73	1.81	1.77	$6.905 \times 10^{-3} \pm 1.07 \times 10^{-3} {}^{+4.75\times10^{-4}}_{-4.94\times10^{-4}}$
1.81	1.88	1.85	$1.206 \times 10^{-2} \pm 1.42 \times 10^{-3} {}^{+7.39\times10^{-4}}_{-7.71\times10^{-4}}$
1.88	1.96	1.93	$1.585 \times 10^{-2} \pm 1.64 \times 10^{-3} {}^{+8.64\times10^{-4}}_{-9.03\times10^{-4}}$
1.96	2.04	2.00	$2.614 \times 10^{-2} \pm 2.13 \times 10^{-3} {}^{+1.27\times10^{-3}}_{-1.33\times10^{-3}}$
2.04	2.12	2.08	$3.617 \times 10^{-2} \pm 2.52 \times 10^{-3} {}^{+1.56\times10^{-3}}_{-1.64\times10^{-3}}$
2.12	2.20	2.16	$5.584 \times 10^{-2} \pm 3.15 \times 10^{-3} {}^{+2.15\times10^{-3}}_{-2.26\times10^{-3}}$
2.20	2.28	2.24	$7.625 \times 10^{-2} \pm 3.70 \times 10^{-3} {}^{+2.64\times10^{-3}}_{-2.78\times10^{-3}}$
2.28	2.36	2.32	$1.130 \times 10^{-1} \pm 4.53 \times 10^{-3} {}^{+3.56\times10^{-3}}_{-3.74\times10^{-3}}$
2.36	2.43	2.40	$1.591 \times 10^{-1} \pm 5.40 \times 10^{-3} {}^{+4.62\times10^{-3}}_{-4.84\times10^{-3}}$
2.43	2.51	2.48	$2.273 \times 10^{-1} \pm 6.47 \times 10^{-3} {}^{+6.17\times10^{-3}}_{-6.44\times10^{-3}}$
2.51	2.59	2.55	$3.135 \times 10^{-1} \pm 7.62 \times 10^{-3} {}^{+8.08\times10^{-3}}_{-8.38\times10^{-3}}$
2.59	2.67	2.63	$4.529 \times 10^{-1} \pm 9.18 \times 10^{-3} {}^{+1.12\times10^{-2}}_{-1.16\times10^{-2}}$
2.67	2.75	2.71	$6.341 \times 10^{-1} \pm 1.09 \times 10^{-2} {}^{+1.54\times10^{-2}}_{-1.57\times10^{-2}}$
2.75	2.83	2.79	$9.066 \times 10^{-1} \pm 1.30 \times 10^{-2} {}^{+2.17\times10^{-2}}_{-2.21\times10^{-2}}$
2.83	2.91	2.87	$1.251 \pm 1.53 \times 10^{-2} {}^{+3.00\times10^{-2}}_{-3.05\times10^{-2}}$
2.91	2.98	2.95	$1.803 \pm 1.83 \times 10^{-2} {}^{+4.39\times10^{-2}}_{-4.44\times10^{-2}}$
2.98	3.06	3.03	$2.703 \pm 2.23 \times 10^{-2} {}^{+6.80\times10^{-2}}_{-6.86\times10^{-2}}$
3.06	3.14	3.10	$3.910 \pm 2.68 \times 10^{-2} {}^{+1.03\times10^{-1}}_{-1.04\times10^{-1}}$

TABLE XIII

DIJET AZIMUTHAL DECORRELATIONS FOR $140 < p_{T,max} < 200$ GeV/c.

Appendix E (Continued)

Bin Low [rad]	Bin High [rad]	$\Delta\varphi_{\text{dijet}}$ [rad]	$1/\sigma_{\text{dijet}}(\text{d}\sigma_{\text{dijet}}/\text{d}\Delta\varphi_{\text{dijet}})$ [rad^{-1}]
1.57	1.81	1.70	$3.208 \times 10^{-3} \pm 9.26 \times 10^{-4} {}^{+2.48\times10^{-4}}_{-2.67\times10^{-4}}$
1.81	1.96	1.89	$1.111 \times 10^{-2} \pm 2.14 \times 10^{-3} {}^{+6.52\times10^{-4}}_{-6.91\times10^{-4}}$
1.96	2.12	2.05	$2.232 \times 10^{-2} \pm 3.07 \times 10^{-3} {}^{+1.03\times10^{-3}}_{-1.08\times10^{-3}}$
2.12	2.28	2.20	$5.077 \times 10^{-2} \pm 4.67 \times 10^{-3} {}^{+1.86\times10^{-3}}_{-1.90\times10^{-3}}$
2.28	2.36	2.32	$9.685 \times 10^{-2} \pm 9.19 \times 10^{-3} {}^{+3.04\times10^{-3}}_{-3.06\times10^{-3}}$
2.36	2.43	2.40	$1.267 \times 10^{-1} \pm 1.06 \times 10^{-2} {}^{+3.62\times10^{-3}}_{-3.61\times10^{-3}}$
2.43	2.51	2.48	$1.826 \times 10^{-1} \pm 1.27 \times 10^{-2} {}^{+4.80\times10^{-3}}_{-4.76\times10^{-3}}$
2.51	2.59	2.55	$2.567 \times 10^{-1} \pm 1.51 \times 10^{-2} {}^{+6.31\times10^{-3}}_{-6.22\times10^{-3}}$
2.59	2.67	2.63	$3.419 \times 10^{-1} \pm 1.75 \times 10^{-2} {}^{+7.99\times10^{-3}}_{-7.84\times10^{-3}}$
2.67	2.75	2.71	$5.912 \times 10^{-1} \pm 2.30 \times 10^{-2} {}^{+1.33\times10^{-2}}_{-1.31\times10^{-2}}$
2.75	2.83	2.79	$8.211 \times 10^{-1} \pm 2.71 \times 10^{-2} {}^{+1.82\times10^{-2}}_{-1.77\times10^{-2}}$
2.83	2.91	2.87	$1.177 \pm 3.25 \times 10^{-2} {}^{+2.59\times10^{-2}}_{-2.53\times10^{-2}}$
2.91	2.98	2.95	$1.716 \pm 3.91 \times 10^{-2} {}^{+3.82\times10^{-2}}_{-3.72\times10^{-2}}$
2.98	3.06	3.03	$2.698 \pm 4.89 \times 10^{-2} {}^{+6.17\times10^{-2}}_{-6.02\times10^{-2}}$
3.06	3.14	3.10	$4.519 \pm 6.29 \times 10^{-2} {}^{+1.08\times10^{-1}}_{-1.06\times10^{-1}}$

TABLE XIV

DIJET AZIMUTHAL DECORRELATIONS FOR $200 < p_{T,max} < 300$ GeV/c.

Appendix E (Continued)

Bin Low [rad]	Bin High [rad]	$\mathbf{\Delta\varphi_{dijet}}$ [rad]	$1/\sigma_{dijet}(d\sigma_{dijet}/d\Delta\varphi_{dijet})$ [rad^{-1}]
1.57	1.96	1.80	$3.070 \times 10^{-3} \pm 1.77 \times 10^{-3} {}^{+2.07\times10^{-4}}_{-2.08\times10^{-4}}$
1.96	2.28	2.14	$1.889 \times 10^{-2} \pm 5.05 \times 10^{-3} {}^{+8.24\times10^{-4}}_{-8.39\times10^{-4}}$
2.28	2.43	2.36	$6.105 \times 10^{-2} \pm 1.30 \times 10^{-2} {}^{+2.03\times10^{-3}}_{-2.08\times10^{-3}}$
2.43	2.59	2.52	$1.605 \times 10^{-1} \pm 2.13 \times 10^{-2} {}^{+4.49\times10^{-3}}_{-4.61\times10^{-3}}$
2.59	2.75	2.68	$4.113 \times 10^{-1} \pm 3.42 \times 10^{-2} {}^{+9.99\times10^{-3}}_{-1.02\times10^{-2}}$
2.75	2.83	2.79	$7.207 \times 10^{-1} \pm 6.40 \times 10^{-2} {}^{+1.63\times10^{-2}}_{-1.66\times10^{-2}}$
2.83	2.91	2.87	$9.790 \times 10^{-1} \pm 7.44 \times 10^{-2} {}^{+2.14\times10^{-2}}_{-2.17\times10^{-2}}$
2.91	2.98	2.95	$1.615 \pm 9.53 \times 10^{-2} {}^{+3.50\times10^{-2}}_{-3.51\times10^{-2}}$
2.98	3.06	3.03	$2.756 \pm 1.24 \times 10^{-1} {}^{+6.02\times10^{-2}}_{-5.97\times10^{-2}}$
3.06	3.14	3.10	$5.282 \pm 1.71 \times 10^{-1} {}^{+1.19\times10^{-1}}_{-1.16\times10^{-1}}$

TABLE XV

DIJET AZIMUTHAL DECORRELATIONS FOR $p_{T,max} > 300$ GeV/c.

CITED LITERATURE

1. Griffiths, D.: <u>Introduction to Elementary Particles</u>. WILEY-VCH, second edition, 2008.

2. Peskin, M. E. and Schroeder, D. V.: <u>An Introduction to Quantum Field Theory</u>. Westview Press, 1995.

3. Halzen, F. and Martin, A. D.: <u>Quarks and Leptons: An Introductory Course in Modern Particle Physics</u>. John Wiley & Sons, Inc., 1984.

4. Gell-Mann, M.: A schematic model of baryons and mesons. <u>Physics Letters</u>, 8(3):214–215, February 1964.

5. Zweig, G.: An SU_3 model for strong interaction symmetry and its breaking. <u>CERN Report</u>, February 1964. CERN-TH-412.

6. Bethke, S.: Experimental tests of asymptotic freedom. <u>Progress in Particle and Nuclear Physics</u>, 58(2):351–386, April 2007.

7. Nagy, Z.: Three-Jet Cross Sections in Hadron-Hadron Collisions at Next-To-Leading Order. <u>Physical Review Letters</u>, 88(12):122003, March 2002.

8. Kluge, T., Rabbertz, K., and Wobisch, M.: FastNLO: Fast pQCD calculations for PDF fits. In <u>14th International Workshop On Deep Inelastic Scattering</u>, September 2006. arXiv:hep-ph/0609285.

9. The DØ Collaboration: Measurement of Dijet Azimuthal Decorrelations at Central Rapidities in $p\bar{p}$ Collisions at $\sqrt{s} = 1.96$ TeV. <u>Physical Review Letters</u>, 94(22):221801, June 2005.

10. The ATLAS Collaboration: Measurement of Dijet Azimuthal Decorrelations in pp Collisions at $\sqrt{s} = 7$ TeV. <u>Physical Review Letters</u>, 106(17):172002, April 2011.

11. The CMS Collaboration: Dijet Azimuthal Decorrelations in pp Collisions at $\sqrt{s} = 7$ TeV. <u>Physical Review Letters</u>, 106(12):122003, March 2011.

12. Ellis, K. R., Stirling, J. W., and Webber, B. R.: QCD and Collider Physics. Cambrige University Press, December 2003.

13. Sjostrand, T., Mrenna, S., and Skands, P.: PYTHIA 6.4 physics and manual. JHEP, 05:026, May 2006.

14. Sjostrand, T., Mrenna, S., and Skands, P.: A brief introduction to PYTHIA 8.1. Computer Physics Communications, 178(11):852–867, January 2008.

15. Bahr, M., et al.: Herwig++ physics and manual. The European Physical Journal C, 58:639–707, November 2008.

16. Gieseke, S., Stephens, P., and Webber, B.: New formalism for QCD parton showers. JHEP, 12:045, December 2003.

17. Alwall, J., et al.: MadGraph/MadEvent v4: the new web generation. JHEP, 09:028, September 2007.

18. Alwall, J., et al.: A standard format for Les Houches Event Files. Computer Physics Communications, 176(4):300–304, February 2007.

19. Agostinelli, S., et al.: Geant4–a simulation toolkit. Nuclear Instruments and Methods in Physics Research A, 506(3):250–303, March 2003.

20. Evans, L. and Bryant, P.: LHC Machine. JINST, 3(S08001), August 2008.

21. The ATLAS Collaboration: The ATLAS Experiment at the CERN Large Hadron Collider. JINST, 3(S08003), August 2008.

22. The CMS Collaboration: The CMS experiment at the CERN LHC. JINST, 3(S08004), August 2008.

23. The ALICE Collaboration: The ALICE experiment at the CERN LHC. JINST, 3(S08002), August 2008.

24. The LHCb Collaboration: The LHCb Detector at the LHC. JINST, 3(S08005), August 2008.

25. The CMS Collaboration: The CMS tracker system project. Technical Design Report CERN-LHCC-98-6, CERN, April 1998.

26. Grupen, C. and Shwartz, B.: Particle Detectors. Cambrige University Press, Second edition, 2008.

27. The CMS Collaboration: The CMS electromagnetic calorimeter project. Technical Design Report CERN-LHCC-97-33, CERN, December 1997.

28. The CMS Collaboration: The CMS hadron calorimeter project. Technical Design Report CERN-LHCC-97-31, CERN, June 1997.

29. The CMS Collaboration: The CMS magnet project. Technical Design Report CERN-LHCC-97-10, CERN, May 1997.

30. The CMS Collaboration: The CMS muon project. Technical Design Report CERN-LHCC-97-32, CERN, December 1997.

31. The CMS Collaboration: The CMS TriDAS project. Technical Design Report CERN-LHCC-2000-38, CERN, December 2000.

32. Iles, G., et al.: Revised CMS Global Calorimeter Trigger Functionality & Algorithms. In 12th Workshop on Electronics for LHC and Future Experiments, ed. CERN, 2006.

33. The CMS Collaboration: The CMS trigger and data-acquisition project. Technical Design Report CERN-LHCC-2002-26, CERN, December 2002.

34. Huth, J. E., et al.: Toward a Standardization of Jet Definitions. In Proceedings of Research Directions for the Decade: Snowmass 1990, ed. E. L. Berger, July 1990.

35. Eck, C., et al.: LHC Computing Grid. Technical Design Report CERN-LHCC-2005-024, CERN, June 2005.

36. Brun, R. and Rademakers, F.: ROOT – An object oriented data analysis framework. Nuclear Instruments and Methods in Physics Research A, 389(1-2):81–86, April 1997.

37. Kovalskyi, D., et al.: Fireworks: A Physics Event Display for CMS. Journal of Physics: Conference Series, 219(032014), 2010.

38. The CMS Collaboration: CMS tracking performance results from early LHC operation. The European Physical Journal C, 70:1165–1192, November 2010.

39. Speer, T., et al.: Track reconstruction in the CMS tracker. Nuclear Instruments and Methods in Physics Research A, 559(1):143–147, December 2006.

40. Waltenberger, W., Fruhwirth, R., and Vanlaer, P.: Adaptive vertex fitting. Journal of Physics G, 34(12):343–356, November 2007.

41. The CMS Collaboration: Tracking and Primary Vertex Results in First 7 TeV Collisions. CMS Physics Analysis Summary, July 2010. CMS-PAS-TRK-10-005.

42. The CMS Collaboration: CMS Physics TDR Volume I : Detector Performance and Software. Technical Design Report CERN-LHCC-2006-001, CERN, February 2006.

43. The CMS Collaboration: Photon reconstruction and identification at $\sqrt{s} = 7$ TeV. CMS Physics Analysis Summary, July 2010. CMS-PAS-EGM-10-005.

44. The CMS Collaboration: Electron reconstruction and identification at $\sqrt{s} = 7$ TeV. CMS Physics Analysis Summary, August 2010. CMS-PAS-EGM-10-004.

45. The CMS Collaboration: Performance of CMS muon reconstruction in cosmic-ray events. JINST, 5(T03022), March 2010.

46. Salam, G. P. and Soyez, G.: A practical seedless infrared-safe cone jet algorithm. JHEP, 05:086, May 2007.

47. The CMS Collaboration: Jet Plus Tracks Algorithm for Calorimeter Jet Energy Corrections in CMS. CMS Physics Analysis Summary, August 2009. CMS-PAS-JME-09-002.

48. The CMS Collaboration: Commissioning of TrackJets in pp Collisions at 7 TeV. CMS Physics Analysis Summary, July 2010. CMS-PAS-JME-10-006.

49. Cacciari, M. and Salam, G. P.: The anti-k_t jet clustering algorithm. JHEP, 04:063, April 2008.

50. The CMS Collaboration: Calorimeter Jet Quality Criteria for the First CMS Collision Data. CMS Physics Analysis Summary, April 2010. CMS-PAS-JME-09-008.

51. The CMS Collaboration: Particle–Flow Event Reconstruction in CMS and Performance for Jets, Taus, and $\not{E}_T$. CMS Physics Analysis Summary, April 2009. CMS-PAS-PFT-09-001.

52. The CMS Collaboration: Commissioning of the Particle–Flow Reconstruction in Minimum–Bias and Jet Events from pp Collisions at 7 TeV. CMS Physics Analysis Summary, July 2010. CMS-PAS-PFT-10-002.

53. The CMS Collaboration: Determination of Jet Energy Calibration and Transverse Momentum Resolution in CMS. CMS Physics Analysis Summary, July 2011. CMS-JME-10-011.

54. Cacciari, M. and Salam, G. P.: Pileup subtraction using jet areas. Physics Letters B, 659(1-2):119–126, January 2008.

55. The CMS Collaboration: Determination of the Jet Energy Scale in CMS with pp Collisions at 7 TeV. CMS Physics Analysis Summary, November 2010. CMS-PAS-JME-10-010.

56. The CMS Collaboration: Jet Energy Resolution in CMS at 7 TeV. CMS Physics Analysis Summary, March 2011. CMS-PAS-JME-10-014.

57. The CMS Collaboration: Jet Performance in pp Collisions at 7 TeV. CMS Physics Analysis Summary, July 2010. CMS-PAS-JME-10-003.

58. The CMS Collaboration: Measurement of CMS Luminosity. CMS Physics Analysis Summary, July 2010. CMS-PAS-EWK-10-004.

59. Field, R.: Early LHC Underlying Event Data - Findings and Surprises. In The Hadron Collider Physics Symposium, October 2010. arXiv:hep-ph/1010.3558.

60. Lafferty, G. D. and Wyatt, T. R.: Where to Stick Your Data Points: The Treatment of Measurements Within Wide Bins. Nuclear Instruments and Methods in Physics Research A, 355(2-3):541–547, February 1995.

61. Tung, W. K., et al.: Heavy quark mass effects in deep inelastic scattering and global QCD analysis. JHEP, 02(053), February 2007.

62. Martin, A. D., et al.: MRST2001: partons and α_s from precise deep inelastic scattering and Tevatron jet data. The European Physical Journal C, 23(1):73–87, January 2002.

63. Hoeche, S., et al.: Matching Parton Showers and Matrix Elements. In HERA and the LHC Workshop, February 2006. arXiv:hep-ph/0602031.

64. Alekhin, S., et al.: The PDF4LHC Working Group Interim Report. arXiv:hep-ph/1101.0536, January 2011.

65. Albrow, M., et al.: Tevatron-for-LHC Report of the QCD Working Group. arXiv:hep-ph/0610012, October 2006.

66. The CMS Collaboration: Measurement of the Jet Energy Resolutions and Jet Reconstruction Efficiency at CMS. CMS Physics Analysis Summary, July 2009. CMS-PAS-JME-09-007.

Name	Cosmin Dragoiu
Education	Ph.D., Physics University of Illinois at Chicago, Chicago, Illinois 2011
	Graduate Classes, Physics University of Bucharest, Bucharest, Romania 2003 - 2004
	B.Sc., Physics and Engineering Technical University of Cluj-Napoca, Cluj-Napoca, Romania 2002
Summer Schools	The 5th CERN-Fermilab Hadron Collider Physics Summer School Fermilab, Batavia, Illinois 2010
	The 16th Coordinated Theoretical-Experimental Project on QCD Summer School University of Wisconsin, Madison, Wisconsin 2009
Awards	Provost Award for Graduate Research University of Illinois at Chicago, Chicago, Illinois 2010
Scholarships	Socrates Erasmus Scholarship Technical University of Chemnitz, Chemnitz, Germany 2002
	Undergraduate Scholarship Technical University of Cluj-Napoca, Cluj-Napoca, Romania 1998 - 2002

Teaching	Teaching Assistant University of Illinois at Chicago, Chicago, Illinois 2005
Experience	Research Assistant (CMS Experiment) University of Illinois at Chicago, Chicago, Illinois 2007 - 2011
	Research Assistant (D-Zero Experiment) University of Illinois at Chicago, Chicago, Illinois 2005 - 2006
	Engineer National R&D Institute for Cryogenic and Isotopic Technologies, Ramnicu Vilcea, Romania 2002 - 2004
	Intern Technical University of Chemnitz, Chemnitz, Germany 2002
Presentations	Jet Results from CMS (Invited talk) XIX International Workshop on Deep-Inelastic Scattering and Related Subjects, Newport News, Virginia 2011
	Dijet Physics with the CMS Detector at LHC (Invited poster) The 35th International Conference on High Energy Physics, Paris, France 2010
	Dijet Azimuthal Decorrelations (Invited talk) US CMS JTerm III, Fermilab, Batavia, Illinois 2009
	Probing Matter down to 10^{-20} Meters (Invited poster) US LHC Users Meeting, Fermilab, Batavia, Illinois 2008

Performance of Jet Algorithms at CMS (Invited talk)
American Physical Society April Meeting, St. Louis, Missouri
2008

Jet Studies at CMS (Invited talk)
UIC Physics Fest, Chicago, Illinois
2008

Conference Proceedings	C. Dragoiu: Dijet Physics with the CMS Detector at LHC. PoS(ICHEP 2010)130, December 2010.
Publications	The CMS Collaboration: Dijet Azimuthal Decorrelations in pp Collisions at $\sqrt{s}$ = 7 TeV. Physical Review Letters, 106(12):122003, March 2011.
	The CMS Collaboration: Measurement of Dijet Angular Distributions and Search for Quark Compositeness in pp Collisions at 7 TeV. Physical Review Letters, 106(20):201804, May 2011.